Testing inflation models by primordial black holes, gravitational wave and the Swampland conjectures

原始ブラックホール、重力波および
スワンプランドコンジェクチャーによる
インフレーションモデルの検証

Yuma S. FURUTA

Supervisor: Prof. Takahiko Matsubara

Department of Particle and Nuclear Physics
School of High Energy Accelerator Science
The Graduate University for Advanced Studies, SOKENDAI

This dissertation is submitted for the degree of
Doctor of Philosophy

March 2026

Abstract

In this doctoral dissertation, we compute observational quantities arising from multi-field inflation with the production of primordial black holes, and discuss theoretical constraints from the Swampland Conjectures. As a proposed solution to the problems of the standard Big Bang cosmology, a phase of exponential expansion of spacetime, known as inflation, has been introduced and is now widely accepted. While various specific mechanisms for inflation have been proposed, they have not yet been uniquely determined, and these are crucial for understanding the origin of the universe. In this research, we demonstrate that, from a bottom-up perspective, computing observable quantities predicted by a concrete inflation model helps identify viable inflationary scenarios. On the other hand, from a top-down perspective, we show that the Swampland Distance Conjecture imposes constraints on the parameters of inflationary models, thereby providing an alternative route toward their identification. First, as a bottom-up perspective, we show that resonant processes during multi-field trapped inflation can generate a large curvature perturbation on small scales without fine-tuning. This perturbation naturally leads to the formation of primordial black holes that may constitute dark matter, as well as to the production of stochastic induced gravitational waves in the deci-Hz band. Such waves are within the reach of future space-based interferometers, such as LISA, DECIGO and BBO. Furthermore, primordial black hole binaries formed at late times produce merger gravitational waves that can be probed by the resonant cavity experiments in addition to interferometers. Next, as a top-down perspective, we impose constraints on inflation models from the Swampland Distance Conjecture and the Lyth Bound. In the case of large field models, a quantitative relation is established between the field distance $\Delta\phi$ and the tensor-to-scalar ratio r. Based on these, we plot the relationship between the field distance $\Delta\phi$ and the tensor-to-scalar ratio r for specific inflation models by running the e-folding number from 47 to 62. The two bounds play complementary roles in assessing the viability of inflationary scenarios. We demonstrate that, for certain representative large field inflation models, the Swampland Distance Conjecture alone can impose more stringent upper limits on the tensor-to-scalar ratio than current observational constraints from the cosmic microwave background.

Publication List

This Ph.D. thesis is mainly based on

[1] **Yuma S. Furuta**, Hamada Yuta and Kohri Kazunori, "Inflation models selected by the swampland distance conjecture with the Lyth bound," Phys. Rev. D **112**, no.12, 103517 (2025) doi:10.1103/lpd1-mbmm [arXiv:2507.23320 [hep-th]].

[2] **Yuma S. Furuta**, Mindaugas Karčiauskas, Kohri Kazunori and Alejandro Saez, "Primordial Black Holes as Dark Matter and the Tachyonic Trap During Inflation," [arXiv:2511.23182 [astro-ph.CO]], submitted to JCAP.

In the first paper [1], we demonstrate that resonance processes during multi-field inflation can enhance curvature perturbations on small scales. As a consequence, primordial black holes, which may constitute a component of dark matter, can be produced. We further show the resulting gravitational-wave spectra emitted during the mergers of these primordial black holes. In addition, it is demonstrated that both these gravitational waves and the second-order induced gravitational waves are potentially observable by future gravitational-wave experiments. These results are discussed in detail in Chapters III-V of this paper.

In the second paper [2], we investigate the constraints imposed by the Swampland Distance Conjecture and the Lyth bound on concrete inflationary models. We find that these theoretical considerations lead to more stringent constraints on the parameters of the inflationary potential than those derived from current observational bounds, such as those from Planck 2018. These results are presented in detail in Chapter VI of this paper.

Table of contents

Introduction

In the past, the standard Big Bang theory described by the cosmological principle and general relativity, had long been believed to provide a theory explaining the origin and evolution of the Universe. However, the standard Big Bang theory suffers from several problems, among which representative examples include the horizon problem, the flatness problem, the monopole problem, and the origin of primordial density perturbations [1]. For instance, taking the flatness problem as an example, in the standard Big Bang theory the Hubble horizon increases monotonically, and hence in the early Universe the Ω parameter of curvature must be fine-tuned to an extremely small value. The origin of these difficulties lies in the fact that the cosmic expansion caused by radiation or matter is decelerated. Inflationary cosmology, characterized by a stage of accelerated expansion [2–5], provides elegant resolutions to several fundamental problems in standard cosmology, including the flatness problem. At present, it is widely accepted as a framework that accounts for the current state of the universe from more general initial conditions.

However, revealing the underlying mechanism responsible for inflation still remains one of the most urgent and central issues in modern cosmology. In addition, despite its theoretical successes, the precise nature of the scalar field ϕ, commonly referred to as the inflaton field, has not yet been established. Furthermore, neither the energy scale at which inflation occurred nor its precise epoch in cosmic history has been directly probed by current observational data. Although many inflationary models consistent with observational data, have been proposed, no model has been uniquely identified. Therefore, in order to constrain the precise nature of the inflaton field and, ultimately, to identify a specific inflation model, we impose constraints from both a bottom-up perspective based on observations and a top-down perspective based on UV-complete theories at high energy scales.

We first consider the bottom-up perspective, which is provided by observations of the cosmic microwave background (CMB) [6]. Inflation can explain the origin of quantum perturbations. This means inflation generates curvature perturbations, and spatial variations of these curvature perturbations lead to temperature anisotropies in the CMB. Therefore, comparing the physical quantities theoretically predicted by inflation with current CMB observations provides a means to test inflation. In particular, its tempera-

ture anisotropies and polarization patterns have so far yielded only an upper bound on the energy scale of inflation, constraining it to be below approximately 10^{16} GeV. This constraint is rewritten in terms of the tensor-to-scalar ratio r, and the most stringent current bound is $r < 0.036$ [7, 8].

On the other hand, from a top-down perspective, there exist complementary efforts to constrain the energy scale of inflation based on internal consistency relations derived from purely theoretical considerations. One such relation is the Lyth bound, which applies to slow-roll models with super-Planckian field excursions and provides a model-independent lower bound on r. However, even when both the observational bounds and the theoretical lower bounds discussed above are taken into account, substantial uncertainties remain regarding the model-dependent functional form of the inflaton potential $V(\phi)$ and the total field excursion $\Delta\phi$ during inflation.

Furthermore, recent developments in quantum gravity, particularly in string theory, have motivated theoretical constraints on effective field theories through what are known as the Swampland Conjectures [9]. The Swampland Distance Conjecture [10] proposes that effective field theories with trans-Planckian field excursions are incompatible with a consistent UV completion in quantum gravity, and that, in order to remain within the Landscape, which is the regime of EFT control, the Hubble scale H must decrease accordingly. [1] At present, among the Swampland Conjectures, the Swampland Distance Conjecture is supported by a substantial amount of evidence comparing with other conjectures, and if it is valid, it would impose nontrivial theoretical constraints and yield new exclusions that could not be obtained from previous observations. In this paper, unlike previous studies, we successfully impose constraints on the parameter space of the inflationary potential by applying these constraints to concrete inflationary models. The new results obtained from this theoretical aspect are more restrictive than the conventional Planck2018 data and provide specific footholds for inflation models, as demonstrated in Section VI.3.

In addition to the above constraints on general inflationary models, theoretical models beyond the standard model, such as supergravity or superstring theory, generically predict many light scalar fields. Therefore, it is more natural to consider multi-field inflation [12], in which multiple scalar fields contribute to the inflaton dynamics, rather than single-field inflation. Within such multi-field inflationary scenarios, there exist possibilities that observational signatures arising during inflation or from transitions may provide specific clues for model discrimination. In several multi-field inflationary scenarios, the Universe undergoes multiple-field transitions during inflation, analogous to phase transitions. Identifying the role of these transitions through observations could provide decisive information about the ultimate theory to describe the early Universe.

[1] See also Ref. [11] for bounds on the field excursion from the UV/IR mixing motivated by the holography and entropy bounds.

In some of these models, interactions between fields can cause resonant field excitations during inflation. A classical example is the so called "Trapped Inflation" [13, 14]. But resonances during inflation and their impact on the primordial perturbation had been studied even earlier, for example, in Ref. [15–17] (for some later works see Ref. [18–21]). Many of the works are based on the mechanism suggested in Ref. [13], where moduli fields of string theory are stabilised by the backreaction of resonantly produced particles. As moduli field(s) pass through or close to (in the case of multi-field inflation) a critical point in field space, some real scalar field χ is rendered massless. Thus, this point was naturally denoted by the name "Enhanced Symmetry Point" (ESP) in Ref. [13]. Around ESP the effective mass of χ is changing non-adiabatically, which induces resonant excitations. The excitations backreact onto the motion of the inflaton, modifying its dynamics.

In this work, we consider a somewhat modified scenario. Instead of the field χ becoming massless at the critical point, we allow it to become tachyonic, i.e., its mass squared to become negative. Hence, for some parameter values, the resonance resembles the one studied in Ref. [22], which they called "Tachyonic Resonance". To emphasise this difference, we name the critical point as the "Symmetry Breaking Point" (SBP). The idea for such a scenario is inspired by the tachyonic trap mechanism, employed to provide an alternative method of reheating for non-oscillatory potentials and to prevent the scalar field of the quintessential inflation scenario from reaching superplanckian values [23, 24].

The current scenario is explored in the context of the supersymmetry-inspired multi-field running-mass model [25]. Augmenting the running-mass-inflation (RMI) with the tachyonic trap mechanism provides a concrete scenario by which inflation can end in a form similar to hybrid inflation [26, 27]. The current treatment, however, differs from the usual considerations of hybrid inflation. First, we take the waterfall phase, i.e., the evolution in the χ direction in field space, to last more than 10 e-foldings, which requires a very flat potential. In such a setup, the tachyonic trap becomes essential to redirect the field evolution from the RMI direction into the waterfall one, at least for parameter ranges considered in this work.

The tachyonic resonance at SBP has another important effect: it generates a sharp peak in the spectrum of the primordial perturbation $\mathcal{P}_\zeta$ at small scales. The amplitude of that peak can be enhanced by several orders of magnitude relative to the slow-roll result on large scales. Combined with the large spectral running of RMI, the spectrum can reach as high values as $\mathcal{P}_\zeta \sim 10^{-1.5}$ [25, 28–34]. The resulting large curvature perturbation at the small scales have distinct observational consequences.

Later, upon horizon reentry in the early Universe, the large curvature perturbation can trigger gravitational collapse, leading to the formation of the primordial black holes (PBHs). As argued in Ref. [35] (for reviews, see also Refs. [36–38]), PBHs with masses in the range 10^{17}g [39] – 10^{23}g [40, 41] can serve as dark matter candidates. This scenario can be constrained or confirmed by future gamma-ray observations and related astrophysical

probes [35]. In this paper, we examine in Section IV.3 how the current multi-field trapped inflation model, which satisfies observational constraints, can produce a sufficient abundance of PBHs with masses that potentially explain nearly all dark matter.

Second, the same perturbations generate stochastic induced gravitational waves (SIGWs) through nonlinear second-order effects [42–50]. These SIGWs, peaking in the deci-Hz band, provide promising targets for future gravitational-wave detectors such as LISA, DECIGO, and BBO. In the analysis in this paper, we incorporate recent refinements accounting for the dissipation of small-scale fluctuations [51, 52], yielding state-of-the-art predictions for the SIGW spectrum in Sec. V.1.

Third, PBHs formed in the early Universe can assemble into binaries through many-body gravitational interactions [53–55]. The mergers of these binaries also generate a stochastic background of gravitational waves. Remarkably, such merger signals may be detectable not only by DECIGO and BBO but also through resonant cavity experiments exploiting the inverse Gertsenshtein effect [56, 57], originally proposed in the context of axion searches. In general, in conventional studies of gravitational waves (GWs) generated from binaries, the abundance of PBHs has often been assumed to be nearly 100%. In contrast, in this paper, we compute not only the GW spectra generated from PBH binaries arising from generic PBH mass distributions, but also the GW spectra predicted within the specific inflationary model considered here. As mentioned above, these signals may be detectable by future observations, and moreover, since different inflationary models generate distinct GW spectra, they can serve as a means to distinguish inflationary models in Sec. V.2.

The structure of this thesis is organized as follows. In Chapter I, we point out the problems of the standard Big Bang cosmology, motivate the currently widely accepted inflation theory, and provide an outline of its basic framework. In addition, we briefly introduce the specific inflationary models that are constrained by the Swampland Distance Conjecture in Chapter VI. In Chapter II, we introduce linear perturbation theory and define the physical quantities that play a central role in inflation. In particular, one of these quantities is the curvature perturbation, because we show that the curvature perturbation consistent with CMB observations on large scales is enhanced on small scales in the subsequent Chapter III. Along with the curvature perturbation, we also show other important physical quantities such as the spectral index and the tensor-to-scalar ratio. In Chapter III, we study a hybrid inflation model involving two scalar fields. As mentioned earlier, current research on inflationary models proceeds not only from a bottom-up approach based on observations, but also from a top-down approach based on UV-complete theories such as string theory and quantum gravity, which suggest that inflation may be driven by multiple inflatons. In particular, inflationary models accompanied by a waterfall phase exhibit a rich variety of interesting physical phenomena, and we focus on these features. In Chapter IV, we show that the curvature perturbations enhanced on small

scales in Chapter III can lead to the formation of primordial black holes, which may serve as candidates for dark matter. In Chapter V, we investigate induced GWs generated from second-order tensor perturbations of the metric, as well as GWs produced by mergers of PBHs formed in Chapter IV. In particular, we demonstrate that these signals lie within the sensitivity ranges of future planned interferometric GWs observations, and thus can contribute to identifying inflation from a bottom-up perspective. In Chapter VI, we examine constraints on inflationary models from a top-down perspective arising from the Swampland Distance Conjecture. These constraints can be stronger than the current 1σ limits on the tensor-to-scalar ratio imposed by CMB observations, and thus may provide a foothold for identifying a specific inflation model. Finally, in Chapter VII, we present our conclusions.

Throughout this paper, we adopt natural units where the reduced Planck constant, the speed of light, and the Boltzmann constant are set to $\hbar = c = k_{\rm B} = 1$. Greek indices μ, ν, σ denote four-dimensional spacetime coordinates and run over $0, 1, 2, 3$, while Latin indices i, j, k denote three-dimensional spatial coordinates and run over $1, 2, 3$. Repeated indices are implicitly summed over according to the Einstein summation convention. Therefore, dimensions of time $[T]$, length $[L]$, and mass $[M]$ are related to the dimension of energy $[E]$ as $[L^{`1}] = [T^{`1}] = [M] = [E]$. Also, temperature has units of energy, and it is measured in terms of eV. G is Newton's gravitational constant, planck mass is $M_{\rm pl} = \sqrt{1/G} \approx 1.2 \times 10^{19}\,\text{GeV}$, and reduced planck mass is $m_{\rm pl} = \sqrt{1/8\pi G} \approx 2.4 \times 10^{18}\,\text{GeV}$.

Chapter I

Inflation

In this Chapter I, we present an outline of inflation [58–62] and describe specific models of single-field inflation that will be discussed in the following. Inflationary models resolve various problems that have been identified in hot Big Bang cosmology, such as the flatness problem and the horizon problem. In addition, inflation can generate the origin of primordial density perturbations that serve as the seeds for the large-scale structures observed today, including galaxies and galaxy clusters, and thus can reproduce the present Universe through the formation of large-scale structure from more general initial conditions. The realization of such a phase of inflation, during which spacetime undergoes exponential accelerated expansion in the early Universe, was first proposed by Alexei Starobinsky [4]. Subsequently, in the early 1980s, Katsuhiko Sato [2] and Alan H. Guth [5], who it is named as "inflation," proposed that inflation can be realized as a first-order phase transition in the context of grand unified theories. Later, Andrei Linde [3] proposed a class of inflationary models that smoothly connect to hot Big Bang cosmology through reheating. In contrast to the old scenarios, these are referred to as new inflation. Since then, inflationary theory has been widely accepted.

I.1 Einstein equation

In modern cosmology, one adopts the principle known as the cosmological principle, which states that the Universe is homogeneous and isotropic on large scales. Since this homogeneity and isotropy are consistent with observations of the CMB, adopting this principle is well motivated. Accordingly, we consider the homogeneous and isotropic Friedmann–Lemaître–Robertson–Walker (FLRW) metric [63–66]

$$\mathrm{d}s^2 = g_{\mu\nu}\mathrm{d}x^\mu \mathrm{d}x^\nu \tag{I.1.1}$$

$$= -\mathrm{d}t^2 + a^2(t)\left(\frac{\mathrm{d}r^2}{1-Kr^2} + r^2\left(\mathrm{d}\theta^2 + \sin^2\theta \mathrm{d}\phi^2\right)\right), \tag{I.1.2}$$

where a is the scale factor characterizing the relative size of spatial hypersurfaces at a given time t. The parameter K is the curvature parameter, which typically takes the values $-1, 0, +1$, corresponding to an open, flat, and closed Universe, respectively. From the metric $g_{\mu\nu}$, we first define the connection as

$$\Gamma^{\lambda}{}_{\mu\nu} = \frac{1}{2} g^{\lambda\sigma} \left(g_{\sigma\mu,\nu} + g_{\sigma\nu,\mu} - g_{\mu\nu,\sigma} \right), \tag{I.1.3}$$

where $g_{\mu\nu,\sigma} = \partial g_{\mu\nu} / \partial x^{\sigma}$. From the connection, the Riemann tensor is defined by

$$R^{\sigma}{}_{\mu\nu\rho} = \Gamma^{\sigma}{}_{\mu\rho,\nu} - \Gamma^{\sigma}{}_{\mu\nu,\rho} + \Gamma^{\sigma}{}_{\lambda\nu}\Gamma^{\lambda}{}_{\mu\rho} - \Gamma^{\sigma}{}_{\lambda\rho}\Gamma^{\lambda}{}_{\mu\nu},$$

from which the Ricci tensor $R_{\mu\nu}$ and the Ricci scalar $R = R^{\mu}_{\mu}$ are obtained as

$$R_{00} = -3\frac{\ddot{a}}{a}, \quad R_{0i} = 0, \quad R_{ij} = \left(\frac{\ddot{a}}{a} + 2\frac{\dot{a}^2}{a^2} + 2\frac{K}{a} \right) g_{ij}, \tag{I.1.4}$$

$$R = 6\left(\frac{\ddot{a}}{a} + \frac{\dot{a}^2}{a^2} + \frac{K}{a^2} \right). \tag{I.1.5}$$

The Einstein tensor $G_{\mu\nu}$ is then defined as

$$G_{\mu\nu} \equiv R_{\mu\nu} - \frac{1}{2} g_{\mu\nu} R. \tag{I.1.6}$$

and its components are given by

$$G_{00} = 3\left(\frac{\dot{a}^2}{a^2} + \frac{K}{a^2} \right), \quad G_{0i} = 0, \quad G_{ij} = -\left(2\frac{\ddot{a}}{a} + \frac{\dot{a}^2}{a^2} + \frac{K}{a^2} \right) g_{ij}. \tag{I.1.7}$$

The Einstein equations

$$G_{\mu\nu} = 8\pi G T_{\mu\nu}, \tag{I.1.8}$$

characterize the spacetime and the matter, and determine the dynamics of the Universe. Here, although details will be discussed later, $T_{\mu\nu}$ denotes the stress-energy tensor. From the $(0,0)$ component and the diagonal (i,i) components of the Einstein equations (I.1.8), one obtains the Friedmann equation and the acceleration equation,

$$H^2 = \frac{1}{3m_{\mathrm{pl}}^2}\rho - \frac{K}{a^2}, \tag{I.1.9}$$

$$\dot{H} + H^2 = \frac{\ddot{a}}{a} = -\frac{1}{6m_{\mathrm{pl}}^2}(\rho + 3p), \tag{I.1.10}$$

respectively. Here, an overdot denotes differentiation with respect to the cosmic time t. The quantities ρ and p correspond to the $(0,0)$ and (i,i) components of the stress-energy

tensor, respectively, and represent the energy density and pressure. The Hubble parameter H is defined as $H \equiv \left(\frac{\dot{a}}{a}\right)$ and characterizes the expansion rate of the Universe. The present value of the Hubble parameter, H_0, is given by $H_0 = 100h\,\mathrm{km\,s^{-1}\,Mpc^{-1}}$. Here, the uncertainty in the observational determination of H_0 is absorbed into the dimensionless parameter h [6]. We introduce this notation here since it will appear later in the discussion of gravitational-wave spectra. Since its dimension is $[T^{-1}] = [L^{-1}]$, the inverse Hubble parameter H^{-1} has the dimension of length and can be interpreted as a characteristic size of the Universe, often referred to as the Hubble horizon. The scale factor a is dimensionless. Taking the time derivative of the Friedmann equation (I.1.9), we obtain

$$2H\dot{H} = \frac{1}{3m_{\mathrm{pl}}^2}\dot{\rho}. \tag{I.1.11}$$

Substituting $\dot{H}$ from the acceleration equation (I.1.10) into this expression, we arrive at the continuity equation,

$$\dot{\rho} + 3H(\rho + p) = 0. \tag{I.1.12}$$

Multiplying both sides of this equation by a^3, we find

$$\frac{\mathrm{d}(a^3\rho)}{\mathrm{d}t} + p\frac{\mathrm{d}a^3}{\mathrm{d}t} = 0, \tag{I.1.13}$$

takes the same form as the first law of thermodynamics, $\mathrm{d}E + p, \mathrm{d}V = 0$. This indicates that the energy and momentum of the Universe are conserved within any comoving region. This result is consistent with the spatial homogeneity assumed at the beginning.

In the following, we examine the different epochs of the Universe according to the evolution of the energy density. We consider a Universe dominated by a fluid characterized by the equation of state

$$w = \frac{p}{\rho}. \tag{I.1.14}$$

Depending on which component dominantly contributes to the energy density of the Universe, the cosmic evolution can be broadly classified into three types. In the first case, relativistic particles such as radiation provide the dominant contribution, and this epoch is referred to as the radiation-dominated (RD) era. In the second case, non-relativistic particles such as matter dominate, and this epoch is called the matter-dominated (MD) era. Finally, when dark energy, such as the cosmological constant Λ, dominates the energy density of the Universe, the corresponding epoch is referred to as the dark-energy-dominated (ΛD) era. Substituting the equation of state (I.1.14) into the continuity equation (I.1.12), and recalling the definition of the Hubble parameter $H \equiv (\dot{a}/a) = \mathrm{d}\ln a/\mathrm{d}t$, we obtain

$$\frac{\mathrm{d}\ln\rho}{\mathrm{d}\ln a} = -3(1+w), \tag{I.1.15}$$

$$\rho \propto a^{-3(1+w)}. \tag{I.1.16}$$

For the radiation-dominated case with $w = 1/3$ and the matter-dominated case with $w = 0$, this relation yields

$$\rho = \begin{cases} \rho_{r,0} a^{-4} & (\text{RD};\ w = 1/3), \\ \rho_{m,0} a^{-3} & (\text{MD};\ w = 0), \end{cases} \tag{I.1.17}$$

where $\rho_{r,0}$ and $\rho_{m,0}$ are integration constants of Eq. (I.1.17), representing the energy densities of radiation and matter at the present temperature T_0. From this, we see that the energy density of matter is diluted inversely with the volume expansion a^3, while that of radiation is further diluted by an additional factor of a due to the redshift-induced stretching of wavelengths, resulting in an overall scaling proportional to a^4.

Furthermore, substituting Eq. (I.1.15) into the Friedmann equation $H = \sqrt{\frac{1}{3m_{\rm pl}^2}\rho}$ (I.1.9), we obtain

$$H \propto \sqrt{\rho} \propto a^{-3(1+w)/2}. \tag{I.1.18}$$

For the case $w = -1$, the Hubble parameter becomes $H \sim$ const.. Using the definition of the Hubble parameter, we can integrate $\mathrm{d}t/a = \mathrm{d}a/a^2 H$ to obtain

$$a \propto -\frac{1}{H\tau}. \tag{I.1.19}$$

On the other hand, integrating $H \equiv (\dot{a}/a) = \mathrm{d}\ln a/\mathrm{d}t$ with respect to t, we find

$$a \propto e^{Ht}, \tag{I.1.20}$$

which shows that during this period the Universe undergoes exponential expansion. Such a spacetime is referred to as de Sitter spacetime.

In contrast, for the radiation-dominated case with $w = 1/3$ and the matter-dominated case with $w = 0$, the scale factor and the conformal time evolve as

$$\dot{a} \propto a^{-\frac{1}{2}(1+3w)}, \tag{I.1.21}$$

$$\tau \propto a^{\frac{1}{2}(1+3w)} = \begin{cases} a & (\text{RD};\ w = 1/3), \\ a^{1/2} & (\text{MD};\ w = 0). \end{cases} \tag{I.1.22}$$

The results obtained so far are summarized in Table. I.1.

epoch	energy density ρ	scale factor $a(\tau)$	scale factor $a(t)$
Radiation($w = 1/3$)	a^{-4}	τ^1	$t^{1/2}$
Matter($w = 0$)	a^{-3}	τ^2	$t^{2/3}$
$\Lambda(w = -1)$	$a^0 = \text{const.}$	$-1/H\tau$	e^{Ht}

Table I.1 Dependence of the energy density ρ on the scale factor a in each cosmological epoch, as well as the relation between the scale factor a and the conformal time τ and their time evolution.

To grasp these results visually, a schematic picture is shown in Fig. I.1. As can be seen from this figure, the Universe initially undergoes a RD epoch, which transitions to a MD at the matter–radiation equality time, when the energy density of matter becomes dominant. Subsequently, after the dark energy–matter equality time, dark energy becomes dominant and the Universe enters the ΛD epoch, which continues until the present time. Strictly speaking, prior to the RD epoch, there may exist an early MD realized by oscillations of the inflaton around the minimum of its potential. However, since we consider prompt preheating in the hybrid inflation scenario discussed later in Chapter III, this early MD is not shown in the schematic picture I.1.

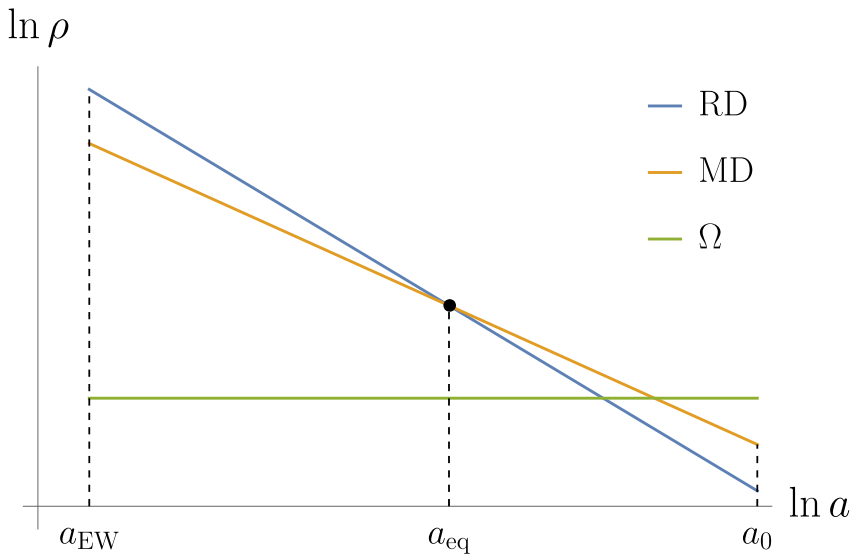

Fig. I.1 Schematic picture of the energy density. The vertical axis represents the energy density ρ, while the horizontal axis denotes the scale factor a, illustrating Eqs. (I.1.15) and (I.1.17). In the RD era ($w = 1/3$), $\rho \propto a^{-4}$ (blue); in the MD era ($w = 0$), $\rho \propto a^{-3}$ (orange); and in the ΛD era ($w = -1$), $\rho \propto a^0 = \text{const.}$ (green). Here, $a_{\rm EW}$ denotes the scale factor at the temperature of the electroweak (EW) phase transition, $T_{\rm EW} \sim 100\,\text{GeV}$; $a_{\rm eq}$ denotes the scale factor at the matter–radiation equality time, corresponding to the temperature $T_{\rm eq} \sim 0.8\,\text{eV}$; and a_0 denotes the scale factor at the present temperature $T_0 \approx 2.7\,\text{K} \approx 2.4 \times 10^{-4}\,\text{eV}$.

I.2 Big Bang cosmology

In the 1940s, George Gamow, together with Hans Bethe and Ralph A. Alpher, proposed the so-called $\alpha\beta\gamma$ theory, which explains the origin of the abundances of light elements such as hydrogen H, helium He, and lithium Li observed in the present Universe not by nuclear fusion inside stars, but by Big Bang nucleosynthesis (BBN) [67]. Subsequently, the redshifted thermal radiation theoretically predicted from this hot Big Bang was discovered as CMB, leading to the great success of Big Bang cosmology. However, within the standard Big Bang cosmology, the energy content of the Universe is dominated by either matter or radiation, and it turns out that extremely special and finely tuned initial conditions are required for the Universe to evolve into its present state. Inflation provides a qualitative resolution to these problems. In inflationary cosmology, an accelerated phase of cosmic expansion is introduced in the early Universe, allowing the present Universe to emerge from generic initial conditions. In this Sec. I.2, after briefly reviewing the thermal history [68–70], of the Universe in the standard Big Bang model based on the Standard Model of particle physics, we pick up two representative problems in the standard Big Bang cosmology, namely the flatness problem and the horizon problem, and explain the associated what is the problem.

I.3 Thermal History

First, the thermal history of the Universe strongly depends on its temperature. In the hot environment immediately after the Big Bang, often referred to as the fireball Universe, the cosmic temperature is extremely high. In such an epoch, all particles in the Standard Model are relativistic ($m - \mu \ll T$), and hence many species of particles are excited in the system. As the Universe expands, the temperature gradually decreases, and some of the Standard Model particles become non-relativistic. Once a given particle becomes non-relativistic ($m - \mu \gg T$), its energy and entropy are transferred to other particle species that remain relativistic. In this manner, as the Universe expands and cools down, the number of relativistic particle species decreases. When these particle species are in thermal equilibrium at temperature T, the distribution function is given by

$$f(\varepsilon) = \frac{1}{e^{(\varepsilon-\mu)/k_{\mathrm{B}}T} \pm 1}, \tag{I.3.1}$$

where ε denotes the energy of each particle species, μ is the chemical potential, and $k_{\mathrm{B}} \approx 8.6 \times 10^{-5}\,\mathrm{eV/K}$ is the Boltzmann constant. The sign $\pm$ corresponds to $+1$ for fermions and -1 for bosons. Hereafter, we set $k_{\mathrm{B}} = 1$. In this case, since the energy density ρ depends only on the magnitude of the momentum $|P|$ through $\varepsilon = \sqrt{|P|^2 + m^2}$,

it can be written as

$$\rho_i = g_i \int \frac{\mathrm{d}P}{(2\pi)^3} \varepsilon f(\varepsilon) = g_i \int \frac{\mathrm{d}|P|}{2\pi^2} \frac{|P|^2 \sqrt{|P|^2 + m_i^2}}{e^{\left(\sqrt{|P|^2+m_i^2}-\mu\right)/T_i} \pm 1}, \tag{I.3.2}$$

where the integral is rewritten in momentum space. Here the subscript i denotes each particle species, and g_i represents the number of internal degrees of freedom. By introducing the dimensionless variable $x = |P|/T$, this expression becomes

$$\rho_i = \frac{g_i T_i^4}{2\pi^2} \int_0^\infty \mathrm{d}x \frac{x^2 \sqrt{x^2 + (m_i/T_i)^2}}{e^{\sqrt{x^2+(m_i/T_i)^2}-\mu/T_i} \pm 1}. \tag{I.3.3}$$

Here, the effective number of relativistic degrees of freedom g_* [69, 70] is introduced, since it will later appear in discussions of the abundance of PBHs and the spectrum of GWs. The evolution of g_* is defined as

$$g_* = \frac{\rho(T)}{\pi^2 T^4/30}, \quad g_{*,s} = \frac{s(T)}{2\pi^2 T^3/45}, \tag{I.3.4}$$

where $s(T)$ denotes the entropy density of the Standard Model plasma, given by

$$s(T) = \frac{\rho(T) + p(T)}{T}. \tag{I.3.5}$$

In the case of complete thermal equilibrium where the chemical potential μ can be neglected, substituting the energy density of each particle species in Eq. (I.3.3) into the definition of the effective relativistic degrees of freedom yields

$$g_* = \frac{\rho(T)}{\pi^2 T^4/30} = \frac{15}{\pi^4} \sum_i g_i \left(\frac{T_i}{T}\right)^4 \int_0^\infty \mathrm{d}x \frac{x^2 \sqrt{x^2 + (m_i/T_i)^2}}{e^{\sqrt{x^2+(m_i/T_i)^2}} \pm 1}. \tag{I.3.6}$$

Furthermore, for non-relativistic particles with $m_i \gg T_i$, their contributions are exponentially suppressed and can be neglected. On the other hand, for relativistic particles with $m_i \ll T_i$, the distribution function can be approximated by the Boltzmann distribution, and by repeated partial integration the integral term evaluates to 6. In this case, one obtains the approximate expression

$$g_* = \sum_{i(\mathrm{boson})} g_i \left(\frac{T_i}{T}\right)^4 + \frac{7}{8} \sum_{i(\mathrm{fermion})} g_i \left(\frac{T_i}{T}\right)^4. \tag{I.3.7}$$

[1]

In the Standard Model, the heaviest particle is the top quark, whose mass is 174 GeV. Therefore, all particles lighter than this are thermally excited for $T \gg \mathcal{O}(100)\,\mathrm{GeV}$, and in such an epoch one has $g_* = g_h + g_g + g_{\mathrm{EW}} + \frac{7}{8}(g_q + g_l) = 106.75$. Here, the internal degrees of freedom are given by $g_h = 1$ for the Higgs boson, $g_g = 16$ for gluons, $g_{\mathrm{EW}} = 11$ for the electroweak gauge bosons, $g_q = 72$ for quarks, and $g_l = 18$ for leptons. However, since there may exist heavy new particles that have not been experimentally confirmed in the high-energy regime far above $\mathcal{O}(100)\,\mathrm{GeV}$, it is also conventional to use an effective value of 150 for the relativistic degrees of freedom. After the spontaneous symmetry breaking of the electroweak interaction at $T_{\mathrm{EW}} \sim 100\mathrm{GeV}$, the gauge bosons mediating the weak force, $W^{\pm}$ and Z, acquire masses. This is referred to as the electroweak phase transition, during which $H^0(125\,\mathrm{GeV})$, $W^{\pm}(80\,\mathrm{GeV})$, $Z(91\,\mathrm{GeV})$, and $t, \bar{t}(174\,\mathrm{GeV})$ become non-relativistic. As a result, $g_h = 1$, $g_W = 6$, $g_Z = 3$, $g_t = 12$ no longer contribute to the effective degrees of freedom, leading to $g_* = g_g + g_\gamma + \frac{7}{8}(60 + g_l) \simeq 86.25$. When the temperature drops below $T_{\mathrm{QCD}} \sim 150\,\mathrm{MeV}$, quarks, which had previously behaved as effectively massless free particles, become confined by gluons and form baryons and mesons through hadronization. This corresponds to a phase transition from the quark phase to the hadron phase, known as the QCD transition. Just before the QCD phase transition, the effective number of particle degrees of freedom is $g_* \simeq 61.75$. After the QCD transition, the thermal bath of the cosmic plasma is populated by baryons and pions, while quarks and gluons no longer contribute to the effective degrees of freedom. Between this epoch and neutrino decoupling as well as electron-positron annihilation, only photons, electrons, and neutrinos contribute, yielding $g_* = g_\gamma + \frac{7}{8}(g_e + g_\nu) = 2 + \frac{7}{8}(2 \cdot 2 + 2 \cdot 3) = 10.75$. At $T \sim 1\,\mathrm{MeV}$, neutrinos decouple from the other particles. Among these species, $e^{\pm}$ possess a relatively large mass, $m_e \sim 0.5\,\mathrm{MeV}$, and thus electron–positron annihilation begins around $T \sim 0.5\,\mathrm{MeV}$. During this annihilation process, photons are emitted and entropy is transferred into the photon. As a consequence, a temperature difference arises between neutrinos and photons at present. As a result, only photons and neutrinos remain as relativistic degrees of freedom, leading to $g_* = g_\gamma + \frac{7}{8} g_\nu \simeq 3.38$. As the temperature decreases further, protons and neutrons that were hadronized during the QCD transition

[1] Here, the factor 7/8 represents the correction for fermionic particles. [2]

$$\int_0^\infty \mathrm{d}x\, x^3 \frac{1}{e^x - 1} = \int_0^\infty \mathrm{d}x\, \frac{e^{-x}}{1 - e^{-x}} = \int_0^\infty \mathrm{d}x\, x^3 \sum_{n=1}^\infty e^{-nx} = \sum_{n=1}^\infty \frac{6}{n^4} = 6\zeta(4) = \frac{\pi^4}{15}, \text{ (Boson)}, \tag{I.3.8}$$

$$\begin{aligned}\int_0^\infty \mathrm{d}x\, x^3 \frac{e^{-x}}{1 + e^{-x}} &= \int_0^\infty \mathrm{d}x\, x^3 \sum_{n=1}^\infty (-1)^{n+1} e^{-nx} = \sum_{m=1}^\infty \left(\int_0^\infty \mathrm{d}x\, x^3 e^{-(2m-1)x} - \int_0^\infty \mathrm{d}x\, x^3 e^{-2mx} \right) \\ &= \sum_{m=1}^\infty \Gamma(4)((2m-1)^{-4} - (2m)^{-4}) = 6\left(1 - \frac{1}{8}\right)\zeta(4) = \frac{7}{8}\frac{\pi^4}{15}, \text{ (Fermion)},\end{aligned} \tag{I.3.9}$$

where ζ denotes the Riemann zeta function, with $\zeta(4) = \pi^4/90$.

undergo nuclear reactions and begin to form light nuclei. This process is known as Big Bang nucleosynthesis (BBN). During this light elements up to Li are produced. At even lower temperatures, the nuclei formed by BBN bind with free electrons to form electrically neutral hydrogen atoms. This process is called recombination. As a result, the number of free electrons that had previously interacted with photons via Thomson scattering is drastically reduced, and photons undergo decoupling. Since photons can then propagate freely, this epoch is referred to as the last scattering or photon decoupling, and the photons scattered just before this epoch, redshifted to the present, are observed as the CMB. The equal-time hypersurface corresponding to the moment when the CMB photons last scattered is called the last scattering surface, which will again play an important role in the discussion of the horizon problem. Subsequently, around 5 meV, the first generation of stars, galaxies, and quasars form in the Universe and begin to emit high-energy photons. These photons reionize the previously electrically neutral atoms, leading to the epoch of reionization.

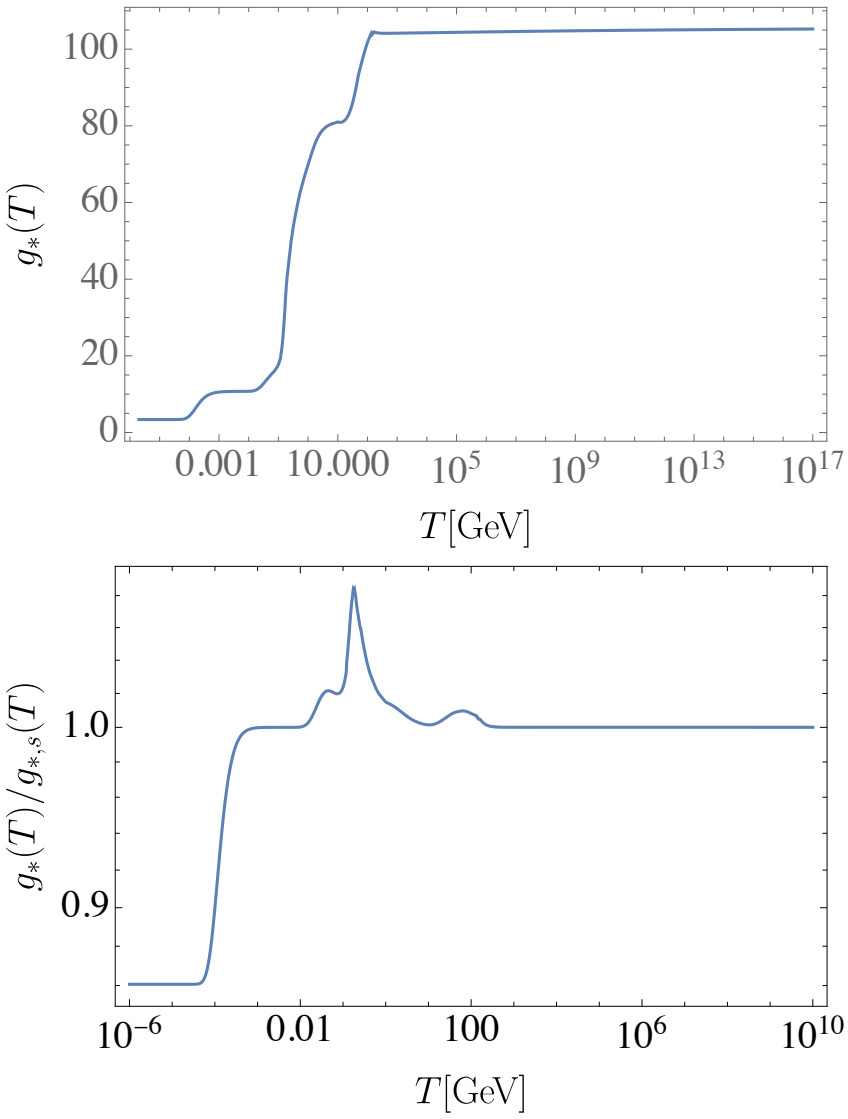

Fig. I.2 Temperature evolution of g_* (I.3.4) (left panel) and of $g_*/g_{*,s}$ (I.3.4) (right panel) [69, 70]. Typical values are, as described above, $T \gg \mathcal{O}(100)\,\text{GeV}$ with $g_* = 106.75$, $T_{\text{EW}} \sim 100\,\text{GeV}$ with $g_* \simeq 86.25$, $T_{\text{QCD}} \sim 150\,\text{MeV}$ with $g_* = 10.75$, and $T \sim 0.5\,\text{MeV}$ with $g_* \simeq 3.38$.

event	temperature T	cosmic time t
EW transition	100 GeV	10^{-11} s
QCD transition	150 MeV	10^{-5} s
Neutrino decoupling	1 MeV	10^{-1} s
$e^{\pm}$ annihilation	500 keV	3 s
BBN	100 keV	3 min
Matter-radiation equality	0.8 eV	60 kyr
Recombination	0.3 eV	280 kyr
Photon decoupling	0.26 eV	380 kyr
Reionization	5 meV	250 kyr
Dark energy-matter equality	0.33 meV	9 Gyr
Present	0.24 meV	13.8 Gyr

Table I.2 Thermal history [69, 70] of the standard Big Bang model. For each event, the corresponding temperature and cosmic time are summarized.

We now turn to two representative problems in the standard Big Bang cosmology, namely the flatness problem and the horizon problem, and explain these inconsistencies.

I.3.1 Flatness problem

In a cosmological model with cosmological constant Λ and spatial curvature K equalt to 0, the energy density is referred to as the critical density. From the Friedmann equations (I.1.9), it is defined as

$$\rho_{\mathrm{c}} = 3m_{\mathrm{pl}}^2 H^2. \tag{I.3.10}$$

The Omega parameter for each component i, defined as the ratio of its energy density to the critical density, is given by

$$\Omega_i = \frac{\rho_i}{\rho_{\mathrm{c}}} = \frac{\rho_i}{3m_{\mathrm{pl}}^2 H^2}. \tag{I.3.11}$$

Similarly, if the curvature parameter K is formally interpreted in terms of an effective energy density and pressure, it can be defined as

$$\rho_{\mathrm{K}} = -\frac{3m_{\mathrm{pl}}^2 K}{a^2}, \quad p_{\mathrm{K}} = \frac{m_{\mathrm{pl}}^2 K}{a^2}. \tag{I.3.12}$$

The corresponding curvature Omega parameter is then defined by

$$\Omega_K = \frac{\rho_K}{\rho_{\mathrm{c}}} = \frac{-K}{a^2 H^2}. \tag{I.3.13}$$

We normalize the scale factor at the present cosmic time t_0 as $a_0 = a(t_0) \equiv 1$. Dividing the Friedmann equations (I.1.9) by H^2,

$$1 - \sum_i \Omega_i = \Omega_K = \frac{-K}{a^2 H^2}, \tag{I.3.14}$$

is obtained, where the time evolution of the scale factor given by Eq. (I.1.21), namely $\frac{1}{a^2 H^2} = \frac{1}{\dot{a}^2} \propto a^{(1+3w)}$, implies that Ω_K is extremely small in the early Universe, as illustrated in Fig. (I.3). Within the standard Big Bang cosmology, no mechanism is provided to explain the origin of this fine-tuning.

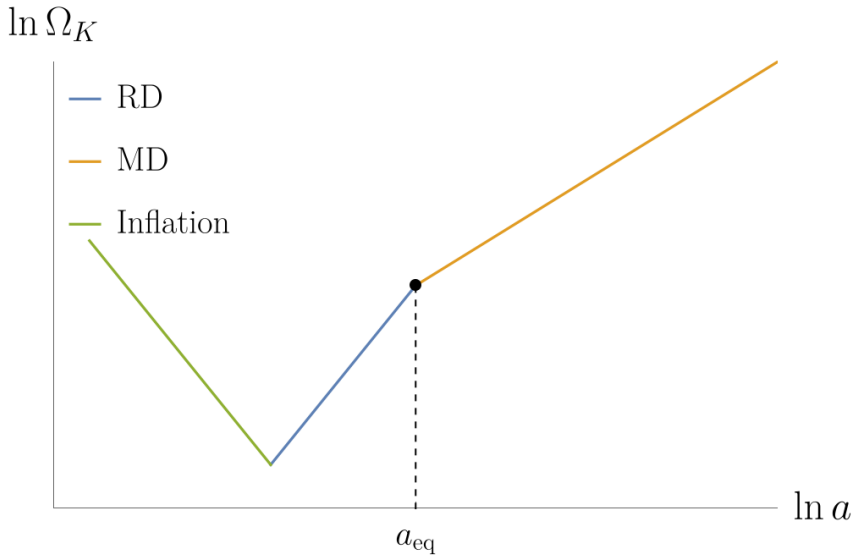

Fig. I.3 Schematic illustration of the flatness problem. The horizontal axis represents the scale factor a, while the vertical axis denotes the curvature Omega parameter $\Omega_K \propto a^{(1+3w)}$. In RD era, the equation of state is $w = 1/3$, corresponding to $\Omega_K \propto a^2$ (blue), whereas in MD era, the equation of state is $w = 0$, corresponding to $\Omega_K \propto a$ (orange). Here, $a_{\rm eq}$ and a_0 denote the scale factors at the matter-radiation equality time and at the present epoch, respectively. Thus, within the Big Bang cosmology, the curvature Omega parameter must be fine-tuned to an extremely small value in the early Universe.

I.3.2 Horizon problem

Here, with respect to the cosmological time t, the conformal time τ, which takes into account the cosmic expansion, is defined as

$$\tau \equiv \int_0^t \frac{\mathrm{d}t'}{a\,(t')} = \int_0^a \frac{\mathrm{d}a}{Ha^2}. \tag{I.3.15}$$

In this context, the causal horizon, namely the maximum distance that light can travel between times t_i and t, is referred to as the particle horizon. Since the null geodesic traced

by light is given by $0 = \mathrm{d}s^2 = -\mathrm{d}t^2 + a(t)^2\mathrm{d}\mathbf{x}^2 = -\mathrm{d}t^2 + a^2(t)\frac{\mathrm{d}r^2}{1-Kr^2}$, the particle horizon is defined as

$$x_p \equiv \int_{r(t_i)}^{r_{\max}(t)} \mathrm{d}r\sqrt{g_{\mathrm{rr}}} = \int_{r(t_i)}^{r_{\max}(t)} \frac{\mathrm{d}r}{\sqrt{1-Kr^2}} = \int_{t_i}^{t} \frac{\mathrm{d}t'}{a\left(t'\right)} = \tau - \tau_i, \tag{I.3.16}$$

which characterizes the region that can be in causal contact. The corresponding physical distance is given by

$$d_p(t) \equiv a(t)x_p(t). \tag{I.3.17}$$

We discuss the horizon problem. Here, $1+z \equiv a_0/a(t) = 1/a(t)$ denotes the cosmological redshift, and $z_{\mathrm{dec}} \sim 1100$. The epoch after the last scattering surface, $0 < z < z_{\mathrm{dec}}$, consists of a MD era followed by a dark-energy-dominated era; however, since the onset of the dark-energy-dominated era occurs at $z_{\Lambda\mathrm{eq}} = (\Omega_{\Lambda 0}/\Omega_{\mathrm{m}0})^{1/3} - 1 < 0.29$ [6], the era after the dark-energy matter equality time can be well approximated as MD era. In this era, $a \propto t^{2/3}$ and $\dot{a} \propto t^{-1/3}$, leading to $H \propto t^{-1} \propto a^{-3/2}$. The horizon size at the time of last scattering is then given by

$$d_H(t_{\mathrm{dec}}) = \frac{1}{H_{\mathrm{dec}}} = \frac{1}{H_0 a_{\mathrm{dec}}^{-3/2}} = H_0^{-1}\left(1+z_{\mathrm{dec}}\right)^{-3/2}. \tag{I.3.18}$$

The angular diameter distance to the last scattering surface, which is currently located at a comoving distance $r_{\mathrm{dec}} = 1/H_0^{-1}$, is defined as the ratio of the physical size of a source to the angle, it subtends for the observer and is given by

$$d_A(t_{\mathrm{dec}}) \equiv a r_{\mathrm{dec}} = \frac{H_0^{-1}}{1+z_{\mathrm{dec}}}. \tag{I.3.19}$$

Therefore, the fraction of the two-dimensional celestial sphere covered by a single horizon patch at last scattering is

$$\frac{d_H(t_{\mathrm{dec}})}{d_A(t_{\mathrm{dec}})} = (1+z_{\mathrm{dec}})^{-1/2} \approx 1/33, \tag{I.3.20}$$

which implies that the number of causally disconnected horizon patches on the two-dimensional sky is

$$\frac{4\pi}{\pi(1/33)^2} \approx 4.4 \times 10^3, \tag{I.3.21}$$

Nevertheless, observations of the CMB indicate that these numerous patches exhibit an extremely uniform temperature, with fluctuations $10^{-5}\,K$. This is the horizon problem.

I.4 Overcoming the problems about Big Bang cosmology

Summarizing the issues of the standard Big Bang cosmology discussed so far, in the flatness problem the horizon scale $(1/aH)^2$ increases monotonically, which implies that the curvature density parameter Ω_K must be extremely small in the early Universe. No explanation has been provided for this fine-tuning. In the horizon problem, the comoving horizon also increases monotonically, so that when go back to the time of CMB decoupling, the Universe is composed of many causally disconnected regions outside the horizon. This makes it impossible to explain why regions that cannot have interacted causally nevertheless exhibit almost identical temperatures with extremely small fluctuations, as observed in the CMB.

In other words, in order to resolve these problems, it suffices to have a period during which the Hubble horizon becomes a decreasing function of time. As a mechanism to achieve this, inflation is introduced. Inflation is a period during which the scale factor a grows exponentially while the Hubble parameter H remains nearly constant. As a result, two points that were initially in causal contact in the early Universe are rapidly separated by inflation, allowing the observed homogeneous and isotropic Universe inferred from CMB observations to be explained. Moreover, even if the curvature had not been extremely small in the early Universe, rapid accelerated expansion would strongly suppress it, thereby reproducing observations. As explained above, to resolve the problems of the standard Big Bang cosmology, it is sufficient that during inflation the comoving Hubble horizon satisfies

$$\frac{\mathrm{d}}{\mathrm{d}t}\frac{1}{aH} < 0. \tag{I.4.1}$$

Proceeding further, since $\frac{\mathrm{d}}{\mathrm{d}t}\frac{1}{aH} = -\ddot{a}/(aH)^2$, this condition is equivalent to

$$\ddot{a} > 0, \tag{I.4.2}$$

namely, a positive second derivative of the scale factor, which implies accelerated expansion. The origin of this acceleration lies in negative pressure. From $\ddot{a} > 0$ and the Friedmann equations (I.1.10), one obtains

$$p < -\frac{1}{3}\rho. \tag{I.4.3}$$

Furthermore, since the Hubble parameter H is approximately constant during inflation, the scale factor can be expressed as

$$a(\tau) \propto -\frac{1}{H\tau}. \tag{I.4.4}$$

In the Big Bang cosmology, the singularity at $\tau = 0$, where $a(\tau) = 0$, does not allow for causal contact. However, once inflation is introduced, this singularity is shifted to $\tau = -\infty$, so that the horizon at the time of CMB decoupling can be causally connected within a finite interval of time.

However, when we go back in time during inflation, resolving the problems of the standard Big Bang cosmology requires that during inflation the comoving horizon τ or the Hubble horizon $1/aH$ exceeds the CMB scale. This condition is conveniently expressed in terms of the e-folding number, which is often used as a time variable during inflation,

$$N(t) \equiv \ln \frac{a_{\rm end}}{a(t)} = \int_t^{t_f} H dt', \tag{I.4.5}$$

$$dN = Hdt, \tag{I.4.6}$$

and it plays an important role in determining the parameters of hybrid inflation discussed in chapter III, as well as in identifying the parameter regions where inflationary parameters evolve under theoretical constraints in chapter VI. Strictly speaking, this condition depends on the details of reheating and the post-inflationary thermal history, so an order-of-magnitude estimate typically yields values from 40 to 60. More precise values will be discussed in individual sections. Here, the subscript end denotes quantities evaluated at the end of inflation, $t = t_{\rm end}$. Furthermore, expressing this in terms of the scalar field ϕ, one obtains

$$N(\phi) = \int_{\phi_{\rm end}}^{\phi} \frac{V}{V_{,\phi}} d\phi, \tag{I.4.7}$$

where the subscript $,\phi$ denotes differentiation with respect to ϕ.

Here we briefly discuss an estimate of the e-folding number required to solve the horizon and flatness problems [71]. When inflation is going backward, resolving the horizon problem requires that during inflation the comoving horizon τ or the Hubble horizon $1/aH$ at horizon crossing exceeds the CMB scale. This ensures that the horizon at the time of CMB decoupling can be causally connected within a finite time, thereby explaining the observed homogeneity of the CMB. Namely,

$$1 = \frac{k_{\rm CMB}}{a_* H_*} = \frac{a_{\rm CMB} H_{\rm CMB}}{a_* H_*} = \frac{a_{\rm CMB} H_{\rm CMB}}{a_{\rm end} H_{\rm end}} \frac{a_{\rm end} H_{\rm end}}{a_{\rm reh} H_{\rm reh}} \frac{a_{\rm reh} H_{\rm reh}}{a_{\rm eq} H_{\rm eq}} \frac{a_{\rm eq} H_{\rm eq}}{a_* H_*}. \tag{I.4.8}$$

Here, the subscript CMB denotes the CMB scale. From the definition of the e-folding number, the first term satisfies $\frac{a_{\rm CMB}}{a_{\rm end}} = e^{-N(k)}$, and since the Hubble parameter H is nearly constant during inflation, one has $H_{\rm CMB}/H_{\rm end} \sim 1$. The subscript reh denotes the end of reheating, which is a brief MD era following inflation. Since this epoch is MD, Eq. (I.1.18) gives $\frac{a_{\rm end}}{a_{\rm reh}} = (\frac{\rho_{\rm end}}{\rho_{\rm reh}})^{-1/3}$. After reheating, during the RD era until matter-

radiation equality, one similarly finds $\frac{a_{\rm reh}}{a_{\rm eq}} = (\frac{\rho_{\rm reh}}{\rho_{\rm eq}})^{-1/4}$. Finally, since the Hubble parameter H can be expressed in terms of ρ via Eq. (I.1.18), one obtains

$$N = \ln\left(\rho_{\rm end}^{1/6}\rho_{\rm reh}^{1/12}\rho_{\rm eq}^{-1/4}\frac{a_{\rm eq}H_{\rm eq}}{a_*H_*}\right). \tag{I.4.9}$$

Moreover, since $H \sim$ const. during inflation, $\rho \propto H^2$ allows us to estimate $\rho_{\rm end} \sim \rho_{\rm CMB}$. For the other epochs, using Eq. (I.3.4), one finds

$$\begin{aligned} N =& -\frac{2}{3}\ln\frac{10^{16}\,\text{GeV}}{\rho_{\rm end}^{1/4}} + \frac{2}{3}\ln 10^{16}\,\text{GeV} - \frac{1}{3}\ln\frac{10^9\,\text{GeV}}{T_{\rm reh}} + \ln\left(\frac{\pi^2 g_*(T_{\rm reh})}{30}\right) \\ &- \ln T_{\rm eq} + \ln\left(\frac{\pi^2 g_*(T_{\rm eq})}{30}\right) + \frac{1}{3}\ln 10^9\text{GeV} + \ln\frac{a_{\rm eq}H_{\rm eq}}{a_*H_*}, \qquad \text{(I.4.10)} \\ \simeq& 56 - \frac{2}{3}\ln\frac{10^{16}\,\text{GeV}}{\rho_{\rm end}^{1/4}} - \frac{1}{3}\ln\frac{10^9\,\text{GeV}}{T_{\rm reh}}. \qquad \text{(I.4.11)} \end{aligned}$$

Here, the comoving horizon at horizon crossing is $a_*H_* = 0.05\,\text{Mpc}^{-1}$. We also evaluate $a_{\rm eq}H_{\rm eq}$ at matter-radiation equality, where $T_{\rm eq} = T_0/a_{\rm eq} \approx 0.8\,\text{eV}$. At equality time, $\rho_r = \rho_{r,0}a^{-4}$ and $\rho_m = \rho_{m,0}a^{-3}$ are equal, yielding the scale factor

$$a_{\rm eq} = \frac{\rho_{r,0}}{\rho_{m,0}}. \tag{I.4.12}$$

The Hubble parameter is then obtained from the total energy density $\rho_t(a_{\rm eq}) = \rho_{r,\rm eq} + \rho_{m,\rm eq}$ as

$$H_{\rm eq} = \sqrt{\frac{1}{3m_{\rm pl}^2}\rho_t(a_{\rm eq})} = \sqrt{\frac{1}{3m_{\rm pl}^2}\left(\rho_{r,0}\left(\frac{\rho_{r,0}}{\rho_{m,0}}\right)^{-4} + \rho_{m,0}\left(\frac{\rho_{r,0}}{\rho_{m,0}}\right)^{-3}\right)}. \tag{I.4.13}$$

Therefore, the scale at matter-radiation equality is given by

$$a_{\rm eq}H_{\rm eq} = \sqrt{\frac{2}{3m_{\rm pl}^2}\frac{\rho_{m,0}^2}{\rho_{r,0}}} \sim 1.0\times10^{-2}\,\text{Mpc}^{-1}, \tag{I.4.14}$$

which we have used here. Consequently, although the precise value depends on details such as reheating, one finds that an e-folding number of approximately $N \sim 60$ is sufficient to solve the horizon problem and to account for the observed homogeneity of the CMB.

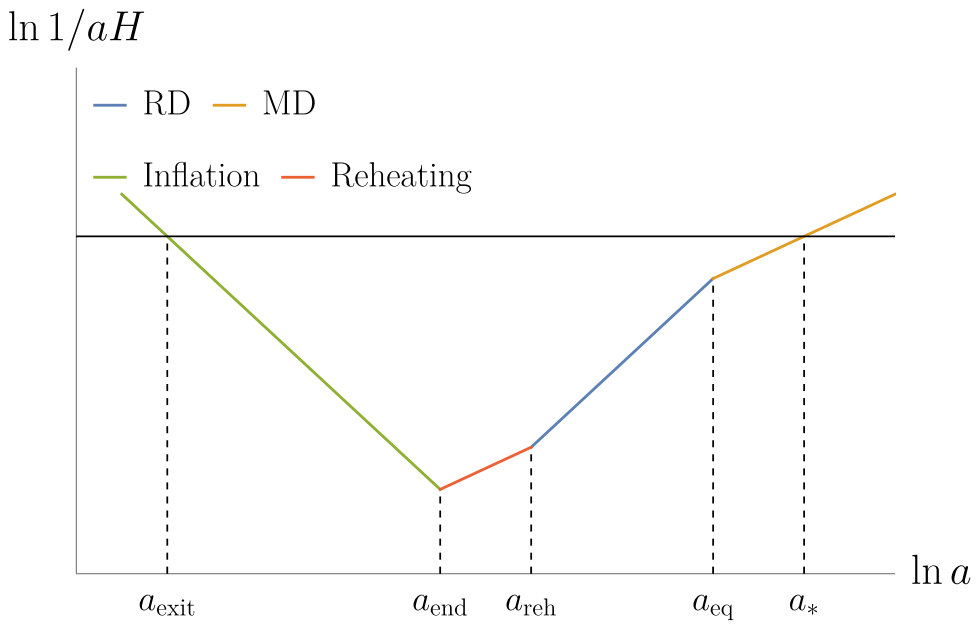

Fig. I.4 Schematic picture of the comoving Hubble scale illustrating the resolution of the horizon problem. The CMB scale (black line) exits the horizon during inflation (green line) at $a_{\rm exit}$ and becomes superhorizon. Inflation ends at $a_{\rm end}$, followed by a brief MD era as reheating era (red line) until $a_{\rm reh}$. Subsequently, a RD era (blue line) continues until the matter-radiation equality time $a_{\rm eq}$, after which the Universe enters another MD era (orange line). The CMB scale re-enters the horizon at recombination.

Turning to the flatness problem, considering the curvature Omega parameter associated with curvature K, avoiding fine-tuning requires only that it be of order $\mathcal{O}(1)$ in the early Universe. One finds

$$\begin{aligned} |\Omega_{K,0}| &= \frac{K}{a_0^2 H_0^2} = \frac{K}{a_{\rm i}^2 H_{\rm i}^2} \frac{a_{\rm i}^2 H_{\rm i}^2}{a_{\rm end}^2 H_{\rm end}^2} \frac{a_{\rm end}^2 H_{\rm end}^2}{a_*^2 H_*^2} \frac{a_*^2 H_*^2}{a_0^2 H_0^2} \\ &= |\Omega_{K,i}| \left(e^{-N} e^{N_{\rm hor}} \frac{a_* H_*}{a_0 H_0} \right)^2 , \end{aligned} \tag{I.4.15}$$

where $N_{\rm hor}$ denotes the minimum e-folding number required to solve the horizon problem, corresponding to the right-hand side of Eq. (I.4.10). Even if the curvature Omega parameter at the onset of inflation satisfies $\Omega_{K,i} \sim \mathcal{O}(1)$, as long as N exceeds $N_{\rm hor}$, the present curvature Omega parameter $|\Omega_{K,0}|$ is exponentially suppressed. Thus, the flatness problem can be resolved without requiring extreme fine-tuning in the early Universe. In other words, once inflation solves the horizon problem, the flatness problem is automatically resolved as well.

I.5 Inflation

So far, we have reviewed the problems inherent in the standard Big Bang cosmology. In this section, we examine how inflation, a period of accelerated expansion that resolves these issues, can be realized. During this inflationary epoch, quantum fluctuations are generated on all length scales, i.e., for all wavenumbers k, on subhorizon scales inside the horizon ($k \gg aH$). Owing to inflation, quantum fluctuations originating on extremely small scales are stretched to large scales. When the Hubble horizon $1/aH$ becomes smaller than the comoving wavelength associated with the quantum fluctuation characterized by k, and the mode exits the horizon, it behaves as a classical fluctuation. Subsequently, when the mode re-enters the horizon after the Big Bang, cosmological perturbations that is curvature perturbations ζ and $\mathcal{R}$, which serve as the seeds of all large-scale structures and inhomogeneities in the Universe, are generated from vacuum quantum fluctuations. Furthermore, combinations of cosmological perturbations generate curvature perturbations, namely fluctuations of the spatial curvature of the Universe around the homogeneous and isotropic FLRW background. These curvature perturbations significantly affect the temperature anisotropies of the CMB and eventually develop into density perturbations that seed large-scale structures such as galaxies and galaxy clusters. Details of the curvature perturbations ζ and $\mathcal{R}$ will be discussed in the next chapter (Ch. II).

I.5.1 Scalar field

Next, we consider a scalar field as the inflaton that drives inflation. As the simplest model of inflation, we focus on the case in which a single scalar field ϕ plays the role of the inflaton. Here, we do not impose specific restrictions on the physical nature of the inflaton, but rather regard it as a parameterization of the time evolution of the energy density during inflation. The action of the scalar field ϕ, minimally coupled to gravity, i.e., without any direct coupling between the inflaton field and the metric, is given in terms of the scalar potential $V(\phi)$ by

$$S = \int \mathrm{d}^4x\sqrt{-g}\mathcal{L} = \int \mathrm{d}^4x\sqrt{-g}\left[\frac{1}{2}m_{\mathrm{pl}}^2 R + \frac{1}{2}g^{\mu\nu}\partial_\mu\phi\partial_\nu\phi - V(\phi)\right], \tag{I.5.1}$$

from which the energy-momentum tensor is obtained as

$$T_{\mu\nu}(\phi) \equiv -\frac{2}{\sqrt{-g}}\frac{\delta S_\phi}{\delta g^{\mu\nu}} = -\frac{\partial\mathcal{L}}{\partial(\partial^\mu\phi)}\partial_\nu\phi + g_{\mu\nu}\mathcal{L} = \partial_\mu\phi\partial_\nu\phi - g_{\mu\nu}\left(\frac{1}{2}\partial^\sigma\phi\partial_\sigma\phi + V(\phi)\right). \tag{I.5.2}$$

If the metric $g_{\mu\nu}$ is taken to be the FLRW metric, the energy-momentum tensor of the scalar field takes the same form as that of a perfect fluid. Accordingly,

$$\rho(\phi) = -T^0_0 = \frac{1}{2}\dot{\phi}^2 + V(\phi), \tag{I.5.3}$$

$$p(\phi) = -T^i_i = \frac{1}{2}\dot{\phi}^2 - V(\phi), \tag{I.5.4}$$

and therefore the equation of state of the scalar field ϕ is given by

$$w(\phi) = \frac{p(\phi)}{\rho(\phi)} = \frac{\frac{1}{2}\dot{\phi}^2 - V(\phi)}{\frac{1}{2}\dot{\phi}^2 + V(\phi)}. \tag{I.5.5}$$

From this expression, if the potential energy $V(\phi)$ dominates over the kinetic energy $\frac{1}{2}\dot{\phi}^2$, the equation-of-state parameter w_ϕ becomes negative, leading to inflationary negative pressure and hence accelerated expansion. Accelerated expansion will be discussed in more detail in the next Sec. (I.5.2). Furthermore, substituting Eqs. (I.5.3) and (I.5.4) into the continuity equation (I.1.12) and the Friedmann equations (I.1.9), one obtains

$$\ddot{\phi} + 3H\dot{\phi} + \frac{\mathrm{d}V(\phi)}{d\phi} = 0, \tag{I.5.6}$$

$$3m_{\mathrm{pl}}^2 H^2 = \frac{1}{2}\dot{\phi}^2 + V(\phi), \tag{I.5.7}$$

which constitute the fundamental equations of the inflaton field.

I.5.2 Slow-roll inflation

When we examined the problems of the standard Big Bang cosmology, we found that introducing a period during which the Hubble horizon decreases resolves these issues, leading to an epoch known as inflation as a resolution. The decrease of the Hubble horizon is equivalent to the condition for accelerated expansion, $\ddot{a} > 0$. By reconsidering this condition in terms of the scalar field ϕ, one can introduce the slow-roll parameters and rewrite the condition in terms of constraints on these slow-roll parameters.

As parameters characterizing the evolution of the Hubble parameter H, the first, second, and third slow-roll parameters are defined as

$$\epsilon \equiv -\frac{\dot{H}}{H^2} = \frac{\dot{\phi}^2}{2m_{\mathrm{pl}}^2 H^2}, \quad \eta \equiv \frac{\dot{\epsilon}}{\epsilon H}, \quad \xi \equiv \frac{\dot{\eta}}{\eta H}, \tag{I.5.8}$$

respectively. In particular, the third slow-roll parameter plays an important role in solving the Mukhanov–Sasaki equation discussed later in Ch. II, and therefore we define the slow-roll parameters up to third order in this paper. Using the slow-roll parameters, the

Friedmann equations (I.1.10) can be rewritten as

$$H^2(1-\epsilon) = \frac{\ddot{a}}{a} = -\frac{1}{6m_{\rm pl}^2}(\rho + 3p), \tag{I.5.9}$$

which implies that accelerated expansion $\ddot{a} > 0$ occurs when $\epsilon < 1$. Furthermore, the de Sitter limit, characterized by $\dot{H} = 0$ and $w = -1$, corresponds to $\epsilon \to 0$. The second slow-roll parameter indicates whether the accelerated expansion is sustained for a sufficiently long period. From Eq. (I.5.6), when $|\eta| \ll 1$, one obtains

$$\left|\ddot{\phi}\right| \ll \left|3H\dot{\phi}\right|, \left|V_{,\phi}\right|, \tag{I.5.10}$$

and thus the fundamental equations during slow-roll inflation reduce to

$$3H\dot{\phi} + \frac{\mathrm{d}V(\phi)}{d\phi} = 0, \tag{I.5.11}$$

$$3m_{\rm pl}^2 H^2 = V(\phi), \tag{I.5.12}$$

Moreover, using the e-folding number (I.4.5), the slow-roll parameters can be expressed as

$$\epsilon = -\frac{d\ln H}{dN}, \tag{I.5.13}$$

$$\eta = -\frac{1}{\dot{\phi}}\frac{\mathrm{d}\dot{\phi}}{\mathrm{d}N} = -\frac{d\ln\left|H_{,\phi}\right|}{dN} = \epsilon - \frac{1}{2\epsilon}\frac{d\epsilon}{dN}, \tag{I.5.14}$$

which represent the fractional rates of change of the Hubble parameter and its derivatives. In addition, one may define the potential slow-roll parameters as

$$\epsilon_V(\phi) \equiv \frac{1}{2}m_{\rm pl}^2\left(\frac{V_{,\phi}}{V}\right)^2, \tag{I.5.15}$$

$$\eta_V(\phi) \equiv m_{\rm pl}^2\frac{V_{,\phi\phi}}{V}, \tag{I.5.16}$$

$$\xi_V^2(\phi) \equiv m_{\rm pl}^4\frac{V_{,\phi}\,V_{,\phi\phi\phi}}{V^2}, \tag{I.5.17}$$

$$\omega_V^3(\phi) \equiv m_{\rm pl}^6\frac{V_{,\phi}^2\,V_{,\phi\phi\phi\phi}}{V^3}, \tag{I.5.18}$$

and the relations between these parameters are approximately given by

$$\epsilon \approx \epsilon_V, \quad \eta \approx \eta_V - \epsilon_V. \tag{I.5.19}$$

Finally, we briefly comment on ultra slow-roll inflation. In regions where the potential is extremely flat, $V(\phi) = V_c$, inflation enters an ultra slow-roll regime, and the slow-roll approximation discussed above breaks down, requiring special care. In this case, the

fundamental equations become

$$\ddot{\phi} + 3H\dot{\phi} = 0, \tag{I.5.20}$$

$$3m_{\rm pl}^2 H^2 = \left(\frac{1}{2}\dot{\phi}^2 + V_c\right), \tag{I.5.21}$$

respectively.

I.6 Example of Inflation model

Here we consider concrete models of inflation and the overall shapes of their potentials. These models will be discussed in the context of the multi-field hybrid inflation model in chapter III, as well as in the top-down theoretical constraints examined in chapter VI. Inflation models can be broadly classified into two types according to the field excursion of the inflaton, and the constraints discussed in chapter VI are imposed on this field excursion and the tensor-to-scalar ratio r.

In the first class, the large field models, the inflaton field starts from a large field value and evolves toward a minimum located at the origin, $\phi = 0$. The field excursion between the point $\phi_{\rm CMB}$, at which the CMB fluctuations are generated, and the end of inflation at $\phi_{\rm end}$ is larger than the Planck scale, namely,

$$\Delta\phi = |\phi_{\rm CMB} - \phi_{\rm end}| > m_{\rm pl}, \tag{I.6.1}$$

as shown above.

In contrast, the second class, the small-field models, is characterized by field evolution over a short distance below the Planck mass scale,

$$\Delta\phi < m_{\rm pl}, \tag{I.6.2}$$

in contrast to the large field case. Potentials that give rise to such small-field evolution often emerge from mechanisms of spontaneous symmetry breaking, where the field rolls from an unstable plateau toward a vacuum.

I.6.1 Example

We first consider the Chaotic Inflation model [72], one of the simplest forms of inflationary potentials, in which a single term dominates the potential. It is referred to as "chaotic" because it does not require special initial conditions: inflation can start from a point randomly distributed by quantum fluctuations, with the energy scale around $V^{1/4} \sim m_{\rm pl}$.

The potential (Fig. I.5) is given by

$$V_{\mathrm{C}}(\phi) = V_0 \left(\frac{\phi}{m_{\mathrm{pl}}} \right)^p , \tag{I.6.3}$$

where p is a parameter. The concrete range of this parameter will be discussed later in chapter VI. In the model originally proposed by Linde, for example in the case $p = 2$, the relation $V^{1/4} = (V_0(\phi/m_{\mathrm{pl}})^2)^{1/4} \sim m_{\mathrm{pl}}$ implies an initial value of the inflaton field $\phi \sim m_{\mathrm{pl}}^3 \gg m_{\mathrm{pl}}$. Thus, the inflaton can start from a very large initial value, and its evolution can take place over a super-Plankian field range. In this case, the tensor-to-scalar ratio r is given by

$$r = 8 \left(\frac{\phi}{p m_{\mathrm{pl}}} \right)^{-2} , \tag{I.6.4}$$

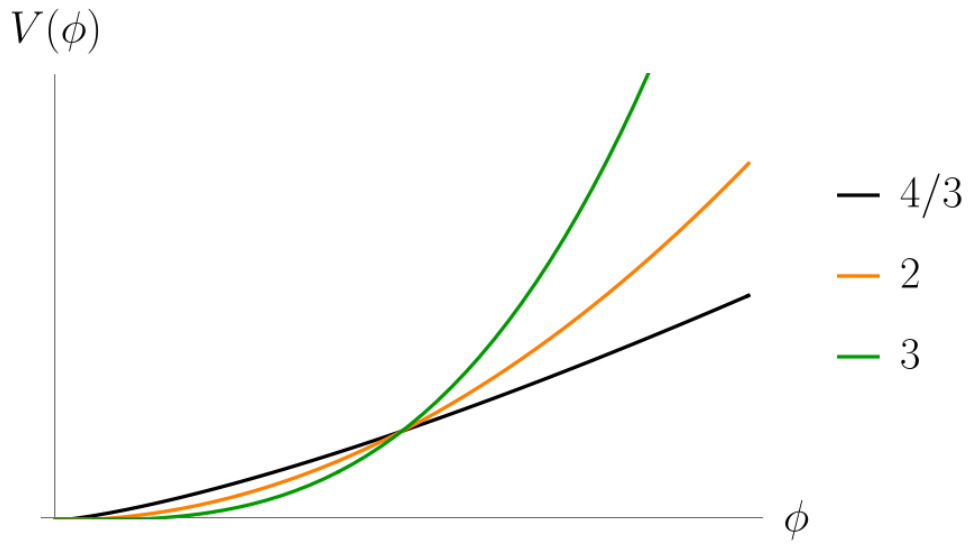

Fig. I.5 Chaotic Inflation Model. This is one of the simplest models described by a simple potential, in which the initial conditions are chaotic. The horizontal axis represents the field ϕ, while the vertical axis represents the potential $V(\phi)$. The parameter p is taken to be representative values often used, such as $4/3, 2$, and 3, which lie within the parameter range considered in this paper and presented in chapter VI.

Next, we consider the Natural Inflation model [73]. This model, proposed by Freese and Adams, employs a pseudo–Nambu–Goldstone boson as the inflaton. The Natural Inflation potential (Fig. I.6) is given by

$$V_{\mathrm{N}}(\phi) = V_0 \left(1 - \cos\left(\frac{\phi}{F} \right) \right) , \tag{I.6.5}$$

where F is a parameter (a decay constant). The potential has a periodicity $\phi \to \phi + 2\pi F$, which naturally realizes the shallow slope of the potential required for inflation. As before, the concrete range of parameters will be discussed in Sec. VI. In this case, the tensor-to-scalar ratio r is given by

$$r = 8\left(\frac{\sin(\phi/F)}{1-\cos(\phi/F)}\right)^2\left(\frac{F}{m_{\rm pl}}\right)^{-2}, \tag{I.6.6}$$

where ϕ depends on F and N, i.e., $\phi = \phi(F, N)$.

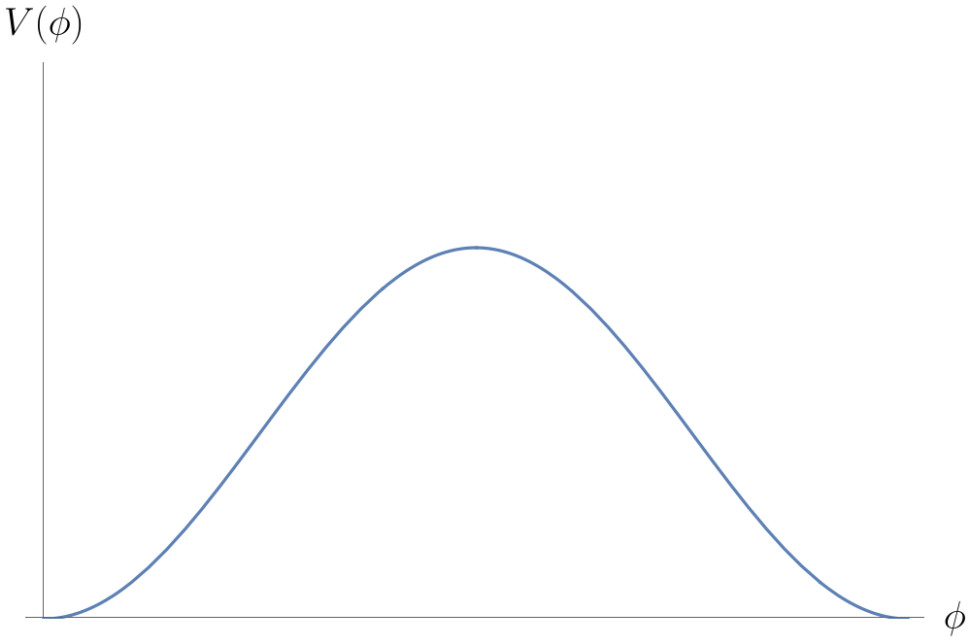

Fig. I.6 Natural Inflation Model. This is one of the simplest potentials in which a gentle slope is naturally realized. The horizontal axis represents the field ϕ, while the vertical axis represents the potential $V(\phi)$. The parameter F is taken to be of order the Planck mass $m_{\rm pl}$ and lies within the parameter range considered in this paper and presented in chapter VI.

Next, we consider the Starobinsky inflation model (Fig. I.7). When the potential energy V dominates over the kinetic energy $\frac{1}{2}\dot{\phi}^2$, the Universe undergoes accelerated expansion, and inflation ends at $\phi_{\rm end}$ when the kinetic energy becomes comparable. The potential is given by

$$V_{\rm S}(\phi) = \frac{3}{4}m^2 m_{\rm pl}^2\left(1 - e^{-\sqrt{2/3}\phi/m_{\rm pl}}\right)^2, \tag{I.6.7}$$

where m denotes the inflaton mass. The CMB fluctuations are generated by quantum fluctuations $\delta\phi$ approximately 60 e-foldings before the end of inflation [74],

$$N_{\rm CMB} = \int_{\phi_{\rm end}}^{\phi_{CMB}} \frac{1}{\sqrt{2\epsilon_V}} d\phi \approx 60, \tag{I.6.8}$$

Furthermore, we consider the α attractor models [75, 76], which include the Starobinsky inflation model as a special case. These models have been proposed and extensively studied in the context of supergravity. Depending on the functional form of the potential V, they are classified into the E-mode and the T-mode. The T-mode of the α attractor model (Fig. I.7) is given by

$$V_\alpha(\phi) = V_0 \tanh^q \left(\frac{\phi}{\sqrt{6\alpha} m_{\rm pl}} \right), \tag{I.6.9}$$

where, in this paper, we adopt $q = 2$ as a representative value.

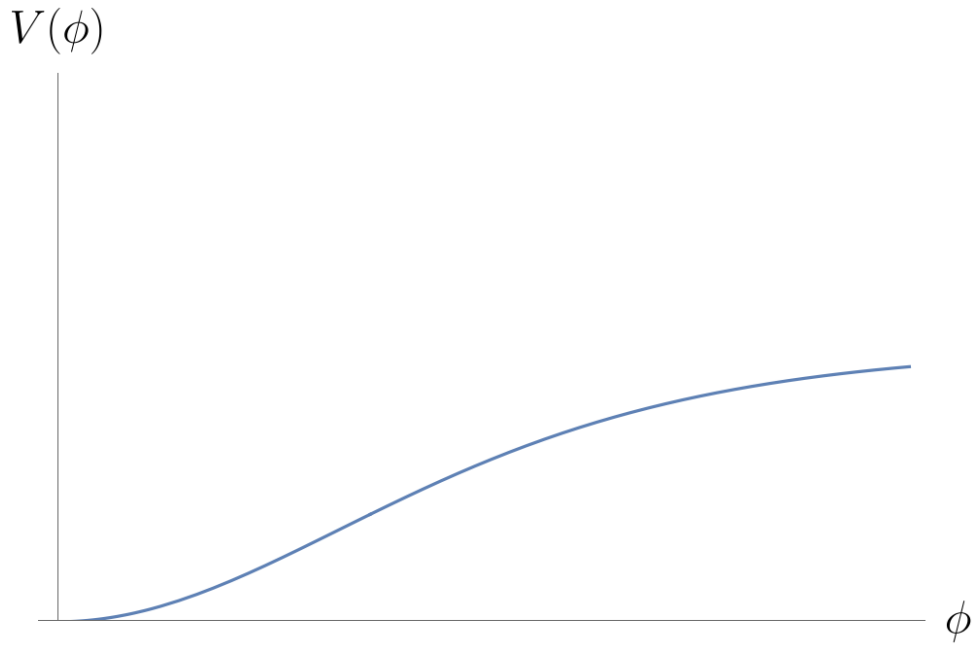

Fig. I.7 α attractor Model T-mode. By transforming to a canonically normalized field, a flat region of the potential is obtained. The horizontal axis denotes the field ϕ, and the vertical axis denotes the potential $V(\phi)$. The parameter α is a free parameter and lies within the parameter range considered in this paper, as presented in chapter VI.

In the Einstein frame, transforming to a canonically normalized field yields an exponentially flat region of the potential. Here, α is a parameter. In this case, the tensor-to-scalar ratio r is given by

$$r = \frac{64}{3\alpha} \left(\sinh \frac{\phi}{\sqrt{6\alpha} m_{\rm pl}} \cosh \frac{\phi}{\sqrt{6\alpha} m_{\rm pl}} \right)^{-2}. \tag{I.6.10}$$

The E-mode of the α attractor model (Fig. I.8) is given by

$$V_\alpha(\phi) = V_0 \left(1 - e^{-\sqrt{2}\phi/\sqrt{3\alpha} m_{\rm pl}} \right)^q, \tag{I.6.11}$$

where, in this paper, we adopt $q = 2$ as a representative value. In this case, the tensor-to-scalar ratio r is given by

$$r = \frac{64}{3\alpha} \frac{e^{-2\sqrt{2}\phi/\sqrt{3\alpha}m_{\rm pl}}}{\left(1 - e^{-\sqrt{2}\phi/\sqrt{3\alpha}m_{\rm pl}}\right)^2}, \tag{I.6.12}$$

where ϕ depends on α and N, i.e., $\phi = \phi(\alpha, N)$.

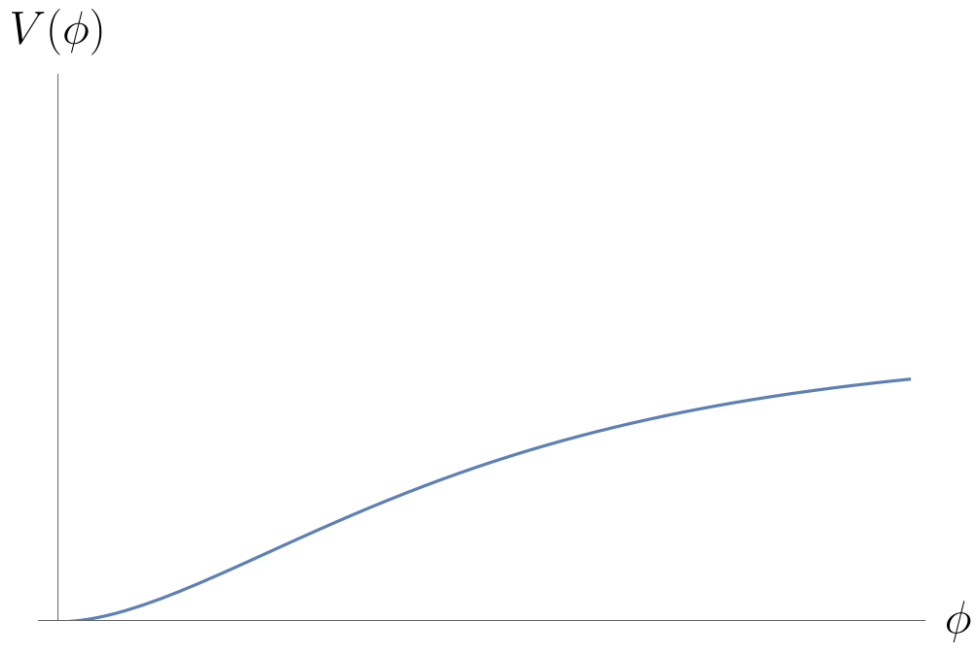

Fig. I.8 α attractor Model E-mode. By transforming to a canonically normalized field, a flat region of the potential is obtained. The horizontal axis denotes the field ϕ, and the vertical axis denotes the potential $V(\phi)$. The parameter α is a free parameter and lies within the parameter range considered in this paper, as presented in Sec. VI.

Next, we consider the running-mass-inflation (RMI) model. When the inflaton mass is renormalized by quantum corrections, it evolves according to the renormalisation group equation. In this case, the potential of the running-mass-inflation model (Fig. I.9) is given by

$$V_{\rm RMI}(\phi) = V_0 \left[1 - \frac{1}{2}\frac{\phi^2}{m_{\rm pl}^2}\left(B - \frac{A}{\left(1 + \alpha \ln \frac{\phi}{m_{\rm pl}}\right)^2}\right)\right], \tag{I.6.13}$$

where α, A, and B are parameters. Further details will be discussed in the next chapter when explaining the potential of hybrid inflation. In this case, the tensor-to-scalar ratio r

is given by

$$r = 8\left(\frac{-\frac{\phi}{m_{\rm pl}}\left(B - \frac{A}{\left(1+\alpha\ln\frac{\phi}{m_{\rm pl}}\right)^2} + \frac{\alpha A}{\left(1+\alpha\ln\frac{\phi}{m_{\rm pl}}\right)^3}\right)}{1 - \frac{1}{2}\frac{\phi^2}{m_{\rm pl}^2}\left(B - \frac{A}{\left(1+\alpha\ln\frac{\phi}{m_{\rm pl}}\right)^2}\right)}\right)^2, \tag{I.6.14}$$

where ϕ depends on α, A, B, and N, i.e., $\phi = \phi(\alpha, A, B, N)$.

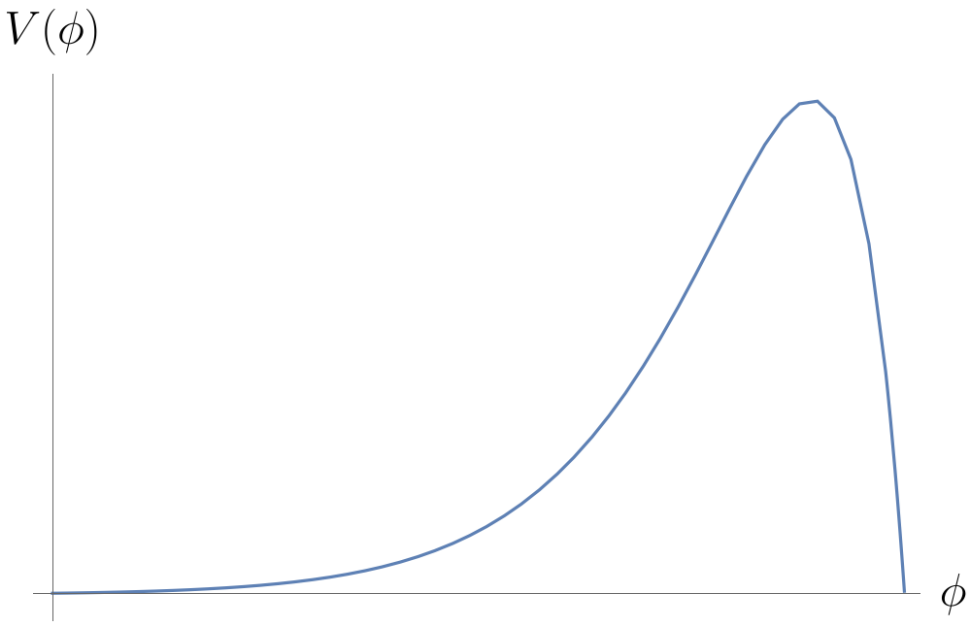

Fig. I.9 Running-mass-inflation Model. By following the renormalisation group equation, the inflaton mass can be kept sufficiently small. The horizontal axis denotes the field ϕ, and the vertical axis denotes the potential $V(\phi)$. The parameters are α, A, and B.

Next, we consider Hilltop Inflation [77]. This model, proposed by Boubekeur and Lyth, realizes inflation near the maximum of the potential. It has been shown that hilltop potentials can be easily obtained from conventional F-term and D-term models, while requiring little fine-tuning. The Hilltop Inflation potential (Fig. I.10) is given by

$$V_{\rm H}(\phi) = V_0(1 - \phi^4/\mu_4^4), \tag{I.6.15}$$

where μ_4 is a parameter. As before, the concrete range of this parameter will be discussed in chapter VI. In this case, the tensor-to-scalar ratio r is given by

$$r = 8\left(\frac{4m_{\rm pl}\phi^3}{\mu_4^4 - \phi^4}\right)^2, \tag{I.6.16}$$

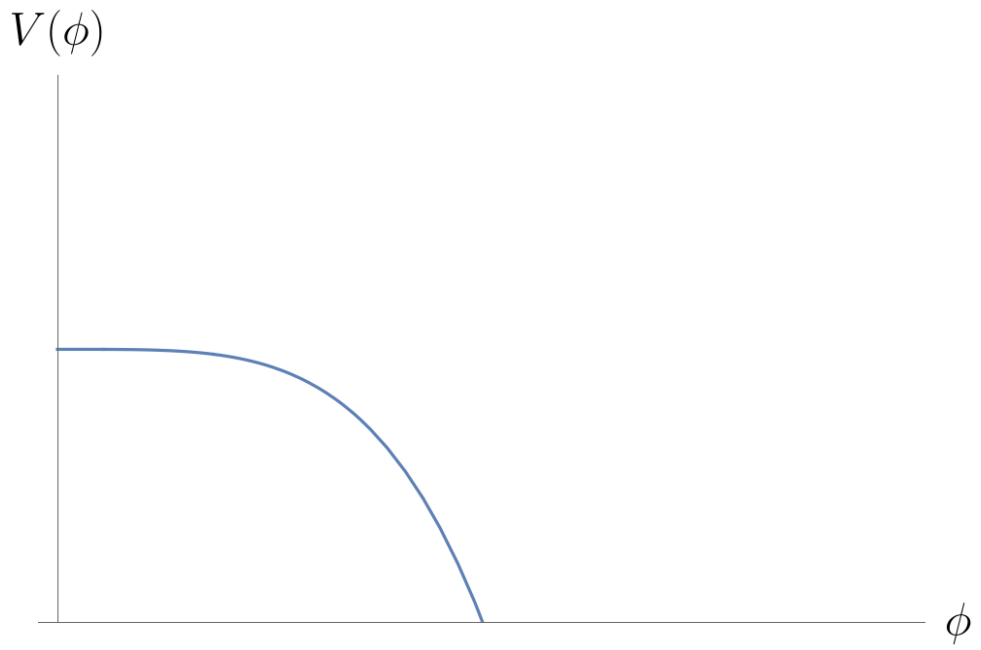

Fig. I.10 Hilltop Inflation Model. This model realizes inflation near the maximum of the potential. The horizontal axis denotes the field ϕ, and the vertical axis denotes the potential $V(\phi)$. The parameter is μ_4, which lies within the parameter range considered in this paper and presented in Sec. VI.

As mentioned at the beginning, inflation can successfully explain the origin of fluctuations that later became the seeds of the present large-scale structure. In the next chapter, we will discuss in detail the calculation of concrete physical quantities derived from these fluctuations.

Chapter II

Curvature perturbation

First, we utilize cosmological perturbation theory to calculate the spectrum of primordial fluctuations generated by quantum fluctuations during inflation. This provides a qualitative explanation of the fundamental mechanism through which inflation transforms microscopic quantum fluctuations into macroscopic seeds for cosmic structure formation. We consider quantum fluctuations about the classical background evolution. These fluctuations $\delta\phi$ lead to local variations in the timing of the end of inflation, resulting in slightly different evolutionary histories across various regions of the universe. Consequently, spatially dependent relative density fluctuations $\delta\rho$ are produced. Comparing the primordial curvature perturbations theoretically predicted by these calculations with cosmic microwave background (CMB) observations has become one of the most powerful methods for testing a number of inflation models proposed by today.

All quantities $X(t, \boldsymbol{x})$ are decomposed into a homogeneous and isotropic background $\bar{X}(t)$ that depends only on cosmic time, and a small spatially dependent perturbation $\delta X(t, \boldsymbol{x})$,

$$X(t, \boldsymbol{x}) = \bar{X}(t) + \delta X(t, \boldsymbol{x}), \tag{II.0.1}$$

where the perturbations are assumed to be sufficiently small compared to the background. Consequently, the Einstein equations can be expanded to linear order as

$$\delta G_{\mu\nu} = 8\pi G \delta T_{\mu\nu}. \tag{II.0.2}$$

The perturbed left-hand side $\delta G_{\mu\nu}$ will be discussed in Sec. II.2, while the right-hand side $\delta T_{\mu\nu}$ will be done in Sec. II.3.

The decomposition into background and perturbations performed here is not unique and depends on the choice of coordinates and gauge. In order to make a meaningful comparison of tensors at two different points on a manifold, one must specify a prescription to identify points in two different spacetimes, which corresponds to a gauge choice. In other words, since the background spacetime and the physical spacetime have different

geometries, a gauge choice is required as a mapping that uniquely relates points between them. This fixes a slicing of the four-dimensional spacetime into spatial hypersurfaces of constant time $t = \text{const.}$ and a threading of worldlines with $x = \text{const.}$. For example, if one chooses a slicing orthogonal to the threading, it corresponds to a homogeneous Universe, and the expansion defined by comoving observers, for whom the momentum density vanishes at their location, becomes isotropic. In general, however, unless a quantity X is gauge-invariant, the value of its perturbation at a given spacetime point is subject to arbitrariness under gauge transformations. Thus, the choice of slicing and threading of the perturbed spacetime is not unique.

II.1 SVT decomposition

The perturbed Einstein equations, which relate metric perturbations to perturbations of the energy–momentum tensor, constitute a coupled system of second-order partial differential equations and are nonlinear, that is, highly complex. Assuming an FLRW background and restricting to the spatially flat case, perturbations can be expanded in Fourier modes with plane waves as eigenfunctions. As a consequence, since different Fourier modes do not interact and evolve independently at linear order, it is convenient to work in Fourier space for a simpler description. Our convention is

$$X_{\mathbf{k}}(t) = A \int \mathrm{d}^3\mathbf{x} X(t,\mathbf{x}) e^{-i\mathbf{k}\cdot\mathbf{x}}, \tag{II.1.1}$$

$$X(t,\mathbf{x}) = B \int \mathrm{d}^3\mathbf{k} X_{\mathbf{k}}(t) e^{i\mathbf{k}\cdot\mathbf{x}}, \tag{II.1.2}$$

which implies the constraint

$$AB = \frac{1}{(2\pi)^3}. \tag{II.1.3}$$

Therefore, there is some arbitrariness in the choice of A and B, and in this work we take $A = 1$ and $B = \frac{1}{(2\pi)^3}$.

Furthermore, by decomposing perturbations into independent scalar (S), vector (V), and tensor (T) components, each type evolves independently and can be treated separately, leading to a significant simplification. When a single Fourier wave vector $\boldsymbol{k}$ is rotated by an angle ψ, a perturbation whose amplitude is multiplied by $e^{im\psi}$ is said to have helicity m. When $\boldsymbol{e}_1, \boldsymbol{e}_2, \boldsymbol{e}_3$ is an orthonormal basis, the basis is taken as the helicity basis $\boldsymbol{e}_\pm = \frac{\boldsymbol{e}_1 \pm i\boldsymbol{e}_2}{\sqrt{2}}, \boldsymbol{e}_3$.

$$X_{\mathbf{k}} \to e^{im\psi} X_{\mathbf{k}}. \tag{II.1.4}$$

The helicities $m = 0, \pm 1, \pm 2$ correspond to the scalar (S), vector (V), and tensor (T) components, respectively.

The linear evolution of perturbations δQ_I from time t_1 to t_2 can then be written as

$$\delta Q_I(t_2, k^i) = \sum_{J=1}^{N} \int \mathrm{d}^3\tilde{k} T_{IJ}(t_2, t_1, k^i, \tilde{k}) \delta Q_J(t_1, \tilde{k}^i), \tag{II.1.5}$$

where T_{IJ} is the transfer matrix derived from the Einstein equations, and the indices I, J label the species of perturbations and run from 1 to N. Under spatial translations $x'^i = x^i + \Delta x^i$ and rotations characterized by $e^{im_I\psi}$, the transfer matrix transforms as

$$T'_{IJ}(t_2, t_1, k^i, \tilde{k}) = e^{i(\tilde{k}_j - k_j)\Delta x^j} T_{IJ}(t_2, t_1, k^i, \tilde{k}), \tag{II.1.6}$$

$$T'_{IJ}(t_2, t_1, k^i, \tilde{k}) = \sum_{J=1}^{N} e^{im_I\psi} T_{IJ}(t_2, t_1, k^i, \tilde{k}). \tag{II.1.7}$$

For translational and rotational invariance to hold for all x^i and m_I, respectively, there can be no coupling between different k modes at linear order. This implies that modes with different helicities do not mix in linear perturbation theory, demonstrating that the SVT decomposition is valid.

II.2 Metric perturbation

We now investigate the right-hand side $\delta G_{\mu\nu}$ of the perturbed Einstein equations. Here, our aim is to determine the evolution of an inhomogeneous and anisotropic spacetime by tracking the evolution of the difference between the physical spacetime and the background spacetime. We consider the background spacetime to be a homogeneous and isotropic FLRW universe, and treat perturbations around the homogeneous background spacetime and the stress-energy tensor of the universe. Specifically, we define perturbations around the homogeneous background solutions of the inflaton $\phi(t)$ and the metric g as

$$\phi(t, \mathbf{x}) = \bar{\phi}(t) + \delta\phi(t, \mathbf{x}), \quad g_{\mu\nu}(t, \mathbf{x}) = \bar{g}_{\mu\nu}(t) + \delta g_{\mu\nu}(t, \mathbf{x}), \tag{II.2.1}$$

and the individual components of the metric are given by

$$g_{00} = -\left(1 + 2\Phi\right), \; g_{0i} = aB_i, \; g_{ij} = a^2\left[\left(1 - 2\Psi\right)\delta_{ij} + 2E_{ij}\right]. \tag{II.2.2}$$

Taking the most general linear perturbation of a spatially flat FLRW metric, the metric becomes

$$\mathrm{d}s^2 = g_{\mu\nu}\mathrm{d}x^\mu \mathrm{d}x^\nu \tag{II.2.3}$$

$$= -(1 + 2\Phi)\mathrm{d}t^2 + 2aB_i \, \mathrm{d}x^i \, \mathrm{d}t + a^2\left[(1 - 2\Psi)\delta_{ij} + 2E_{ij}\right]\mathrm{d}x^i \, \mathrm{d}x^j. \tag{II.2.4}$$

Here, Φ is the three-scalar lapse function, B_i is the shift vector of three-vector, Ψ is the three-scalar spatial curvature perturbation, and E_{ij} is a symmetric and traceless three-tensor representing the spatial shear. We choose slices to be the three-dimensional hypersurfaces of constant time $t = \text{const.}$ and threading to be spatial constant $x_i = \text{const.}$. The intrinsic Ricci scalar curvature of the constant-time hypersurfaces is then given by

$$R_{(3)} = \frac{4}{a^2}\nabla^2\Psi. \tag{II.2.5}$$

The shift vector B_i, which is the metric perturbation in real space, can be decomposed via the SVT decomposition as

$$B_i \equiv \partial_i B - S_i, \tag{II.2.6}$$

into a scalar part B and a vector part S_i, where $\partial^i S_i = 0$. Similarly, the spatial shear E_{ij} can be decomposed as

$$E_{ij} \equiv 2\partial_{ij}E + 2\partial_{(i}F_{j)} + h_{ij}, \tag{II.2.7}$$

into a scalar part E, a vector part F_j, and a tensor part h_{ij}, with the conditions $\partial^i F_i = 0$ and $h^i_i = \partial^i h_{ij} = 0$. Therefore, the metric for scalar perturbations takes the form

$$\mathrm{d}s^2 = -(1+2\Phi)\mathrm{d}t^2 + 2aB_{,i}\ \mathrm{d}x^i\ \mathrm{d}t + a^2\left[(1-2\Psi)\delta_{ij} + E_{,ij}\right]\mathrm{d}x^i\ \mathrm{d}x^j, \tag{II.2.8}$$

where the subscript $,i$ denotes a partial derivative ∂_i. The metric for tensor perturbations is given by

$$\mathrm{d}s^2 = -\mathrm{d}t^2 + a^2\left[\delta_{ij} + h_{ij}\right]\mathrm{d}x^i\ \mathrm{d}x^j. \tag{II.2.9}$$

II.2.1 Gauge transformation

We consider gauge transformations of scalar perturbations of the metric. Let us consider the gauge transformation associated with the coordinate transformation

$$t \to t + \alpha, \tag{II.2.10}$$

$$x^i \to x^i + \delta^{ij}\beta_{,j}, \tag{II.2.11}$$

where α and β are arbitrary functions, since general relativity requires invariance under general coordinate transformations. Under this gauge transformation, the metric transforms as

$$g_{\mu\nu} \to \tilde{g}_{\mu\nu}(\tilde{x}) = \frac{\partial x^\alpha}{\partial \tilde{x}^\mu}\frac{\partial x^\beta}{\partial \tilde{x}^\nu}g_{\alpha\beta}(x). \tag{II.2.12}$$

Here, $\tilde{x}$ denotes the coordinate transformation (II.2.10), which can be written compactly as

$$x^\mu \to \tilde{x}^\mu = x^\mu + \xi^\mu, \tag{II.2.13}$$

with $\xi^\mu = (\alpha, \delta^{ij}\beta_{,j})$. In this case, one finds

$$\begin{aligned}\tilde{g}_{\mu\nu}(x) - g_{\mu\nu}(x) &= \tilde{g}_{\mu\nu}(\tilde{x} - \xi) - g_{\mu\nu}(x) \\ &= (\delta^\alpha_\mu - \xi^\alpha_{,\mu})(\delta^\beta_\nu - \xi^\beta_{,\nu})g_{\alpha\beta}(x) - g_{\mu\nu,\alpha}(x)\xi^\alpha - g_{\mu\nu}(x).\end{aligned} \tag{II.2.14}$$

Approximating this expression to the first order in infinitesimal quantities yields,

$$\tilde{g}_{\mu\nu}(x) - g_{\mu\nu}(x) \simeq -g_{\mu\alpha}(x)\xi^\alpha_{,\nu} - g_{\nu\alpha}(x)\xi^\alpha_{,\mu} - g_{\mu\nu,\alpha}(x)\xi^\alpha. \tag{II.2.15}$$

From this result, calculating each individual component leads to

$$\tilde{g}_{00}(x) - g_{00}(x) \simeq -g_{0\alpha}(x)\xi^\alpha_{,0} - g_{0\alpha}(x)\xi^\alpha_{,0} - g_{00,\alpha}(x)\xi^\alpha \tag{II.2.16}$$

$$\Leftrightarrow (-1 - 2\tilde{\Phi}) - (-1 - 2\Phi) \simeq -2(-1 - 2\Phi)\dot{\alpha}, \tag{II.2.17}$$

$$\tilde{g}_{0i}(x) - g_{0i}(x) \simeq -g_{0\alpha}(x)\xi^\alpha_{,i} - g_{i\alpha}(x)\xi^\alpha_{,0} - g_{0i,\alpha}(x)\xi^\alpha \tag{II.2.18}$$

$$\Leftrightarrow a\tilde{B}_{,i} - aB_{,i} \simeq -(-1 - 2\Phi)\alpha_{,i} - a^2\left((1 - 2\Psi)\delta_{ij} + 2E_{,ij}\right)\delta^{ij}\dot{\beta}_{,j}, \tag{II.2.19}$$

$$\tilde{g}_{ij}(x) - g_{ij}(x) \simeq -g_{i\alpha}(x)\xi^\alpha_{,j} - g_{j\alpha}(x)\xi^\alpha_{,\text{ß}} - g_{ij,\alpha}(x)\xi^\alpha \tag{II.2.20}$$

$$\Leftrightarrow a^2\left(2(\psi - \tilde{\psi})\delta_{ij} + 2(\tilde{E}_{,ij} - E_{,ij})\right) \simeq -2a^2\beta_{,ij} - \dot{a}^2\delta_{ij}\alpha - a^2_{,k}\delta_{ij}\delta^{kl}\beta_{,l}, \tag{II.2.21}$$

which leads to the transformation laws of the scalar perturbations of the metric,

$$\Phi \to \Phi - \dot{\alpha}, \tag{II.2.22}$$

$$B \to B + a^{-1}\alpha - a\dot{\beta}, \tag{II.2.23}$$

$$E \to E - \beta, \tag{II.2.24}$$

$$\Psi \to \Psi + H\alpha. \tag{II.2.25}$$

From these relations, one can construct two gauge-invariant quantities, the Bardeen variables [78],

$$\Phi_B \equiv \Phi - \frac{\mathrm{d}}{\mathrm{d}t}\left[a^2(\dot{E} - B/a)\right], \tag{II.2.26}$$

$$\Psi_B \equiv \Psi - a^2 H(\dot{E} - B/a), \tag{II.2.27}$$

which are indeed gauge-invariant. Explicitly, under a gauge transformation one finds

$$\begin{aligned}\Phi_B \to \tilde{\Phi}_B &= (\Phi - \dot{\alpha}) - \frac{\mathrm{d}}{\mathrm{d}t}\left[a^2((\dot{E} - \dot{\beta}) - (B + \alpha/a - a\dot{\beta})/a)\right] \\ &= \Phi - \frac{\mathrm{d}}{\mathrm{d}t}\left[a^2(\dot{E} - B/a)\right], \qquad \text{(II.2.28)} \\ \Psi_B \to \tilde{\Psi}_B &= (\Psi + H\alpha) - a^2 H((\dot{E} - \dot{\beta}) - (B + \alpha/a - a\dot{\beta})/a) \\ &= \Psi - a^2 H(\dot{E} - B/a), \qquad \text{(II.2.29)}\end{aligned}$$

are indeed gauge-invariant.

II.3 Matter perturbation

We now turn to the right-hand side of the perturbed Einstein equation, $\delta T_{\mu\nu}$. During inflation, the energy content of the Universe is dominantly described by its energy–momentum tensor. Imposing the cosmological principle of homogeneity and isotropy, together with Lorentz invariance, uniquely leads to the same form as that of a perfect fluid. The corresponding matter perturbations are defined as

$$\delta\rho(t, x^i) \equiv \rho(t, x^i) - \bar{\rho}(t), \qquad \text{(II.3.1)}$$

$$\delta p(t, x^i) \equiv p(t, x^i) - \bar{p}(t), \qquad \text{(II.3.2)}$$

which are related to the metric perturbations through the Einstein equations discussed above. After inflation, the total energy–momentum tensor of the Universe takes the form

$$T^{\mu\nu} = (\rho + p)u^\mu u^\nu + g^{\mu\nu}p + \Sigma^{\mu\nu}, \qquad \text{(II.3.3)}$$

and hence the matter perturbations can be written as

$$T^0_0 = -(\bar{\rho} + \delta\rho), \qquad \text{(II.3.4)}$$

$$T^0_i = (\bar{\rho} + \bar{p})av_i, \qquad \text{(II.3.5)}$$

$$T^i_0 = -(\bar{\rho} + \bar{p})\left(v^i - B^i\right)/a, \qquad \text{(II.3.6)}$$

$$T^i_j = \delta^i_j(\bar{p} + \delta p) + \Sigma^i_j, \qquad \text{(II.3.7)}$$

where v^i is defined in terms of the spatial components of the normalized four-velocity u^μ as $v^i \equiv u^i/u^0$. Explicitly, the four-velocity is given by

$$u_\mu \equiv (-1 - \Phi, av_i),\ u^\mu \equiv (1 - \Phi, (v^i - B^i)/a), \qquad \text{(II.3.8)}$$

and Σ^i denotes the anisotropic stress components of the energy–momentum tensor.

II.3.1 Gauge transformation

In the same way before, when the coordinate transformation is given by Eq. (II.2.10), the energy–momentum tensor transforms as

$$T^{\mu}_{\nu}(x) \to \tilde{T}^{\mu}_{\nu}(x) = \frac{\partial \tilde{x}^{\mu}}{\partial x^{\alpha}} \frac{\partial x^{\beta}}{\partial \tilde{x}^{\nu}} T^{\alpha}_{\beta}(x), \tag{II.3.9}$$

and hence, in complete analogy with the case of metric perturbations, one finds

$$\tilde{T}^{\mu}_{\nu}(x) - T^{\mu}_{\nu}(x) \simeq T^{\alpha}_{\nu}(x)\xi^{\mu}_{,\alpha} - T^{\mu}_{\alpha}(x)\xi^{\alpha}_{,\nu} - T^{\mu}_{\nu,\alpha}(x)\xi^{\alpha}, \tag{II.3.10}$$

where ξ^{μ} denotes the gauge transformation. Evaluating each component explicitly, we obtain

$$\tilde{T}^{0}_{0}(x) - T^{0}_{0}(x) \simeq T^{\alpha}_{0}(x)\xi^{0}_{,\alpha} - T^{0}_{\alpha}(x)\xi^{\alpha}_{,0} - T^{0}_{0,\alpha}(x)\xi^{\alpha} \tag{II.3.11}$$

$$\Leftrightarrow -\delta\rho - (-\delta\tilde{\rho}) \simeq (\dot{\bar{\rho}} + \dot{\delta\rho})\alpha, \tag{II.3.12}$$

$$\tilde{T}^{0}_{i}(x) - T^{0}_{i}(x) \simeq T^{\alpha}_{i}(x)\xi^{0}_{,\alpha} - T^{0}_{\alpha}(x)\xi^{\alpha}_{,i} - T^{0}_{i,\alpha}(x)\xi^{\alpha} \tag{II.3.13}$$

$$\Leftrightarrow (\bar{\rho} + \bar{p})a(\tilde{v}_i - v_i) \simeq \left((\bar{p} + \delta p)\delta^{k}_{i} + \Sigma^{k}_{i}\right)\alpha_{,k} + (\bar{\rho} + \delta\rho)\alpha_i, \tag{II.3.14}$$

$$\tilde{T}^{i}_{j}(x) - T^{i}_{j}(x) \simeq T^{\alpha}_{j}(x)\xi^{i}_{,\alpha} - T^{i}_{\alpha}(x)\xi^{\alpha}_{,j} - T^{i}_{j,\alpha}(x)\xi^{\alpha} \tag{II.3.15}$$

$$\Leftrightarrow \delta\tilde{p}\delta^{i}_{j} + \tilde{\Sigma}^{i}_{j} - \delta p\delta^{i}_{j} - \Sigma^{i}_{j} \simeq \bar{p}\delta^{k}_{j}\delta^{il}\beta_{,lk} - \bar{p}\delta^{i}_{k}\delta^{kl}\beta_{,lj} - \bar{p}_{,\alpha}\delta^{i}_{j}\xi^{\alpha}, \tag{II.3.16}$$

from which the gauge transformation properties of each perturbation variable follow as

$$\delta\rho \to \delta\rho - \dot{\bar{\rho}}\alpha, \tag{II.3.17}$$

$$\delta p \to \delta p - \dot{\bar{p}}\alpha, \tag{II.3.18}$$

$$\delta q \to \delta q + (\bar{\rho} + \bar{p})\alpha, \tag{II.3.19}$$

$$\delta\Sigma \to \delta\Sigma. \tag{II.3.20}$$

Here $\delta q^{i} \equiv (\bar{\rho} + \bar{p})av^{i}$. Therefore, similarly to the metric sector, the gauge-invariant quantities are

$$\delta p_{\rm en} \equiv \delta p - \frac{\dot{\bar{p}}}{\dot{\bar{\rho}}}\delta\rho, \tag{II.3.21}$$

$$\delta\rho_m \equiv \delta\rho - 3H\delta q, \tag{II.3.22}$$

which are indeed gauge-invariant quantities. Explicitly, under a gauge transformation,

$$\delta p_{\rm en} \to \delta\tilde{p}_{\rm en} = (\delta p - \dot{\bar{p}}\alpha) - \frac{\dot{\bar{p}}}{\dot{\bar{\rho}}}(\delta\rho - \dot{\bar{\rho}}\alpha), \tag{II.3.23}$$

$$\delta\rho_m \to \delta\tilde{\rho}_m = (\delta\rho - \dot{\bar{\rho}}\alpha) - 3H(\delta q + (\bar{\rho} + \bar{p})\alpha), \tag{II.3.24}$$

demonstrating their gauge invariance. In deriving these expressions, we have used the fact that $\dot{\bar{\rho}}$ is a background quantity and satisfies the Bianchi equation, $\dot{\bar{\rho}} = 3H(\bar{\rho} + \bar{p})$.

II.4 Linear Einstein equation and gauge fixing

Up to this point, in Sec. II.2 we have expanded, at linear order, the metric perturbations associated with the left-hand side of the Einstein equation, $\delta G_{\mu\nu}$, while in Sec. II.3 we have similarly expanded the matter perturbations associated with the right-hand side, $\delta T_{\mu\nu}$. In this section, building on these results, we derive the linearized perturbed Einstein equations and reduce them to four partial differential equations. In addition, we derive the perturbed continuity equations and reduce them to two partial differential equations.

From the metric perturbation (II.2.2), the Christoffel symbols are obtained as

$$\Gamma^0_{00} = \frac{1}{2}g^{0\nu}\Big(g_{0\nu,0} + g_{0\nu,0} - g_{00,\nu}\Big) = \dot{\Phi}, \tag{II.4.1}$$

$$\Gamma^0_{0i} = \frac{1}{2}g^{0\nu}\Big(g_{0\nu,i} + g_{i\nu,0} - g_{0i,\nu}\Big) = \Phi_{,i} + \dot{a}\, B_i, \tag{II.4.2}$$

$$\begin{aligned}\Gamma^0_{ij} &= \frac{1}{2}g^{0\nu}\Big(g_{i\nu,j} + g_{j\nu,i} - g_{ij,\nu}\Big) \\ &= -a\, B_{(i,j)} + a\dot{a}\Big((1 - 2\Psi - 2\Phi)\delta_{ij} + 2E_{ij}\Big) - a^2\Big(\dot{\Psi}\,\delta_{ij} - \dot{E}_{ij}\Big),\end{aligned} \tag{II.4.3}$$

$$\begin{aligned}\Gamma^i_{00} &= \frac{1}{2}g^{i\nu}\Big(g_{0\nu,0} + g_{0\nu,0} - g_{00,\nu}\Big) \\ &= \frac{1}{a}\Big(HB^i + \dot{B}^i + \frac{1}{a}\delta^{ij}\Phi_{,j}\Big),\end{aligned} \tag{II.4.4}$$

$$\begin{aligned}\Gamma^i_{0j} &= \frac{1}{2}g^{i\nu}\Big(g_{0\nu,j} + g_{j\nu,0} - g_{0j,\nu}\Big) \\ &= \frac{1}{a}\,\delta^{ik}B_{(k,j)} + H\delta^i{}_j - \dot{\Psi}\,\delta^i{}_j + \dot{E}^i{}_j,\end{aligned} \tag{II.4.5}$$

$$\begin{aligned}\Gamma^i_{jk} &= \frac{1}{2}g^{i\nu}\Big(g_{j\nu,k} + g_{k\nu,j} - g_{jk,\nu}\Big) \\ &= -\dot{a}\, B^i\delta_{jk} - 2\delta^i_{(j}\Psi_{,k)} + 2E^i{}_{(j,k)} + \delta^{il}\Big(\Psi_{,l}\delta_{jk} - E_{jk,l}\Big).\end{aligned} \tag{II.4.6, II.4.7}$$

From these expressions, one can straightforwardly compute the Ricci tensor $R_{\mu\nu}$, the Ricci scalar R, and hence the Einstein tensor $G_{\mu\nu}$. On the other hand, from the matter perturbations (II.3.4), one finds

$$\delta T_{00} = \delta\rho, \tag{II.4.8}$$

$$\delta T_{i0} = -\Big(\delta q + (\bar{\rho} + \bar{p})B^i\Big), \tag{II.4.9}$$

$$\delta T_{0i} = -\delta q, \tag{II.4.10}$$

$$\delta T_{ij} = a^2(\delta p\delta_{ij} + \delta\Sigma_{ij}), \tag{II.4.11}$$

and therefore the linearized perturbation Einstein equations are given by

$$3H\Big(\dot{\Psi}+H\Phi\Big)+\frac{k^2}{a^2}\Big[\Psi+H\Big(a^2\dot{E}-aB\Big)\Big]=-\frac{1}{2m_{\rm pl}^2}\,\delta\rho, \tag{II.4.12}$$

$$\dot{\Psi}+H\Phi=-\frac{1}{2m_{\rm pl}^2}\,\delta q, \tag{II.4.13}$$

$$\ddot{\Psi}+3H\dot{\Psi}+H\dot{\Phi}+\Big(3H^2+2\dot{H}\Big)\Phi=\frac{1}{2m_{\rm pl}^2}\Big(\delta p-\frac{2}{3}k^2\delta\Sigma\Big), \tag{II.4.14}$$

$$\Big(\partial_t+3H\Big)\Big(\dot{E}-B/a\Big)+\frac{\Psi-\Phi}{a^2}=\frac{1}{m_{\rm pl}^2}\,\delta\Sigma. \tag{II.4.15}$$

Furthermore, the linearized perturbed continuity equations are obtained as

$$\dot{\delta\rho}+3H(\delta\rho+\delta p)=\frac{k^2}{a^2}\delta q+(\bar{\rho}+\bar{p})[3\dot{\Psi}+k^2(\dot{E}+B/a)]\,, \tag{II.4.16}$$

$$\dot{\delta q}+3H\delta q=-\delta p+\frac{2}{3}k^2\delta\Sigma-(\bar{\rho}+\bar{p})\Phi\,. \tag{II.4.17}$$

II.5 Vector perturbation

For completeness, we also derive here the gauge transformation of the vector part of the metric perturbations for $\xi^\mu=(0,\beta^i)$. The metric of the vector part is given by

$$\mathrm{d}s^2=-\mathrm{d}t^2+2aS_i\mathrm{d}x^i\mathrm{d}t+a^2\left[\delta_{ij}+2F_{(i,j)}\right]\mathrm{d}x^i\mathrm{d}x^j, \tag{II.5.1}$$

and, in same with the scalar case, computing each component yields

$$\tilde{g}_{0i}(x)-g_{0i}(x)\simeq-g_{0\alpha}(x)\xi^\alpha_{,i}-g_{i\alpha}(x)\xi^\alpha_{,0}-g_{0i,\alpha}(x)\xi^\alpha \tag{II.5.2}$$

$$\Leftrightarrow 2a(\tilde{S}_i-S_i)\simeq-a^2\left(\delta_{ij}+2F_{(i,j)}\right)\delta^{ij}\dot{\beta}_k, \tag{II.5.3}$$

$$\tilde{g}_{ij}(x)-g_{ij}(x)\simeq-g_{i\alpha}(x)\xi^\alpha_{,j}-g_{j\alpha}(x)\xi^\alpha_{,ß}-g_{ij,\alpha}(x)\xi^\alpha \tag{II.5.4}$$

$$\Leftrightarrow 2a^2\left(\partial_{(i}\tilde{F}_{j)}-\partial_{(i}F_{j)}\right)\simeq-2a^2(\beta_{i,j}-\beta_{j,i})-(a^2\delta_{ij})_{,k}\zeta^k, \tag{II.5.5}$$

from which the vector-type metric perturbations transform as

$$S_i\to S_i+\alpha\dot{\beta}_i, \tag{II.5.6}$$

$$F_i\to F_i-\beta_i. \tag{II.5.7}$$

In this case, a gauge-invariant quantity is given by

$$\dot{F}_i+S_i/a\to\dot{\tilde{F}}_i+\tilde{S}_i/a=\dot{F}_i-\dot{\beta}_i+(S_i+a\dot{\beta}_i)/a, \tag{II.5.8}$$

and indeed this quantity is found to be gauge-invariant. The linearized perturbed Einstein equations for the vector modes are then

$$\dot{\delta q_i} + 3H\delta q_i = k^2\delta\Sigma_i\,, \tag{II.5.9}$$

$$k^2(\dot{F}_i + S_i/a) = \frac{2}{m_{\rm pl}^2}\,\delta q_i\,. \tag{II.5.10}$$

In the case $\delta\Sigma_i = 0$, the right-hand side of the first equation vanishes, implying that $\delta q = \mathrm{Exp}\left[-3\int H\mathrm{d}t\right] = a^{-3}$, and hence it decays due to the cosmic expansion. Consequently, the right-hand side of the second equation also decays with the same a^{-3} scaling, and therefore the vector gauge-invariant quantity on the left-hand side also approaches $\to 0$ as the universe expands and never becomes dominant. For this reason, vector perturbations are not important and will not be considered further here.

II.6 Curvature perturbation

Fixing a gauge makes calculations technically simpler, but it carries the risk of including unphysical gauge degrees of freedom, known as gauge artifacts, which are induced by coordinate transformations. Therefore, although the computation of gauge-invariant quantities is technically more complicated, it has the advantage that only physical degrees of freedom are treated. For this reason, we construct gauge-invariant quantities from appropriate combinations of the gauge-invariant metric perturbations and the gauge-invariant matter perturbations.

We first consider an energy-density uniform slicing defined by $\delta\rho = 0$, i.e., a hypersurface on which there are no fluctuations in the energy density. The curvature fluctuations on an iso-density hypersurface, which measure the spatial curvature of a uniform-density hypersurface, are defined as

$$-\zeta \equiv \Psi + \frac{H}{\dot{\bar{\rho}}}\delta\rho, \tag{II.6.1}$$

and on a uniform-density hypersurface with $\delta\rho = 0$, it is clear that ζ coincides with Ψ, which is related to the three-dimensional spatial curvature $R_{(3)}$ (II.2.5). Under a gauge transformation, we find

$$\begin{aligned} -\zeta \to -\tilde{\zeta} &= (\Psi + H\alpha) + \frac{H}{\dot{\bar{\rho}}}(\delta\rho + \dot{\bar{\rho}}\alpha) \\ &= \Psi + \frac{H}{\dot{\bar{\rho}}}\delta\rho, \end{aligned} \tag{II.6.2}$$

showing that ζ is gauge-invariant.

Next, we consider a slicing orthogonal to the worldlines of comoving observers, namely the comoving slicing. In this case, comoving observers are in free fall, and the expansion defined by them is isotropic. The comoving curvature perturbation, which corresponds to the spatial curvature on a comoving hypersurface, is defined as

$$\mathcal{R} \equiv \Psi - \frac{H}{\bar{\rho}+\bar{p}}\delta q = \Psi + H\frac{\delta\phi}{\dot{\phi}}, \tag{II.6.3}$$

and on a comoving hypersurface with $\delta\phi = 0$, $\mathcal{R}$ coincides with Ψ. Under a gauge transformation, we obtain

$$\begin{aligned}\mathcal{R} \to \tilde{\mathcal{R}} &= (\Psi + H\alpha) - \frac{H}{\bar{\rho}+\bar{p}}(\delta q + (\bar{\rho}+\bar{p})a) \\ &= \Psi - \frac{H}{\bar{\rho}+\bar{p}}\delta q,\end{aligned} \tag{II.6.4}$$

and hence $\mathcal{R}$ is also gauge-invariant.

Finally, we consider the spatially flat slicing defined by $\Psi = 0$. In this case, the fluctuation Q can be defined as

$$Q = \delta\phi + \frac{\dot{\phi}}{H}\Psi = \frac{\dot{\phi}}{H}R, \tag{II.6.5}$$

which becomes an important quantity when studying the time evolution of curvature perturbations in multi-field models. In fact, in the multi-field case, perturbations can be decomposed into adiabatic and isocurvature components, and one finds that they are not conserved even on superhorizon scales.

The quantities ζ and $\mathcal{R}$ are related through the linearized Einstein equations. Substituting the continuity equation (I.1.12) into the definition of the curvature perturbation on the uniform-density (II.6.1), and furthermore noting that on superhorizon scales the inflaton fluctuation is frozen, $\delta\phi = 0$, one finds

$$-\zeta = \mathcal{R} + \frac{k^2}{(aH)^2}\frac{2\bar{\rho}}{3(\bar{\rho}+\bar{p})}\Psi_{\mathrm{B}}, \tag{II.6.6}$$

which implies that on superhorizon scales ($k \ll aH$) the second term is suppressed, so that $-\zeta \sim \mathcal{R}$ and both become time independent.

II.6.1 Curvature perturbation in the case of single barotropic fluid

Above, we have seen that on superhorizon scales ($k < aH$) the uniform-density gauge curvature perturbation ζ coincides with the comoving curvature perturbation $\mathcal{R}$. This

is an important property of curvature perturbations in single-field models. Next, we show that when there are only adiabatic modes, the curvature perturbation is exactly conserved on superhorizon scales [79, 80]. For example, in single-field inflationary models, the perturbation ζ does not evolve in time outside the horizon ($k \ll aH$).

Here, the stress-energy tensor is given by

$$T^{\mu\nu} = (\rho + p)u^\mu u^\nu + g^{\mu\nu}p, \tag{II.6.7}$$

where the four-velocity u^μ is defined as

$$u^\mu = \frac{1}{a}(\delta^\mu_0 + v^\mu). \tag{II.6.8}$$

Furthermore, from the continuity equation $\nabla_\mu T^\mu_{\nu=0} = 0$, we obtain

$$\dot{\delta\rho} = -3H(\rho + \delta p) + 3\dot{\Psi}(\bar{\rho} + \bar{p}), \tag{II.6.9}$$

where the pressure perturbation is decomposed as

$$\delta p = \delta p_{\rm nad} + c_s^2 \delta\rho, \quad c_s^2 = \frac{\delta p_{\rm ad}}{\delta\rho}, \tag{II.6.10}$$

into an adiabatic component $\delta p_{\rm ad}$ and a non-adiabatic component $\delta p_{\rm nad}$. Taking the uniform-density gauge,

$$\delta\rho = 0, \quad \Psi = \zeta, \tag{II.6.11}$$

we examine the time evolution of the uniform-density curvature perturbation. From Eq. (II.6.9), which follows from the continuity equation, we find

$$\dot{\zeta} = \frac{H}{\bar{\rho} + \bar{p}} \delta p_{\rm nad}, \tag{II.6.12}$$

and hence, in the adiabatic case $\delta p_{\rm nad} = 0$, it vanishes and ζ is exactly conserved in time.

Next, for the comoving curvature perturbation, we choose for simplicity the Newtonian gauge, in which the perturbations satisfy $B = E = 0$. In this gauge, the (i, j) components of the Einstein equations yield

$$\Psi = \Phi, \tag{II.6.13}$$

and by adding the $(0, 0)$ and (i, i) components, we obtain

$$\Psi'' + 6\mathcal{H}\Psi' + (2\mathcal{H}' + 4\mathcal{H})\Psi - \nabla^2\Psi = -a^2 V' \delta\phi / m_{\rm pl}^2, \tag{II.6.14}$$

where the prime denotes a derivative with respect to the conformal time τ, and the Hubble parameter is defined as $\mathcal{H} = a'/a = aH$. Adding the background Klein–Gordon equation

and the $(0, i)$ component of the Einstein equations, we further obtain

$$\Psi' + \mathcal{H}\Psi = \phi'\delta\phi/2m_{\rm pl}^2 = \epsilon\mathcal{H}^2\frac{\delta\phi}{\phi'}. \tag{II.6.15}$$

Therefore, on superhorizon scales,

$$\Psi \simeq \epsilon H\frac{\delta\phi}{\dot{\phi}}, \tag{II.6.16}$$

$$\mathcal{R} = \Psi + H\frac{\delta\phi}{\dot{\phi}} = (1+\epsilon)H\frac{\delta\phi}{\dot{\phi}} \simeq H\frac{\delta\phi}{\dot{\phi}} \propto \frac{H^2}{2\pi\dot{\phi}}(-\tau)^{\eta-3\epsilon}, \tag{II.6.17}$$

and hence its time evolution is given by

$$\frac{1}{H}\frac{{\rm d}\ln\mathcal{R}_k}{{\rm d}t} = -2\epsilon + (\eta-\epsilon) + (\eta-3\epsilon)\left(\frac{-1}{H\tau}\right)\frac{d(-\tau)}{dt} = 0, \tag{II.6.18}$$

showing that, as in the case of ζ, the curvature perturbation remains conserved in time for adiabatic perturbations.

II.6.2 Curvature perturbation in the case of multi-field

Unlike the single-field case discussed above, in the multi-field case one must consider not only adiabatic perturbations along the inflaton trajectory but also isocurvature perturbations orthogonal to the trajectory. Let us therefore define the adiabatic condition in multi-field models [81] as

$$\Gamma_{x,y} \equiv \frac{\delta x}{\dot{x}} - \frac{\delta y}{\dot{y}} = 0, \tag{II.6.19}$$

where the condition $\Gamma = 0$ characterizes adiabatic. Here x and y denote arbitrary quantities that can be expressed in terms of the inflaton fields. For example, in the single-field case discussed above,

$$\Gamma_{x,y} = \frac{\delta\phi}{\dot{\phi}} - \frac{\delta\phi}{\dot{\phi}} = 0, \tag{II.6.20}$$

which manifestly satisfies the adiabatic condition, and consequently the curvature perturbation is conserved and does not evolve in time on superhorizon scales. In contrast, in the multi-field case one generally finds

$$\Gamma_{\phi\chi} = \frac{\delta\phi}{\dot{\phi}} - \frac{\delta\chi}{\dot{\chi}} \neq 0, \tag{II.6.21}$$

so that the adiabatic condition is violated and non-adiabatic perturbations must be taken into account.

In this situation, we introduce perturbations Q on the background trajectory in field space. In the single-field case, the inflaton simply evolves along a one-dimensional

background trajectory, and only the adiabatic component $Q_{\rm ad}$ along the trajectory is present. In the multi-field case, however, in addition to the component $Q_{\rm ad}$ along the trajectory, there also appears a component Q_s orthogonal to the trajectory. These can be decomposed as

$$Q_{\rm ad} = \cos\theta\delta\phi + \sin\theta\delta\chi \quad \text{(along)}, \tag{II.6.22}$$

$$Q_s = -\sin\theta\delta\phi + \cos\theta\delta\chi \quad \text{(normal)}, \tag{II.6.23}$$

where θ denotes the angle between $Q_{\rm ad}$ and the inflaton field perturbation $\delta\phi$. A schematic picture illustrating these features is shown in Fig. II.1.

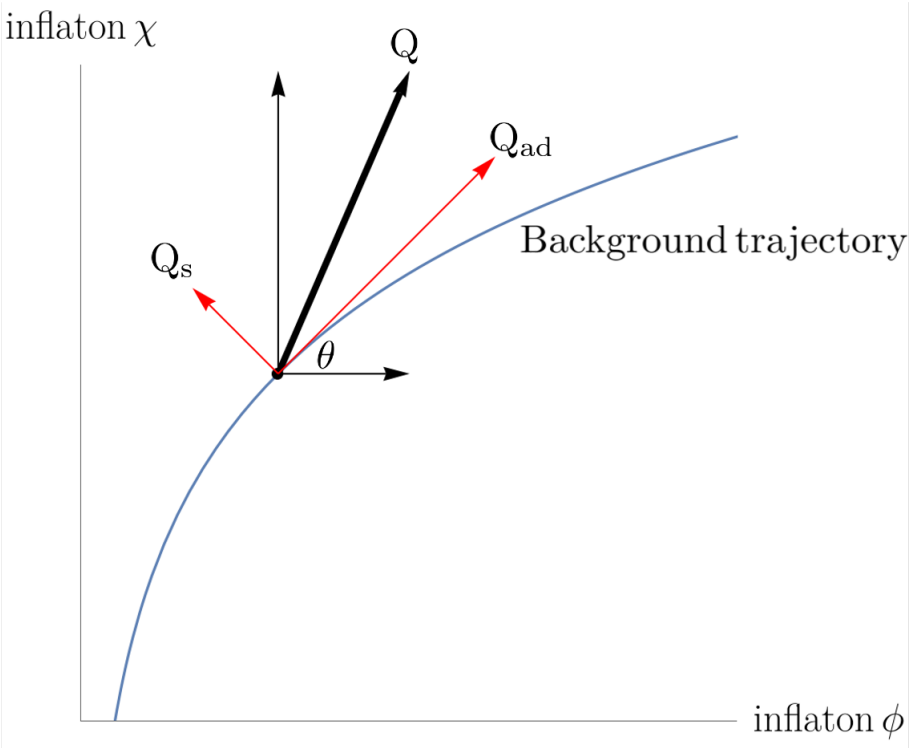

Fig. II.1 Schematic picture of the evolution of perturbations in the multi-field case. Here we consider two fields, ϕ and χ, and the phase space spanned by ϕ on the horizontal axis and χ on the vertical axis. When the adiabatic condition is violated in a multi-field setup, the perturbation Q (black thick arrow) possesses not only a component $Q_{\rm ad}$ along the background trajectory (blue) but also a component Q_s perpendicular to it (red arrows), so that the curvature perturbation evolves in time even on superhorizon scales [82].

In this case, choosing the spatially flat gauge $\Psi = 0$, the curvature perturbation is given by

$$\zeta = \frac{H}{\dot\rho}\delta\rho = \frac{-H}{\sqrt{\dot\phi^2 + \dot\chi^2}}Q_{\rm ad}, \tag{II.6.24}$$

$$\dot{\zeta} = -2\frac{H\dot{\theta}}{\sqrt{\dot{\phi}^2 + \dot{\chi}^2}}Q_s + \mathcal{O}\left(\frac{k}{aH}\right)^2, \tag{II.6.25}$$

where the first term, which does not appear in the single-field case, arises in the multi-field scenario. As a result, even on superhorizon scales one finds $\dot{\zeta} \neq 0$, indicating that the curvature perturbation evolves in time.

II.7 Tensor perturbation

Tensor perturbations can give rise to gravitational waves. In particular, in scenarios where curvature perturbations are enhanced on small scales, the curvature perturbations can source tensor perturbations through the source term in their evolution equations, potentially leading to a gravitational-wave spectrum with an amplitude large enough to be observable. Here, we investigate the equations satisfied by tensor perturbations.

II.7.1 Metric perturbation

The metric for tensor perturbations is given by

$$\mathrm{d}s^2 = -\mathrm{d}t^2 + a^2\left[\delta_{ij} + h_{ij}\right]\mathrm{d}x^i\ \mathrm{d}x^j. \tag{II.7.1}$$

In this case, the gauge transformation is

$$h_{ij} \to \tilde{h}_{ij} = h_{ij}, \tag{II.7.2}$$

showing that the tensor perturbation is gauge-invariant. Decomposing it into eigenmodes of the spatial Laplacian, we write

$$h_{ij} = h(t)e_{ij}^{(+,\times)}(x), \tag{II.7.3}$$

where $+$ and $\times$ denote the two polarization states, e_{ij} are the eigenmodes of the spatial Laplacian satisfying $\nabla^2 e_{ij} = -k^2 e_{ij}$, and k is the comoving wavenumber.

II.7.2 Matter perturbation

In general, as a good approximation, the anisotropic stress Σ_{ij} can be neglected. In the absence of anisotropic stress, the perturbed Einstein equation is given by

$$\ddot{h} + 3H\dot{h} + \frac{k^2}{a^2}h \simeq 0, \tag{II.7.4}$$

which describes the evolution of gravitational waves in an expanding universe.

In general, when photons are scattered, linear polarization is generated in the direction perpendicular to the scattering plane. However, if the Universe were perfectly homogeneous and isotropic, such polarization would cancel out on average. In reality, as observed in the CMB, small temperature fluctuations exist, so that polarization remains and exhibits spatial variations. Among the vector fields describing the polarization direction, the modes whose curl vanishes are referred to as E-modes. On the other hand, even if temperature fluctuations were absent, the presence of gravitational waves would induce different redshifts, and in this case, as well, polarization would remain and exhibit anisotropies in the CMB. In this situation, the polarization vector field contains a rotational component whose divergence vanishes, and such modes are called B-modes. Gravitational waves generated during inflation decay as the Universe expands. Nevertheless, at the time of recombination, it may leave imprints characteristic of B-mode polarization of the CMB.

II.8 Power spectrum

Up to this point, we have derived the equations satisfied by the perturbations and the corresponding gauge-invariant quantities for each component of the SVT decomposition. In this section, we introduce several physical quantities that are important for the direct observations. First, assuming statistical isotropy and that the dependence is only on the distance r, the two-point correlation function is defined as

$$\xi_{\mathcal{R}}(r) \equiv \langle \mathcal{R}(\mathbf{x})\mathcal{R}(\mathbf{x}+\mathbf{r}) \rangle \,, \tag{II.8.1}$$

and its Fourier transform defines the power spectrum,

$$P_{\mathcal{R}}(\bar{k}) = A \int \mathrm{d}^3\mathbf{r}\xi_{\mathcal{R}}(r)e^{-i\mathbf{k}\cdot\mathbf{r}}. \tag{II.8.2}$$

II.8.1 Scalar Power spectrum

As stated at the beginning of this chapter, adopting the convention $A = 1$ and $B = \frac{1}{(2\pi)^3}$, the power spectrum is defined through

$$\langle \mathcal{R}_{\mathbf{k}}\mathcal{R}_{\mathbf{k}'} \rangle \equiv A^2 \left\langle \int \mathrm{d}^3\mathbf{x}\mathcal{R}(\mathbf{x})e^{-i\mathbf{k}\cdot\mathbf{x}} \int \mathrm{d}^3\mathbf{x}'\mathcal{R}(\mathbf{x}')e^{-i\mathbf{k}'\cdot\mathbf{x}'} \right\rangle \tag{II.8.3}$$

$$= (2\pi)^3\delta\left(\mathbf{k}+\mathbf{k}'\right) P_{\mathcal{R}}(k), \tag{II.8.4}$$

and its variance is given by

$$\sigma_R^2 \equiv \left\langle \mathcal{R}^2(x) \right\rangle = \xi_{\mathcal{R}}(0) \coloneqq \int \mathrm{dlnk}\mathcal{P}_{\mathcal{R}}(\mathrm{k}), \tag{II.8.5}$$

from which the power spectrum of curvature perturbations is defined as

$$\mathcal{P}_{\mathcal{R}}(\mathrm{k}) = \frac{k^3}{2\pi^2} P_{\mathcal{R}}(\mathrm{k}). \tag{II.8.6}$$

Furthermore, the dimensionless power spectrum of scalar perturbations is obtained as

$$\mathcal{P}_{\mathrm{s}} \equiv \mathcal{P}_{\mathcal{R}} = \frac{k^3}{2\pi^2} P_{\mathcal{R}}(k), \tag{II.8.7}$$

from which one can see that it is scale independent. The scalar spectral index, which characterizes the scale dependence of the power spectrum, is defined by

$$n_{\mathrm{s}} - 1 \equiv \frac{\mathrm{d}\ln \mathcal{P}_{\mathrm{s}}}{\mathrm{d}\ln k}, \tag{II.8.8}$$

and for $n_{\mathrm{s}} = 1$, $\mathcal{P}_s$ is independent of k, corresponding to a scale-invariant spectrum. The running of the spectral index is defined as

$$\alpha_{\mathrm{s}} \equiv \frac{\mathrm{d}n_{\mathrm{s}}}{\mathrm{d}\ln k}, \tag{II.8.9}$$

and furthermore, in Hybrid inflation III, the running of the running,

$$\beta_{\mathrm{s}} \equiv \frac{\mathrm{d}^2 n_{\mathrm{s}}}{\mathrm{d}\ln k^2} = \frac{\mathrm{d}\alpha_{\mathrm{s}}}{\mathrm{d}\ln k}, \tag{II.8.10}$$

also appears, so we therefore introduce it here.

II.8.2 Tensor spectrum

Similarly to the scalar case, when considering the power spectra of the two polarization modes h_+ and $h_\times$, we discuss them collectively by representing each mode with a single symbol h without a polarization index.

$$\langle h_{\mathbf{k}} h_{\mathbf{k}'} \rangle = (2\pi)^3 \delta\left(\mathbf{k} + \mathbf{k}'\right) P_h(k), \tag{II.8.11}$$

$$\mathcal{P}_h = \frac{k^3}{2\pi^2} P_h(k), \tag{II.8.12}$$

and hence the power spectrum of tensor perturbations is given by the sum of the dimensionless power spectra of the two polarizations,

$$\mathcal{P}_{\mathrm{t}} \equiv 2\mathcal{P}_h. \tag{II.8.13}$$

Furthermore, the tensor spectral index is defined as

$$n_{\mathrm{t}} \equiv \frac{\mathrm{d}\ln \mathcal{P}_{\mathrm{t}}}{\mathrm{d}\ln k}, \tag{II.8.14}$$

which is an important physical quantity related to the tilt of primordial gravitational waves. A more detailed discussion of gravitational waves will be given in Chapter V.

II.9 Gauge choice and curvature perturbation

As discussed in Sec. II.6, the gauge choice determines which gauge-invariant quantities are most convenient to work with. Here we introduce several types of gauge fixing. In particular, the Newtonian gauge and the flat gauge will also be used later in the context of hybrid inflation.

- The uniform density gauge is defined by imposing $\delta\rho = 0$. For simplicity, one often additionally sets $E = 0$. In this gauge, the gauge-invariant quantity ζ is related to the metric perturbation Ψ as $\zeta = -\Psi$, which makes this gauge convenient for describing perturbations on superhorizon scales.

- The comoving gauge is defined by $\delta\phi = 0$. In this case, the gauge-invariant quantity $\mathcal{R}$ is related to the metric perturbation Ψ as $\mathcal{R} = \Psi$. As already seen, ζ and $\mathcal{R}$ are related by Eq. (II.6.6). We will study this gauge in more detail in Sec. II.10, where we follow the quantization procedure and solve the corresponding equations, and explicitly derive the scalar power spectrum.

- The flat gauge is defined by $\Psi = E = 0$. In this case, the gauge-invariant quantities Q and R are related. As discussed in Sec. II.6.2, in the multi-field case curvature perturbations are not conserved even on superhorizon scales due to the presence of isocurvature components. This gauge will also reappear in the discussion of hybrid inflation in Chapter III.

- The Newtonian gauge is defined by $B = E = 0$. This gauge will also be used again in the discussion of hybrid inflation in Chapter III.

II.10 Comoving gauge and Quantization

Here we consider a single-field inflationary model, whose action is given by Eq. (I.5.1) as

$$S = \frac{1}{2}\int \mathrm{d}^4x\sqrt{-g}\left[m_{\mathrm{pl}}^2\mathcal{R} - (\nabla\phi)^2 - 2V(\phi)\right], \tag{II.10.1}$$

and we choose the comoving gauge. The metric g_{ij} and the scalar field ϕ are related to the curvature perturbation $\mathcal{R}$, thereby fixing the spacetime parameters as

$$\delta\phi = 0, \quad g_{ij} = a^2 \left[(1 - 2\mathcal{R})\delta_{ij} + h_{ij}\right], \tag{II.10.2}$$

As is evident from the definition of the gauge choice, the inflaton field ϕ is unperturbed, and all scalar perturbations are parameterized by the fluctuation $\mathcal{R}$. Here the tensor perturbation h_{ij} is transverse, $\partial_i h_{ij} = 0$, and traceless, $h^i_i = 0$. An important property of $\mathcal{R}$ is that, as discussed in Sec. II.6.1, it remains constant outside the horizon in the adiabatic case, so that it suffices to evaluate the correlation functions of $\mathcal{R}$ at horizon crossing. Moreover, the Einstein equations relate the remaining metric perturbations Φ and B to $\mathcal{R}$ via

$$g_{00} = -(1 + 2\Phi), \quad g_{0i} = aB_i. \tag{II.10.3}$$

In this way, all perturbations are related to $\mathcal{R}$, and henceforth we describe the equations of motion entirely in terms of $\mathcal{R}$.

II.10.1 Quantization

As discussed in Sec. II.6.1, in the single-field case, the gauge-invariant curvature perturbation $\mathcal{R}$ is conserved outside the horizon. Therefore, a given mode of $\mathcal{R}$ can be computed at horizon exit without considering the physics during reheating or until its re-entry. Using the gauge-invariant curvature perturbation $\mathcal{R}$, we expand the action of single slow-roll inflation up to second order, derive the equation of motion for $\mathcal{R}$ from the action, and analyze the slow-roll approximate solution. Furthermore, $\mathcal{R}$ is promoted from a classical quantity to a quantum operator, and by imposing canonical commutation relations on this operator, boundary conditions for the mode functions are given. By defining the vacuum state, a unique vacuum is selected, and the mode functions are completely fixed. Finally, the power spectrum of curvature perturbations at horizon crossing is computed. Since the inflationary potential considered in this chapter III contains regions where the slow-roll approximation is violated, the simple slow-roll approximation alone is insufficient. Therefore, even in the ultra-slow-roll regime, we include second-order slow-roll parameters, which are often neglected in conventional approximations, to expand the Mukhanov-Sasaki equation and obtain approximate solutions. Ultimately, the power spectra and scale dependence of both scalar and tensor perturbations are calculated.

Here we adopt the Arnowitt-Deser-Misner (ADM) formalism [83], which decomposes spacetime into time and space. The metric is written as

$$\mathrm{d}s^2 = -N^2\,\mathrm{d}t^2 + \hat{\gamma}_{ij}\left(\mathrm{d}x^i + N^i\mathrm{d}t\right)\left(\mathrm{d}x^j + N^j\mathrm{d}t\right), \tag{II.10.4}$$

where N is the lapse function, N^i is the shift vector, and $\hat{\gamma}_{ij}$ is the three-dimensional spatial metric. In this decomposition, the metric components are

$$g_{\mu\nu} = \begin{pmatrix} -N^2 + N_i N^i & N_i \\ N_i & \hat{\gamma}_{ij} \end{pmatrix}, \quad g^{\mu\nu} = \begin{pmatrix} -N^{-2} & N^{-2} N^i \\ N^{-2} N^i & \hat{\gamma}^{ij} - N^{-2} N^i N^j \end{pmatrix}, \tag{II.10.5}$$

so that $\sqrt{-g} = \sqrt{-\det g_{\mu\nu}} = N\sqrt{\hat{\gamma}}$. This allows one to compute the connection, Ricci tensor, and Ricci scalar, leading to

$$R = R^{(3)} + K_{ij} K^{ij} - K^2, \tag{II.10.6}$$

where K_{ij} is the extrinsic curvature, i.e., the momentum conjugate of the spatial metric,

$$K_{ij} = \nabla_i n_j = \frac{1}{2N} \left(\partial_t \hat{\gamma}_{ij} - \hat{D}_i N_j - \hat{D}_j N_i \right), \tag{II.10.7}$$

where $\hat{D}_i$ denotes the covariant derivative with respect to $\hat{\gamma}_{ij}$ and $n_j \equiv N_j / \sqrt{N^2}$ denotes the unit normal vector to the hypersurface. In addition to this ADM decompose, the spatial metric can be decomposed into trace and traceless parts as

$$\hat{\gamma}_{ij} = a^2(t) e^{2\psi} \gamma_{ij}, \tag{II.10.8}$$

where ψ is the scalar perturbation associated with spatial curvature, and γ_{ij} is a traceless tensor.

In the comoving gauge, there is no need to consider perturbations of the inflaton, and the comoving curvature perturbation R is directly related to Ψ. In the ADM formalism, Action Eq. (II.10.1) becomes [1]

$$\begin{aligned} S = \frac{1}{2} \int \mathrm{d}^4 x \sqrt{-g} \Big[& N m_{\mathrm{pl}}^2 R^{(3)} - 2NV + N^{-1} \left(E_{ij} E^{ij} - E^2 \right) \\ & + N^{-1} \left(\dot{\phi} - N^i \partial_i \phi \right)^2 - N g^{ij} \partial_i \phi \partial_j \phi - 2V \Big]. \end{aligned} \tag{II.10.9}$$

The Lagrangian is

$$\mathcal{L} = \sqrt{-g} \left[N R^{(3)} + \frac{1}{N} \left(E_{ij} E^{ij} - E^2 \right) + \frac{1}{N} \dot{\phi}^2 - 2NV(\phi) \right], \tag{II.10.10}$$

with

$$E_{ij} \equiv \frac{1}{2} \left(\dot{g}_{ij} - \nabla_i N_j - \nabla_j N_i \right), \quad E = E^i_i. \tag{II.10.11}$$

[1] We have the action $g^{\mu\nu} \partial_\mu \phi \partial_\nu \phi = \frac{-1}{N^2} \dot{\phi}^2 + 2 \frac{N^i}{N^2} \dot{\phi} \partial_i \phi + g^{ij} \partial_i \phi \partial_j \phi - \frac{N^i N^j}{N^2} \partial_i \phi \partial_j \phi = \frac{-1}{N^2} \left(\dot{\phi} - N^i \partial_o \phi \right)^2 + g^{ij} \partial_i \phi \partial_j \phi$ and $\sqrt{-g} = N\sqrt{\hat{\gamma}}$ where the three-dimensional spatial metric $\hat{\gamma}_{ij}$ is relabeled as g_{ij}.

To solve the constraint equations, we perform the SVT decomposition

$$N \equiv 1 + \alpha, \tag{II.10.12}$$

$$N_i \equiv \Psi_{,i} + \tilde{N}_i, \tag{II.10.13}$$

where $\Psi_{,i}$ is the scalar part and $\tilde{N}_i$ is a vector with $\tilde{N}_{i,i} = 0$. These are expanded in powers of $\mathcal{R}$ as

$$\alpha = \alpha_1 + \alpha_2 + \cdots, \tag{II.10.14}$$

$$\psi = \psi_1 + \psi_2 + \cdots, \tag{II.10.15}$$

$$\tilde{N}_i = \tilde{N}_i^{(1)} + \tilde{N}_i^{(2)} + \cdots. \tag{II.10.16}$$

The Euler–Lagrange equations for N^i and N give

$$\nabla_j[(E_i^j - E\delta_i^j)/N] = 2H\nabla_i\alpha - 2\nabla_i\dot{\mathcal{R}} = 0, \tag{II.10.17}$$

$$R_{(3)} - 2V - \frac{1}{N^2}(E_{ij}E^{ij} - E^2) - \frac{1}{N^2}\dot{\phi}^2 = 0, \tag{II.10.18}$$

which leads to $\alpha_1 = \dot{\mathcal{R}}/H$ and $\psi_1 = -\dot{\mathcal{R}}/H + a^2\epsilon_V\theta/H$, where θ satisfies $\dot{\mathcal{R}} = \partial^2\theta$. Substituting the first-order solutions of N and N_i into the action (II.10.9) and performing integration by parts yields the second-order action for $\mathcal{R}$,

$$S_{(2)} = \frac{1}{2}\int \mathrm{d}^4x a^3 \frac{\dot{\phi}^2}{H^2}\left[\dot{\mathcal{R}}^2 - a^{-2}\left(\partial_i\mathcal{R}\right)^2\right]. \tag{II.10.19}$$

The Mukhanov-Sasaki variable are defined

$$v \equiv z\mathcal{R}, \tag{II.10.20}$$

$$z^2 \equiv a^2\frac{\dot{\phi}^2}{H^2} = 2a^2\epsilon, \tag{II.10.21}$$

and transforming to conformal time τ, we get the canonical action for the scalar mode called as the Mukhanov-Sasaki action

$$S_{(2)} = \frac{1}{2}\int \mathrm{d}\tau\mathrm{d}^3x\left[\left(v'\right)^2 + \left(\partial_i v\right)^2 + \frac{z''}{z}v^2\right], \tag{II.10.22}$$

where $'$ denotes differentiation with respect to conformal time. Note that the second term vanishes on boundary condition when it was integrated by τ because $\mathcal{R} = a^{-2}(v'z^{-1} - vz'z)^2 = a^{-2}z^{-2}\left(v'^2 - 2\frac{z'}{z}vv' + \frac{z'^2}{z^2}v^2\right) = a^{-2}z^{-2}\left(v'^2 - (\frac{z'}{z}v^2)' + \frac{z''}{z}v^2\right)$. The Fourier expansion

$$v(\tau, \mathbf{x}) = \int \frac{\mathrm{d}^3k}{(2\pi)^3}v_{\mathbf{k}}(\tau)e^{i\mathbf{k}\cdot\mathbf{x}}, \tag{II.10.23}$$

satisfies equation of motion

$$v_{\mathbf{k}}'' + \left(k^2 - \frac{z''}{z}\right) v_{\mathbf{k}} = 0, \tag{II.10.24}$$

called as the Mukhanov-Sasaki equation. Hereafter, since the variable depends only on the magnitude of $\mathbf{k}$, the vector index $\mathbf{k}$ is suppressed.

II.10.2 Boundary condition of Mukhanov-Sasaki equation

Next, we perform quantization in a same manner of the harmonic oscillator [84]. First, the field v and its momentum conjugate are promoted to operators via a plane-wave expansion,

$$v \to \hat{v} = \int \frac{\mathrm{d}\mathbf{k}^3}{(2\pi)^3} \left[v_k(\tau) \hat{a}_{\mathbf{k}} e^{i\mathbf{k}\cdot\mathbf{x}} + v_k^*(\tau) \hat{a}_{\mathbf{k}}^\dagger e^{-i\mathbf{k}\cdot\mathbf{x}} \right], \tag{II.10.25}$$

$$v_{\mathbf{k}} \to \hat{v}_{\mathbf{k}} = v_k(\tau) \hat{a}_{\mathbf{k}} + v_{-k}^*(\tau) \hat{a}_{-\mathbf{k}}^\dagger, \tag{II.10.26}$$

thus defining quantum operators. These creation and annihilation operators satisfy the canonical commutation relation

$$\langle v_k, v_k \rangle \left[\hat{a}_{\mathbf{k}}, \hat{a}_{\mathbf{k}'}^\dagger \right] = (2\pi)^3 \delta\left(\mathbf{k} - \mathbf{k}'\right). \tag{II.10.27}$$

If the mode functions are normalized as $\langle v_k, v_k \rangle \equiv \frac{i}{\hbar}\left(v_k^* v_k' - v_k^{*\prime} v_k\right) = 1$, it becomes

$$\left[\hat{a}_{\mathbf{k}}, \hat{a}_{\mathbf{k}'}^\dagger \right] = (2\pi)^3 \delta\left(\mathbf{k} - \mathbf{k}'\right). \tag{II.10.28}$$

In addition to the normalization of the mode functions, the choice of a vacuum state

$$\hat{a}_{\mathbf{k}} |0\rangle = 0, \tag{II.10.29}$$

defined such that spacetime is Minkowski deep inside the horizon, serves as the boundary condition for the Mukhanov-Sasaki equation. For example, by selecting the Minkowski vacuum of a comoving observer in the far past $\tau \to -\infty$, the mode functions are fully fixed across all scales, yielding a unique solution. Alternatively, one may choose the Bunch-Davies vacuum, defined as the Minkowski vacuum in the initial-time limit $\tau \to -\infty$ for each mode. In the hybrid inflation model treated in Chapter III, we adopt the Bunch-Davies vacuum, as will be discussed in detail later.

II.10.3 Srow-roll approximation

The general solution of the Mukhanov-Sasaki equation is generally difficult to obtain because the function z depends on the background dynamics. Therefore, for a given

inflationary background, we adopt the slow-roll approximation and solve it numerically. Using the slow-roll parameters I.5.8, the Mukhanov-Sasaki variable can be expressed as

$$z' = aHz\left(1-\epsilon+\frac{\eta}{2}+\epsilon\right) = aHz\left(1+\frac{\eta}{2}\right), \tag{II.10.30}$$

$$z'' = (aH)^2 z\left(\left(1-\epsilon+1+\frac{\eta}{2}\right)\left(1+\frac{\eta}{2}\right)+\frac{1}{2}k\eta\right) \tag{II.10.31}$$

$$= (aH)^2 z\left(2-\epsilon+\frac{3\eta}{2}-\frac{1}{2}\epsilon\eta+\frac{1}{4}\eta^2+\frac{1}{2}k\eta\right), \tag{II.10.32}$$

$$\frac{z''}{z} = (aH)^2\left(2-\epsilon+\frac{3}{2}\eta-\frac{1}{2}\epsilon\eta+\frac{1}{4}\eta^2+\frac{1}{2}\eta\xi\right), \tag{II.10.33}$$

where, under the slow-roll approximation in de Sitter space with $\epsilon \to 0$ and $H = \text{const.}$, the Mukhanov-Sasaki equation (II.10.24) reduces to

$$v_k'' + \left(k^2 - \frac{2}{\tau^2}\right) v_k = 0. \tag{II.10.34}$$

The general solution is

$$v_k = \alpha\frac{e^{-ik\tau}}{\sqrt{2k}}\left(1-\frac{i}{k\tau}\right) + \beta\frac{e^{ik\tau}}{\sqrt{2k}}\left(1+\frac{i}{k\tau}\right), \tag{II.10.35}$$

where α and β are arbitrary constants. Imposing the boundary condition of the Minkowski vacuum and the normalization $\langle v_k, v_k\rangle \equiv \frac{i}{\hbar}\left(v_k^* v_k' - v_k^{*\prime} v_k\right) = 1$, the solution is uniquely fixed as

$$v_k = \frac{e^{-ik\tau}}{\sqrt{2k}}\left(1-\frac{i}{k\tau}\right). \tag{II.10.36}$$

The ensemble average of the curvature perturbation $\hat{\psi}_{\mathbf{k}} \equiv a^{-1}\hat{v_{\mathbf{k}}}$ is then

$$\left\langle \hat{\psi}_{\mathbf{k}}(\tau)\hat{\psi}_{\mathbf{k}'}(\tau)\right\rangle = (2\pi)^3\delta\left(\mathbf{k}+\mathbf{k}'\right)\frac{|v_k(\tau)|^2}{a^2} \tag{II.10.37}$$

$$= (2\pi)^3\delta\left(\mathbf{k}+\mathbf{k}'\right)\frac{H^2}{2k^3}\left(1+k^2\tau^2\right), \tag{II.10.38}$$

so that on superhorizon scales $|k\tau| \ll 1$,

$$\left\langle \hat{\psi}_{\mathbf{k}}(\tau)\hat{\psi}_{\mathbf{k}'}(\tau)\right\rangle \to (2\pi)^3\delta\left(\mathbf{k}+\mathbf{k}'\right)\frac{H^2}{2k^3}. \tag{II.10.39}$$

Thus, the dimensionless power spectrum of curvature perturbations is

$$\mathcal{P}_\psi = \mathcal{P}_\mathcal{R} = \frac{k^3}{2\pi^2}P_\mathcal{R}(k) = \left(\frac{H}{2\pi}\right)^2, \tag{II.10.40}$$

At horizon crossing $a(t_*)H(t_*) = k$, the power spectrum of the curvature perturbation $\mathcal{R} = \frac{H}{\dot\phi}\psi$ [85, 86] is

$$\langle \mathcal{R}_{\mathbf{k}}(t)\mathcal{R}_{\mathbf{k}'}(t)\rangle = (2\pi)^3\delta\left(\mathbf{k}+\mathbf{k}'\right)\frac{H_*^2}{2k^3}\frac{H_*^2}{\dot\phi_*^2} = (2\pi)^3\delta\left(\mathbf{k}+\mathbf{k}'\right)P_{\mathcal{R}}(k), \tag{II.10.41}$$

where the subscript $*$ denotes evaluation at horizon crossing $k = a(t_*)H(t_*)$, and the dimensionless power spectrum is defined as

$$\mathcal{P}_{\mathcal{R}}(k) \equiv \frac{k^3}{2\pi^2}P_{\mathcal{R}}(k). \tag{II.10.42}$$

II.11 Flat gauge

Up to this, we have calculated the scalar power spectrum in the comoving gauge $\delta\phi = 0$. In this section, we will perform the calculation using the flat gauge $\Psi = 0$.

II.11.1 Flat gauge and scalar power spectrum

At this stage, the curvature perturbation $\mathcal{R}$ is

$$\mathcal{R} = H\frac{\delta\phi}{\dot\phi} \equiv -H\delta t, \tag{II.11.1}$$

so that the power spectrum of $\mathcal{R}$ becomes

$$\langle \mathcal{R}_{\mathbf{k}}\mathcal{R}_{\mathbf{k}'}\rangle = \left(\frac{H}{\dot\phi}\right)^2\langle \delta\phi_{\mathbf{k}}\delta\phi_{\mathbf{k}'}\rangle\,. \tag{II.11.2}$$

In the same way of the comoving gauge and using the slow-roll approximation, we have

$$\langle \delta\phi_{\mathbf{k}}\delta\phi_{\mathbf{k}'}\rangle = (2\pi)^3\delta\left(\mathbf{k}+\mathbf{k}'\right)\frac{2\pi^2}{k^3}\left(\frac{H}{2\pi}\right)^2, \quad \mathcal{P}_{\delta\phi} = \left(\frac{H}{2\pi}\right)^2. \tag{II.11.3}$$

Therefore, the dimensionless power spectrum of curvature perturbations generated by quantum fluctuations during inflation is

$$\mathcal{P}_{\mathcal{R}}(k) = \frac{H_*^2}{(2\pi)^2}\frac{H_*^2}{\dot\phi_*^2}. \tag{II.11.4}$$

From Eqs. (I.5.11) and (I.5.12), we have

$$\begin{aligned} 0 &= 3H\dot\phi + \frac{\mathrm{d}V(\phi)}{\mathrm{d}\phi} = 3H\dot\phi + 3\times 2H\dot H/\dot\phi, \\ \dot\phi^2 &= -2H\dot H, \end{aligned} \tag{II.11.5}$$

so that rewriting ϕ in terms of the slow-roll parameter $\epsilon \equiv -\dot{H}/H^2$, the dimensionless power spectrum of scalar perturbation becomes

$$\mathcal{P}_{\rm s}(k) \equiv \mathcal{P}_{\mathcal{R}}(k) = \frac{1}{8\pi^2}\frac{H_*^2}{m_{\rm pl}^2}\frac{1}{\epsilon_*}, \tag{II.11.6}$$

which is the well-known result.

II.11.2 Flat gauge and tensor power spectrum

Similarly to the scalar perturbations, we consider tensor perturbations. First, the second-order action for tensor perturbations is

$$S_{(2)} = \frac{m_{\rm pl}^2}{8}\int {\rm d}\tau {\rm d}x^3 a^2 \left[(h'_{ij})^2 - (\partial_l h_{ij})^2\right]. \tag{II.11.7}$$

Fourier-expanding of the tensor perturbation yields

$$h_{ij}(\eta,\mathbf{x}) = \int \frac{{\rm d}^3k}{(2\pi)^3}\sum_{s=+,\times}\epsilon_{ij}^s(k)h_{\mathbf{k}}^s(\tau)e^{i\mathbf{k}\cdot\mathbf{x}} \tag{II.11.8}$$

$$= \int \frac{{\rm d}^3k}{(2\pi)^{3/2}}\left(e_{ij}^+(\mathbf{k})h_{\mathbf{k}}^+(\eta) + e_{ij}^\times(\mathbf{k})h_{\mathbf{k}}^\times(\eta)\right)e^{i\mathbf{k}\cdot\mathbf{x}}, \tag{II.11.9}$$

where ϵ are transverse $\epsilon_{ii}=0$, traceless, and normalized as $\epsilon_{ij}^s(k)\epsilon_{ij}^{s'}(k) = 2\delta_{ss'}$. For the basis, let $e_i(\mathbf{k})$ and $\bar{e}_i(\mathbf{k})$ form an orthonormal basis orthogonal to the wave vector $\mathbf{k}$, then

$$e_{ij}^+(\mathbf{k}) = \frac{1}{\sqrt{2}}\left(e_i(\mathbf{k})e_j(\mathbf{k}) - \bar{e}_i(\mathbf{k})\bar{e}_j(\mathbf{k})\right), \tag{II.11.10}$$

$$e_{ij}^\times(\mathbf{k}) = \frac{1}{\sqrt{2}}\left(e_i(\mathbf{k})\bar{e}_j(\mathbf{k}) + \bar{e}_i(\mathbf{k})e_j(\mathbf{k})\right), \tag{II.11.11}$$

where the $+$ mode corresponds to the E-mode and the $\times$ mode to the B-mode of gravitational waves. Using this, the action becomes

$$S_{(2)} = \sum_s \int {\rm d}\tau {\rm d}\mathbf{k}\frac{a^2 m_{\rm pl}^2}{4}\left[h_{\mathbf{k}}^{s'}h_{\mathbf{k}}^{s'} - k^2 h_{\mathbf{k}}^s h_{\mathbf{k}}^s\right]. \tag{II.11.12}$$

Defining the canonically normalized field as

$$v_{\mathbf{k}}^s \equiv \frac{a}{2}m_{\rm pl}h_{\mathbf{k}}^s, \tag{II.11.13}$$

the action can be rewritten as

$$S_{(2)} = \sum_s \int {\rm d}\tau {\rm d}^3\mathbf{k}\frac{1}{2}\left[(v_{\mathbf{k}}^{s'})^2 - \left(k^2 - \frac{a''}{a}\right)(v_{\mathbf{k}}^s)^2\right]. \tag{II.11.14}$$

Considering the normalized massless field for each polarization s in de Sitter space,

$$h^s_{\mathbf{k}} = \frac{2}{m_{\rm pl}}\psi^s_{\mathbf{k}}, \tag{II.11.15}$$

where $\psi^s_{\mathbf{k}} \equiv v_{\mathbf{k}}/a$, the power spectrum of ψ is

$$\mathcal{P}_\psi \equiv \left(\frac{H}{2\pi}\right)^2. \tag{II.11.16}$$

Thus, the power spectrum of tensor polarization with s polarization is

$$\mathcal{P}_h(k) \equiv \frac{4}{m^2_{\rm pl}}\left(\frac{H_*}{2\pi}\right)^2, \tag{II.11.17}$$

and, the total power spectrum of tensor perturbation becomes the summation of each mode $2\mathcal{P}_h(k)$

$$\mathcal{P}_{\rm t}(k) \equiv 2\mathcal{P}_h(k) = \frac{8}{m^2_{\rm pl}}\left(\frac{H_*}{2\pi}\right)^2. \tag{II.11.18}$$

Similarly to the scalar case, from Eq. (I.5.12) where $V = H^2/3m^2_{\rm pl}$, we have

$$\mathcal{P}_{\rm t}(k) = \frac{2V}{3\pi^2 m^4_{\rm pl}}. \tag{II.11.19}$$

II.12 Scale dependence

At this stage, the spectral indices for scalar and tensor perturbations are defined as

$$n_{\rm s} - 1 \equiv \frac{{\rm d}\ln\mathcal{P}_{\rm s}}{{\rm d}\ln k}, \quad n_{\rm t} \equiv \frac{{\rm d}\ln\mathcal{P}_{\rm t}}{{\rm d}\ln k}. \tag{II.12.1}$$

Here, $\ln k = N + \ln H$. Evaluating these to first order in the slow-roll parameters gives

$$n_{\rm s} - 1 = \frac{{\rm d}\ln\mathcal{P}_{\rm s}}{{\rm d}N}\frac{{\rm d}N}{{\rm d}\ln k} = \left(2\frac{{\rm d}\ln H}{{\rm d}N} - \frac{{\rm d}\ln\epsilon}{{\rm d}N}\right)\frac{{\rm d}N}{{\rm d}\ln k}, \tag{II.12.2}$$

$$n_{\rm t} = \frac{{\rm d}\ln\mathcal{P}_{\rm t}}{{\rm d}N}\frac{{\rm d}N}{{\rm d}\ln k} = 2\frac{{\rm d}\ln H}{{\rm d}N}\frac{{\rm d}N}{{\rm d}\ln k}, \tag{II.12.3}$$

where the derivatives of the slow-roll parameters are

$$\frac{{\rm d}\ln H}{{\rm d}N} = -\epsilon \simeq -\epsilon_V, \tag{II.12.4}$$

$$\frac{{\rm d}\ln\epsilon_V}{{\rm d}N} \simeq 4\epsilon_V - 2\eta_V, \tag{II.12.5}$$

$$\frac{{\rm d}\eta_V}{{\rm d}N} \simeq 2\epsilon_V\eta_V - \xi^2_V, \tag{II.12.6}$$

$$\frac{\mathrm{d}\xi_V^2}{\mathrm{d}N} \simeq 4\epsilon_V\xi_V^2 - \eta_V\xi_V^2 - \omega_V^3, \tag{II.12.7}$$

where, using Eq. (I.5.13) and evaluating at horizon crossing $k = aH$, $\mathrm{d}N/\mathrm{d}\ln k = 1/(1-\epsilon)$, we obtain

$$n_\mathrm{s} - 1 = \frac{2\eta - 4\epsilon}{1-\epsilon} \simeq 2\eta_{V*} - 6\epsilon_{V*}, \tag{II.12.8}$$

$$n_\mathrm{t} = \frac{-2\epsilon}{1-\epsilon} \simeq -2\epsilon_{V*}, \tag{II.12.9}$$

expressed in terms of the potential slow-roll parameters. The running of the spectral index is then

$$\alpha_\mathrm{s} \equiv \frac{\mathrm{d}n_\mathrm{s}}{\mathrm{d}\ln k} \simeq 16\epsilon_{V*}\eta_{V*} - 24\epsilon_{V*}^2 - 2\xi_{V*}^2\,, \tag{II.12.10}$$

$$\beta_\mathrm{s} \equiv \frac{\mathrm{d}^2 n_\mathrm{s}}{\mathrm{d}\ln k^2} \simeq -192\epsilon_{V*}^3 + 192\epsilon_{V*}^2\eta_{V*} - 32\epsilon_{V*}\eta_{V*}^2 - 24\epsilon_{V*}\xi_{V*}^2 + 2\eta_{V*}\xi_{V*}^2 + 2\omega_{V*}^3\,, \tag{II.12.11}$$

as shown in [87]. Furthermore, the tensor-to-scalar ratio is defined as

$$r \equiv \frac{\mathcal{P}_\mathrm{t}}{\mathcal{P}_\mathrm{s}} = \frac{\frac{8}{m_\mathrm{pl}^2}\left(\frac{H_*}{2\pi}\right)^2}{\frac{1}{8\pi^2}\frac{H_*^2}{m_\mathrm{pl}^2}\frac{1}{\epsilon_*}} = 16\epsilon_*. \tag{II.12.12}$$

Hence, the spectral index and tensor-to-scalar ratio are related by

$$r = -8n_\mathrm{t}, \tag{II.12.13}$$

which is often referred to as the consistency relation. Moreover, using the Friedmann equation $m_\mathrm{pl}^2 H^2 = \rho/3 \sim V/3m_\mathrm{pl}^2$, r is also related to the energy scale of inflation,

$$r \equiv \frac{\mathcal{P}_\mathrm{t}}{\mathcal{P}_\mathrm{s}} \approx \frac{2H^2/\pi^2 m_\mathrm{pl}^2}{(4.7\times10^{-5})^2} \simeq \frac{2V/3\pi^2 m_\mathrm{pl}^4}{(4.7\times10^{-5})^2} \approx 0.01 \times \left(\frac{V^{1/4}}{5.2\times10^{16}\mathrm{GeV}}\right)^4. \tag{II.12.14}$$

Thus, when the tensor-to-scalar ratio r is of order 0.01, the energy scale of inflation corresponds roughly to the GUT scale.

In the next chapter, we extend the inflationary models discussed so far to multi-field scenarios, and examine in detail the physical quantities arising from hybrid inflation models with a trapping phase.

Chapter III

Multi-field trapped inflation with resonant processes

We study a multi-field model of inflation. The basic setup is reminiscent of the hybrid inflation scenario [26, 27] with some essential modifications. First, we consider the potential in the direction of the inflaton ϕ to be completely flat at tree level. The slope is generated by radiative corrections. Such single filed models are known by the name "Running-Mass-Inflation"(RMI) [88–90]. At one loop level, the shape of the potential is given by

$$V(\phi) = V_{\rm c}\left[1+U(\phi)\right], \tag{III.0.1}$$

where $V_{\rm c}$ is constant and $U(\phi)$ is defined by

$$U(\phi) \equiv -\frac{1}{2}\frac{\phi^2}{m_{\rm pl}^2}\left(B-\frac{A}{\left(1+\alpha\ln\frac{\phi}{m_{\rm pl}}\right)^2}\right), \tag{III.0.2}$$

The shape of $U(\phi)$ for several values of α, A and B parameters is shown in Fig. III.1.

In analogy to hybrid inflation scenario we add an additional field χ. The potential in the χ direction is of the hilltop type [61]. The simplest form of such a potential can be written as

$$V(\chi) = -\frac{1}{2}m^2\chi^2+\lambda\chi^4. \tag{III.0.3}$$

The crucial piece for this scenario is the interaction part of the Lagrangian, which we take to be [23, 24]

$$V_{\rm int}(\phi,\chi) = \frac{1}{2}g^2\chi^2\left(\phi-\phi_{\rm SBP}\right)^2. \tag{III.0.4}$$

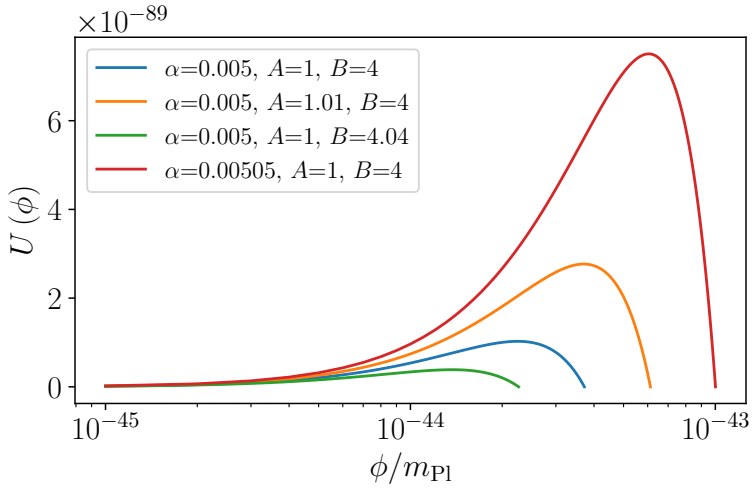

Fig. III.1 Rescaled RMI potential $U(\phi)$ in Eq. (III.0.2) for several α, A and B values.

$\phi_{\rm SBP}$ denotes the critical value at which $V_{\rm int}$ vanishes. We choose to call this point a "Symmetry Breaking Point" and denote it by $\phi_{\rm SBP}$ in order to make the relation to the mechanism discussed in Ref. [24] more suggestive, but also to emphasise that our scenario somewhat deviates from the standard hybrid inflation scenario.

The main role of the χ field in hybrid inflation scenarios is to terminate inflation. It is called the waterfall field. In our scenario the main function of χ is to trap ϕ at the $\phi_{\rm SBP}$ value. This is achieved by the backreaction of resonantly produced χ particles [13, 24], hence we also sometimes call χ as the "trapping field". Another difference, as compared to the traditional hybrid scenario, is that the "waterfall" phase in this scenario lasts many e-foldings. This is needed to extend inflation sufficiently long after $\phi = \phi_{\rm SBP}$ is reached, so that the horizon and flatness problems of Hot Big Bang are solved. Finally, as can be witnessed from Eq. (III.0.4), the ϕ–χ interaction includes a trilinear term. Trilinear interactions can be found in the A term of SUGRA models [91], but it can also be generated by fermion condensation [92].

Adding all these components together, the full Lagrangian of the model can be written as

$$\mathcal{L} \;=\; -\frac{1}{2}\left(\partial_\mu\phi\right)^2 - V\left(\phi\right) - \frac{1}{2}\left(\partial_\mu\chi\right)^2 - V\left(\chi\right) - V_{\rm int}\left(\phi,\chi\right)\,. \qquad \text{(III.0.5)}$$

The dynamics evolves over three stages. Initially the inflaton ϕ is displaced far away from the critical value, $\phi \gg \phi_{\rm SBP}$. This makes the trapping field χ very heavy and anchored at the origin. During the first phase, while ϕ rolls down towards the origin, the dynamics can be well approximated by slow-roll. Once ϕ approaches $\phi_{\rm SBP}$ the second phase starts. The motion of ϕ induces a non-adiabatic change in the effective mass of the trapping field via the interaction term in Eq. (III.0.4). This results in resonant excitations of χ, which

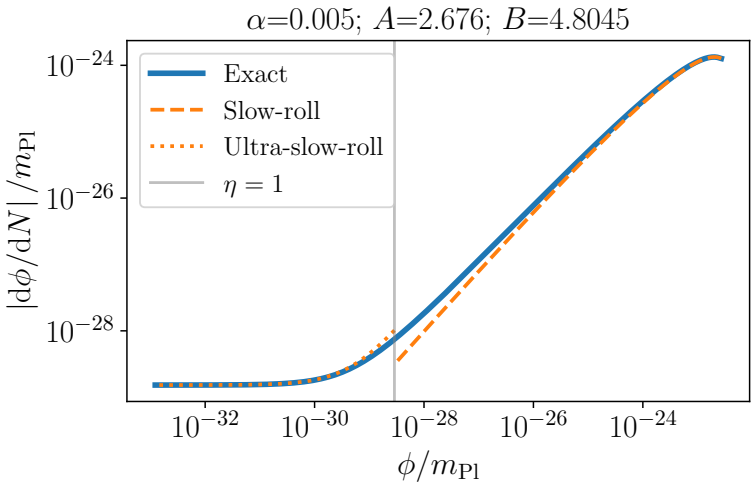

Fig. III.2 Numerical solution of homogeneous RMI equations ("Exact"). At the pivot scale, on the RHS of the plot, inflation is well approximated by slow-roll (cf. Eq. (III.1.1)), but eventually it enters the ultra-slow-roll regime (cf. Eq. (III.1.4)). Conventionally this transition is taken at $\eta = 1$ (vertical gray line).

backreact onto the motion of ϕ and anchors it at $\phi_{\rm SBP}$. In the final phase, the χ field rolls down the potential in Eq. (III.0.3), which is chosen to be sufficiently flat, so that inflation lasts for an additional ~ 10 e-foldings in this phase. Bellow we discuss these phases in more detail.

III.1 Running-Mass-Inflation

Let ϕ_* be the inflaton field value when the pivot scale exits the horizon during inflation. CMB observations allow us to constrain the primordial spectrum roughly 10 e-foldings around this value. The first task is to find regions in (α, A, B) parameter space where the model generates the primordial perturbation that is consistent with CMB observations.

Generically we take $\phi_{\rm SBP} \ll \phi_*$, which, according to Eq. (III.0.4), makes the χ field heavy and anchored at the origin, leading to an effectively single field inflation, at least within the 10 e-foldings mentioned above. Another important consequence of χ being heavy is that the isocurvature perturbation is suppressed at CMB scales, which makes the observational bounds on this parameter [93] easily satisfied.

One of the features of the RMI potential in Eq. (III.0.1) is that it becomes ever flatter as ϕ field approaches the origin. This makes the inflaton dynamics eventually dominated by the kinetic energy rather than by the slope of the potential. In other words, inflation enters the ultra-slow-roll regime [94–97] if not terminated earlier. To investigate this issue we solved the homogeneous equations of motion numerically. One such solution is shown in Fig. III.2.

As can be seen from Fig. III.2, at larger inflaton values slow-roll provides a good description of the dynamics. During this period the inflaton equation of motion can be approximated by Eq. (I.5.11)

$$\dot{\phi} \simeq -\frac{V_{,\phi}}{3H}\,, \tag{III.1.1}$$

where V is given in Eq. (III.0.1) and the index denotes the derivative with respect to the field ϕ. In this approximation the Hubble parameter is dominated by the potential energy

$$3m_{\rm pl}^2 H^2 \simeq V(\phi) \simeq V_{\rm c}\,, \tag{III.1.2}$$

where $V_{\rm c}$ is defined in Eq. (III.0.1). This slow-roll approximated solution is denoted by the dashed curve in Fig. III.2.

As ϕ decreases, eventually inflation enters the ultra-slow-roll regime. In this regime the slope of the potential can be neglected, and we obtain an approximate equation of motion of the form

$$\ddot{\phi} \simeq -3H\dot{\phi}\,, \tag{III.1.3}$$

where $H \simeq$ const. and its value can be computed using the same approximate expression in Eq. (III.1.2). It is easy to show that the approximate solution of the above equation is

$$\dot{\phi} \simeq \dot{\phi}_0 - 3H(\phi - \phi_0)\,. \tag{III.1.4}$$

The ultra-slow-roll approximated solution is represented by the dotted curve in Fig. III.2.

The approximate location in the potential, where slow-roll gives way to ultra-slow-roll, is conventionally taken to be $\eta = 1$, where η is the second slow-roll parameter defined bellow in Eq. (III.1.6).

To choose viable models, which do not contradict CMB constraints, we calculate the properties of the scalar perturbation spectrum and the amplitude of the tensor mode. Because slow-roll approximates the inflaton dynamics sufficiently well when CMB scales exit the horizon, we use the well known relations between the slow-roll parameters and the shape of the primordial spectrum. These parameters are defined in terms of the potential $V(\phi)$ and its derivatives as

$$\epsilon = \frac{m_{\rm pl}^2}{2}\left(\frac{U_{,\phi}}{U+1}\right)^2\,, \tag{III.1.5}$$

$$\eta = m_{\rm pl}^2\frac{U_{,\phi\phi}}{U+1}\,, \tag{III.1.6}$$

$$\xi^2 = m_{\rm pl}^4 \frac{U_{,\phi} U_{,\phi\phi\phi}}{(U+1)^2}\,, \tag{III.1.7}$$

$$\omega^3 = m_{\rm pl}^6 \frac{U_{,\phi}^2 U_{,\phi\phi\phi\phi}}{(U+1)^3}\,, \tag{III.1.8}$$

where $U(\phi)$ is given in Eq. (III.0.2) and the indices denote derivatives with respect to the inflaton ϕ. The spectral properties of the primordial scalar perturbation are related to the above parameters by the following expressions (see e.g. Ref. [61] or [98])

$$n_{\rm s} \equiv \frac{{\rm d}\ln A_{\rm s}}{{\rm d}\ln k} \simeq 1 - 6\epsilon + 2\eta\,, \tag{III.1.9}$$

$$\alpha_{\rm s} \equiv \frac{{\rm d}n_{\rm s}}{{\rm d}\ln k} \simeq 16\epsilon\eta - 24\epsilon^2 - 2\xi^2\,, \tag{III.1.10}$$

$$\beta_{\rm s} \equiv \frac{{\rm d}^2 n_{\rm s}}{{\rm d}\ln k^2} \simeq -192\epsilon^3 + 192\epsilon^2\eta - 32\epsilon\eta^2 - 24\epsilon\xi^2 + 2\eta\xi^2 + 2\omega^3\,, \tag{III.1.11}$$

where $n_{\rm s}$, $\alpha_{\rm s}$ and $\beta_{\rm s}$ are the scalar spectral index, its running and the running-of-the-running respectively. All of these quantities are to be computed when the pivot scale exits the horizon. Analogously, tensor-to-scalar ratio can also be related to the slow-roll parameter ϵ by

$$r = 16\epsilon\,. \tag{III.1.12}$$

To find models that are compatible with observations we scan over the parameters α, A and B and look for regions of ϕ_* values that result in the primordial spectrum with values in the range

$$n_s = 0.9743 \pm 0.0034\,, \tag{III.1.13}$$

$$\alpha_s = 0.0062 \pm 0.0052\,, \tag{III.1.14}$$

$$\beta_s = 0.010 \pm 0.013\,. \tag{III.1.15}$$

The errorbars correspond to 1σ constraints for n_s [99], α_s [100] and β_s [93]. To constrain the tensor-to-scalar ratio we adopt the upper bound in BICEP/*Keck* + WMAP/*Planck* data [7]

$$r < 0.036 \quad (95\,\%\,\text{C.L.})\,. \tag{III.1.16}$$

The final PBH abundance is not very sensitive to the precise values of these parameters. They only determine which model in the (α, A, B) plane will be used to represent the inflaton direction. The result of the scan over this parameter space is shown in Fig. III.3 for several values of α.

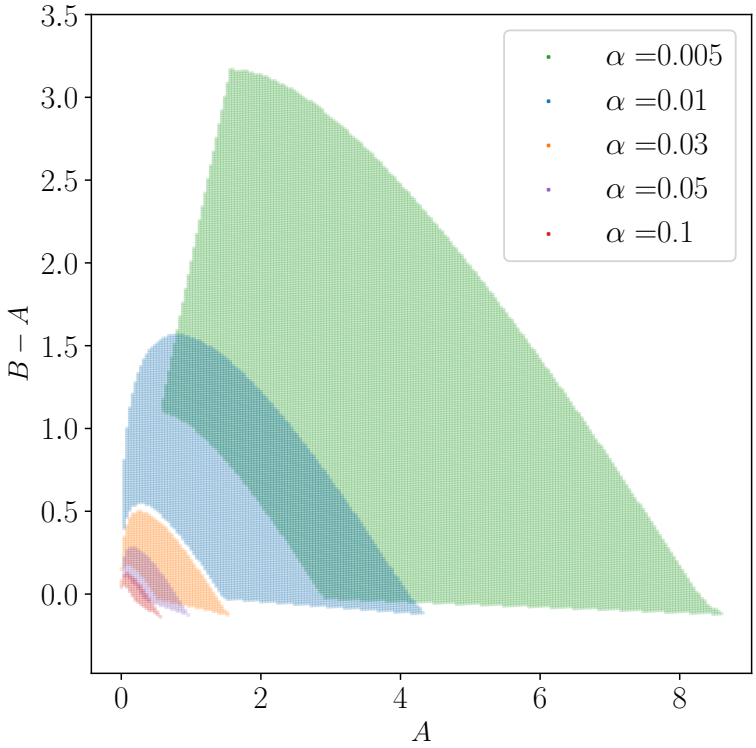

Fig. III.3 Parameter regions for several different α values where the running mass inflation models are compatible with the CMB constraints on the primordial spectrum at the pivot scale $k_* = 0.05\,\mathrm{Mpc}^{-1}$ (Eqs. (III.1.13)–(III.1.16)). We also impose two other conditions: $\phi_* < m_{\mathrm{pl}}$ when the pivot scale exits the horizon and that the energy scale of inflation is larger than the BBN scale.

Usually all the constraints in Eqs. (III.1.13)–(III.1.16) can be satisfied only for a small range of ϕ values, if at all. For such models we choose ϕ_* to correspond to the value that is closest to the central value of the constraints. Once ϕ_* is fixed, we can compute the energy scale of inflation V_c from the amplitude of the scalar spectral index A_s, given by

$$A_s = \frac{V}{24 m_{pl}^2 \epsilon} . \tag{III.1.17}$$

The value of A_s is fixed by the Planck normalisation, $A_s = 3.044$ [93]. Initially ϕ follows the slow-roll equation of motion in Eq. (III.1.1). As the potential flattens out the dynamics becomes well approximated by ultra-slow-roll in Eq. (III.1.4). The latter equation is solved by

$$\dot{\phi} \propto a^{-3} . \tag{III.1.18}$$

One of the consequences of the flattening of the potential is the rapid increase in the amplitude of the curvature perturbation $\mathcal{P}_\zeta$. On superhorizon scales it can be written as

$$\mathcal{P}_\zeta (k) = \left(\frac{H}{\dot{\phi}} \right)^2 |\delta\phi_k|^2 , \tag{III.1.19}$$

where $\delta\phi_k (t)$ is the Fourier mode of the field perturbation $\delta\phi (x, t)$. We can see that as $\dot{\phi}$ decreases, $\mathcal{P}_\zeta$ rapidly grows. We must make sure that the first phase of inflation is terminated before $\mathcal{P}_\zeta$ reaches the value of 1. Otherwise perturbations become non-linear, which is in conflict with observations [101, 102].

III.2 The Trapping Phase

To the best of our knowledge, there is no detailed discussion in the literature of a mechanism to end the RMI phase and provide the remaining e-foldings of inflation. Usually, it is implicitly assumed that hybrid inflation or some related mechanism terminates the RMI stage before $\mathcal{P}_\zeta (k)$ becomes too large. Unfortunately, a simplistic implementation of hybrid inflation is difficult to realise. After observable scales – where $\mathcal{P}_\zeta (k_*)$ is fixed to satisfy CMB bounds – exit the horizon, the maximum value of $\mathcal{P}_\zeta (k)$ must be reached in about 30-35 e-foldings. Only then, the masses of PBHs created by a large curvature perturbation, which reached approximately $10^{-1.5}$, are such that they can explain the observed DM abundance (see Fig. IV.3). But 30-35 fall short from the expected 50-60 e-foldings of inflation, which are required to solve the flatness and horizon problems of Hot Big Bang (see section III.3 for a more detailed discussion). Therefore, to solve these

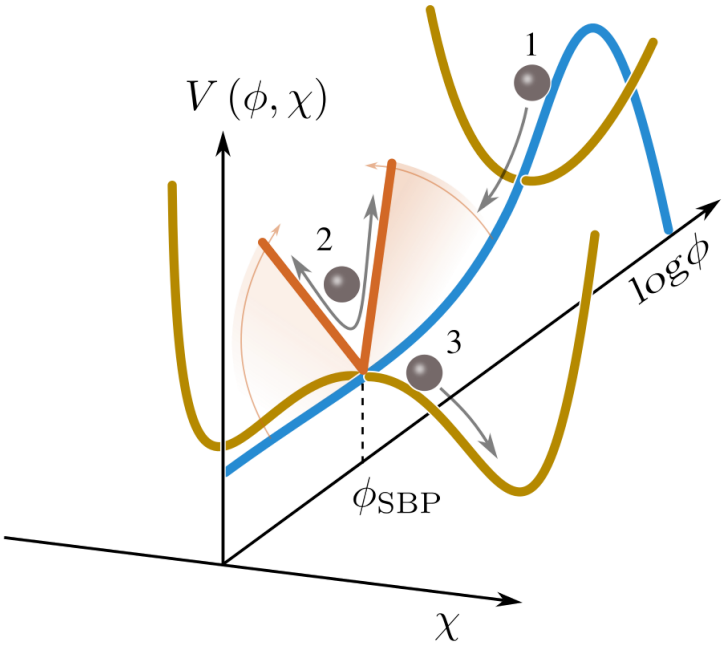

Fig. III.4 Schematic depiction of our scenario. At stage 1 the field rolls down along the RMI direction (blue curve). At tree level, the linear potential (red curve) does not exist. Once the field reaches SBP (stage 2) it resonantly excites the χ field. Excitations backreact onto the motion of the field, which can be effectively described by a steepening linear potential. At this stage the trapped ϕ field oscillates around $\phi_{\rm SBP}$ with an exponentially decreasing amplitude. Eventually the amplitude becomes too small to excite the χ field. At that point the evolution enters the 3rd stage, in which the field rolls down solely in the direction of the sufficiently flat waterfall potential (brown curve) with ϕ remaining being fixed at $\phi_{\rm SBP}$. During stage 2 the metric perturbation is also resonantly amplified for scales which exit the horizon at that time.

problems inflation must last for an additional ~ 10 e-foldings in the waterfall phase. A long waterfall phase can be achieved if the potential in this direction is flat enough. But we found that for a too flat potential the ϕ field just zips through the critical (Symmetry Breaking) point without destabilising the waterfall field χ.

Fortunately, as we show, this problem can be circumvented by another effect. For some parameter values the passage of ϕ through the Symmetry Breaking Point $\phi_{\rm SBP}$ induces resonant excitations of the χ field. This field backreacts onto the motion of ϕ by making it effectively heavy and stopping it from rolling down the potential. This is the basic scenario of the tachyonic trap mechanism discussed in Refs. [23, 24]. In this work we make use of the tachyonic trap mechanism to terminate RMI at the value of $\mathcal{P}_\zeta$ that results in the production of PBHs with masses that can explain Dark Matter [35]. A schematic depiction of our scenario is provided in Fig. III.4.

III.2.1 The Tachyonic Trap

In Refs. [23, 24], where the tachyonic trapping mechanism is analysed, the metric perturbations are ignored. These simplifications can no longer be employed for the current model, where such perturbations play the central role. Nevertheless, before discussing the model in full detail, including the metric perturbation, bellow we summarize the basic ideas behind the tachyonic trap mechanism.

For the most part of the RMI stage of inflation the trapping field χ is very heavy. This is the case if the value of the coupling constant g in Eq. (III.0.4) is not too small, so that $g^2\left(\phi-\phi_{\rm SBP}\right)^2 \gg H^2$, where H is the Hubble parameter during inflation. This makes the homogeneous component of the χ field anchored at the origin. The perturbations $\delta\chi$ of the χ field obey the following equation of motion:

$$\delta\ddot{\chi}_k + 3H\delta\dot{\chi}_k + \left(\omega_k^2 + 12\lambda\left\langle\chi^2\right\rangle\right)\delta\chi_k \simeq 0\,, \tag{III.2.1}$$

where

$$\omega_k^2 \equiv \frac{k^2}{a^2} - m^2 + g^2\left(\phi-\phi_{\rm SBP}\right)^2\,. \tag{III.2.2}$$

We can rewrite the above equation in the canonical form by defining

$$X_k \equiv a\chi_k\,, \tag{III.2.3}$$

and using the conformal time $\mathrm{d}\tau \equiv \mathrm{d}t/a$. This gives

$$X_k'' + \left(W_k^2 + 12\lambda a^2\left\langle\chi^2\right\rangle\right)X_k = 0\,, \tag{III.2.4}$$

where primes denote derivatives with respect to τ and

$$W_k^2 \equiv a^2\omega_k^2 - \frac{a''}{a}\,. \tag{III.2.5}$$

Initially, as field ϕ is far away from SBP, the effective mass of the trapping field satisfies

$$m_{\rm eff}^2 \equiv g^2\left(\phi-\phi_{\rm SBP}\right)^2 - m^2 \simeq g^2\left(\phi-\phi_{\rm SBP}\right)^2 \gg 12\lambda\left\langle\chi^2\right\rangle\,, \tag{III.2.6}$$

and Eq. (III.2.4) reduces to the equation of a harmonic oscillator with an adiabatically changing mass. We can thus impose the adiabatic vacuum initial conditions, which, at the lowest order, are given by

$$X_{k,\rm vac}\left(\eta\right) = \frac{1}{\sqrt{2W_k}}\mathrm{e}^{-\mathrm{i}\int W_k\mathrm{d}\eta}\,. \tag{III.2.7}$$

Up to the same order, the occupation number can be computed using the expression

$$n_k = \frac{W_k}{2}\left[\frac{|X_k'|^2}{W_k^2} + |X_k|^2\right] - \frac{1}{2}\,. \tag{III.2.8}$$

The $12\lambda a^2 \langle\chi^2\rangle$ term consists of the Hartree approximation to account for self-interactions, where the expectation value $\langle\chi^2\rangle$ can be computed using the equation

$$\left\langle\chi^2\right\rangle = a^{-2}\left\langle X^2\right\rangle = \frac{a^{-2}}{2\pi^2}\int \mathrm{d}k\, k^2\left[|X_k|^2 - \frac{1}{2\,|W_k|}\right]\,. \tag{III.2.9}$$

As the ϕ field moves towards the origin and comes close to $\phi_{\rm SBP}$ the effective mass squared $m_{\rm eff}^2$ vanishes and then becomes negative. Moreover, within some interval of ϕ values the change of $m_{\rm eff}^2$ is rendered to be non-adiabatic [23, 24]. This causes two effects. First, the non-adiabaticity of $m_{\rm eff}^2$ results in the resonant excitations of the χ field, as described in Ref. [103]. Second, as $m_{\rm eff}^2$ becomes negative, it can lead to an additional amplification of χ field perturbations via the process known as the tachyonic resonance [104, 22].

Which of the two effects dominates, depends on model parameters [24]. But in both cases, due to ϕ–χ interactions, the exponential growth of $\langle\chi^2\rangle$ backreacts onto the motion of the ϕ field by creating an effective contribution to its mass term. Indeed, from Eq. (III.0.4) we find the effective equation of motion of the homogeneous component of the ϕ field to be

$$\ddot{\phi} + 3H\dot{\phi} + V\left(\phi,\chi\right)_{,\phi} = 0\,, \tag{III.2.10}$$

where

$$V\left(\phi,\chi\right)_{,\phi} \simeq V_{\rm c}U_{,\phi} + g^2\left\langle\chi^2\right\rangle\left(\phi - \phi_{\rm SBP}\right)\,, \tag{III.2.11}$$

and $V_{\rm c}$ and U are defined in Eqs. (III.0.1) and (III.0.2) respectively. Once the second term in the above expression becomes large enough, $g^2\langle\chi^2\rangle > H^2$, the field becomes heavy and stops running towards the origin, but rather oscillates around $\phi_{\rm SBP}$ with a decaying amplitude.

This process is somewhat similar to the one described in Ref. [13], where the resonant excitations of the χ field traps the ϕ field at SBP. In contrast to that work, we take χ to be tachyonic. This way the trapping of ϕ at $\phi_{\rm SBP}$ initiates the symmetry breaking phase by releasing the χ field from the origin and allowing it to roll towards the vacuum value. This gives the name for the subscript $\phi_{\rm SBP}$, as in "Symmetry Breaking Point" and the name "tachyonic trap" for the mechanism [24].

There is another crucial difference in the current model as compared to both Ref. [13] and [24]. The resonance and the trapping in the latter references are assumed to happen in a non-accelerating spacetime. In the current application, we make use of the tachyonic trap during inflation. The idea of resonant field excitations during inflation is not new. We can find such discussions in, for example, Refs. [15, 105, 20, 106] and many others. But here again, in contrast to those works, we consider χ to be tachyonic. This allows for the χ field to play the role of the waterfall field of the hybrid inflation.

III.2.2 The Metric Perturbation

As it is well known in the literature of preheating, see e.g. Refs. [107–110, 15, 20], resonant processes also affect the metric perturbation. The current model is not an exception. In order to estimate these effects and to compute the final spectrum of the primordial curvature perturbation we employ semi-analytic computations. To that goal several simplifications are made. First of all, we will only solve linearised equations. It is likely that such an approximation provide sufficiently accurate results. In contrast to the preheating scenarios, perturbations during inflation must remain linear. This also justifies using the Hartree approximation to estimate the effects of non-linear terms. Due to the smallness of perturbations, we would expect non-linear k-mode interactions of the metric perturbation to not change the picture significantly.

At the linear level, we perform the computations in the Newtonian and flat gauges. The two gauges are used in order to check the consistency of our numerical code. We present Newtonian gauge equations in this section and analogous expressions in the flat gauge in Appendix A.1. The line element in the former takes the form

$$\mathrm{d}s^2 = -(1+2\Phi)\,\mathrm{d}t^2 + a^2(t)\,(1+2\Psi)\,\delta_{ij}\mathrm{d}x^i\mathrm{d}x^j\,. \tag{III.2.12}$$

Since this is a two scalar field model in General Relativity, the anisotropic stress vanishes and the two metric perturbation variables are related by $\Psi = -\Phi$. Therefore we can drop Ψ in favour of Φ.

Scalar fields ϕ and χ are also perturbed such that

$$\phi(\boldsymbol{x},t) = \bar{\phi}(t) + \delta\phi(\boldsymbol{x},t)\,, \tag{III.2.13}$$

and

$$\chi(\boldsymbol{x},t) = \bar{\chi}(t) + \delta\chi(\boldsymbol{x},t)\,. \tag{III.2.14}$$

In the case of the ϕ field we have $\bar{\phi} \gg \delta\phi$, therefore the separation into the homogeneous value $\bar{\phi}$ and the perturbation $\delta\phi$ is unambiguous. In regards to the χ field, an analogous

separation is more subtle. Initially χ is heavy and its VEV vanishes. Hence, we define $\bar{\chi}$ by

$$\bar{\chi} \equiv \sqrt{\langle \chi^2 \rangle}\,, \tag{III.2.15}$$

where $\langle \chi^2 \rangle$ is given in Eq. (III.2.9) and we take $\delta\chi$ to be of the same perturbation order as $\delta\phi$. Finally, because we have no use of the full fields $\phi(\boldsymbol{x}, t)$ and $\chi(\boldsymbol{x}, t)$, we will drop the overbars from the homogeneous fields and denote them just by ϕ and χ in the remaining part of the text.

The homogeneous components follow the equations

$$\ddot{\phi} + 3H\dot{\phi} + V_{,\phi} = 0\,, \tag{III.2.16}$$

$$\ddot{\chi} + 3H\dot{\chi} + V_{,\chi} = 0\,, \tag{III.2.17}$$

where the Hubble parameter is given by

$$3H^2 = \frac{1}{2}\dot{\phi}^2 + \frac{1}{2}\dot{\chi}^2 + V, \tag{III.2.18}$$

and V denotes the full potential

$$V \equiv V(\phi) + V(\chi) + V_{\rm int}(\phi, \chi)\ . \tag{III.2.19}$$

In regards to perturbations, the full system of equations in the Newtonian gauge is given by

$$\delta\ddot{\phi}_k + 3H\delta\dot{\phi}_k + \left(\frac{k^2}{a^2} + V_{,\phi\phi}\right)\delta\phi_k = 2\left(2\dot{\phi}\dot{\Phi}_k - V_{,\phi}\Phi_k\right) - V_{,\phi\chi}\delta\chi_k\,, \tag{III.2.20}$$

$$\delta\ddot{\chi}_k + 3H\delta\dot{\chi}_k + \left(\frac{k^2}{a^2} + V_{,\chi\chi}\right)\delta\chi_k = 2\left(2\dot{\chi}\dot{\Phi}_k - V_{,\chi}\Phi_k\right) - V_{,\phi\chi}\delta\phi_k\,, \tag{III.2.21}$$

$$\dot{\Phi}_k + H\Phi_k = \frac{1}{2}\left(\dot{\phi}\delta\phi_k + \dot{\chi}\delta\chi_k\right)\,, \tag{III.2.22}$$

where $\delta\phi_k$, $\delta\chi_k$ and Φ_k represent the Fourier modes of perturbation variables $\delta\phi$, $\delta\chi$ and Φ respectively. We use Eq. (III.2.22) in the integral form to inspect numerical solutions. In this form the equation can be written as

$$\Phi_k = \frac{1}{2a}\int a\left(\dot{\phi}\delta\phi_k + \dot{\chi}\delta\chi_k\right)\mathrm{d}t\,. \tag{III.2.23}$$

In addition, the perturbed Einstein equation results in a constraint equation

$$\left(\dot{\phi}^2 + \dot{\chi}^2 - 2\frac{k^2}{a^2}\right)\Phi_k = \dot{\phi}\delta\dot{\phi}_k + \dot{\chi}\delta\dot{\chi}_k - \ddot{\phi}\delta\phi_k - \ddot{\chi}\delta\chi_k\,. \tag{III.2.24}$$

Similarly to Eq. (III.2.1), using the Hartree approximation we replace χ^2 with $\langle\chi^2\rangle$ whenever such a term appears in Eqs. (III.2.20)–(III.2.22). For example,

$$V_{,\chi\chi} = g^2\left(\phi - \phi_{\rm SBP}\right)^2 - m^2 + 12\lambda\left\langle\chi^2\right\rangle . \tag{III.2.25}$$

Eq. (III.2.22) makes it clear that Φ_k is directly sourced by the trapping field perturbation $\delta\chi_k$. Hence, if $\delta\chi_k$ is resonantly amplified, one expects that it also amplifies the metric perturbation. As we will see bellow, this is exactly what happens during the resonance.

The ultimate goal of solving these equations is to compute the primordial curvature perturbation ζ. In terms of the Newtonian metric perturbation it is given by

$$\zeta_k = \Phi_k + 2H\frac{\dot{\Phi}_k + H\Phi_k\left(1+\frac{1}{3}\frac{k^2}{a^2H^2}\right)}{\dot{\phi}^2+\dot{\chi}^2} . \tag{III.2.26}$$

The power spectrum of ζ_k is then computed using

$$\mathcal{P}_\zeta(k) = \frac{k^3}{2\pi^2}\left|\zeta_k\right|^2 . \tag{III.2.27}$$

Since we consider the two field model, inevitably the isocurvature perturbation is also generated at some level. Such a perturbation can be computed using the following expression [111]

$$\mathcal{S}_k = \frac{2}{3}\frac{\delta V\left[3H\left(\dot{\phi}^2+\dot{\chi}^2\right)+\dot{V}\right] + \left[\dot{\phi}\delta\dot{\phi}_k + \dot{\chi}\delta\dot{\chi}_k - \Phi_k\left(\dot{\phi}^2+\dot{\chi}^2\right)\right]\dot{V}}{\left(\dot{\phi}^2+\dot{\chi}^2\right)\left[3H\left(\dot{\phi}^2+\dot{\chi}^2\right)+2\dot{V}\right]} , \tag{III.2.28}$$

where $\delta V = V_{,\phi}\delta\phi + V_{,\chi}\delta\chi$. Similarly to Eq. (III.2.27) we define the spectrum of the isocurvature perturbation to be

$$\mathcal{P}_\mathcal{S}(k) = \frac{k^3}{2\pi^2}\left|\mathcal{S}_k\right|^2 . \tag{III.2.29}$$

Because the χ field is heavy when the pivot scale exits the horizon, $\mathcal{S}_k$ is negligible on those scales (see Fig. III.7 for an example). On smaller length scales, for modes exiting the horizon during the trapping phase, this is no longer true. As it is well known (see for example Ref. [111]) a non-zero isocurvature perturbation can source the curvature one, even on superhorizon scales. But this depends on the reheating scenario and other factors. Since we assume prompt reheating for the purpose of this work, we do not include the contribution from $\mathcal{S}_k$ to ζ_k during the post inflationary evolution. The study of these effects and their consequences for the mass distribution of PBHs is left for future work.

Furthermore, as pointed out in Ref. [112], under certain conditions in hybrid inflation with a waterfall transition, quantum fluctuations can dominate over the classical motion

of the inflaton and the waterfall field, and stochastic effects may become dominant. Usually, a perturbative expansion is performed about the inflaton quantum fluctuations around the classical background quantities; however, in the above-mentioned situations, the perturbative expansion breaks down, and it may become necessary to employ the stochastic formalism [113–115]. Therefore, we compare the classical contributions in the Friedmann equation, $m_{\rm pl}^2 V_{,\phi}/V$ and $m_{\rm pl}^2 V_{,\chi}/V$, with the quantum contribution $H/2\pi$ [116]. In this context, the ratios between the classical and quantum effects for the inflaton field and the waterfall field are defined as

$$\Delta_\phi \equiv HV/(2\pi m_{\rm pl}^2 V_{,\phi}), \tag{III.2.30}$$

$$\Delta_\chi \equiv HV/(2\pi m_{\rm pl}^2 V_{,\chi}), \tag{III.2.31}$$

respectively. Namely, $\Delta > 1$ indicates that quantum effects are dominant, whereas $\Delta < 1$ implies that classical effects are dominant. For the hybrid inflation model considered in this work, we calculate these ratios and plot them in field space, as shown in Fig. III.5. As can be seen from this figure, for the parameter choices adopted in the present hybrid inflation potential, both $\Delta_\phi \sim 10^{-10}$ and $\Delta_\chi \sim 10^{-15}$ are sufficiently small. This result indicates that stochastic effects are negligible is well justified in this time.

III.3 The Second Stage and The Total Duration of Inflation

One of the traditional issues related to RMI is its large spectral running [29, 34]. Usually it takes only a few tens of e-foldings of inflation before perturbations become non-linear. Such a short inflation is not sufficient if it is to solve the horizon and flatness problems. The duration of inflation can be enlarged if the $V(\chi)$ part of the potential is flat enough, so that the waterfall phase can provide the missing number of e-foldings. This is in contrast to the standard picture of hybrid inflation [26, 27], where the waterfall phase is assumed to be completed within less than an e-folding.

For this purpose we consider a hilltop type potential in Eq. (III.0.3), which consists of two free parameters m and λ. Only these two terms are assumed to be significant during the waterfall. Higher order terms can be added to stabilise the potential, but they are taken to be inconsequential for the dynamics of inflation.

To estimate the minimum number of e-foldings of inflation that is required to solve the flatness and horizon problems of Hot Big Bang we assume prompt reheating at the end of inflation. In this approximation we can write [61]

$$N \simeq 56 - \frac{2}{3}\ln\frac{10^{16}\text{GeV}}{\rho_*^{1/4}} - \frac{1}{3}\ln\frac{10^{9}\text{GeV}}{T_{\rm reh}}\,, \tag{III.3.1}$$

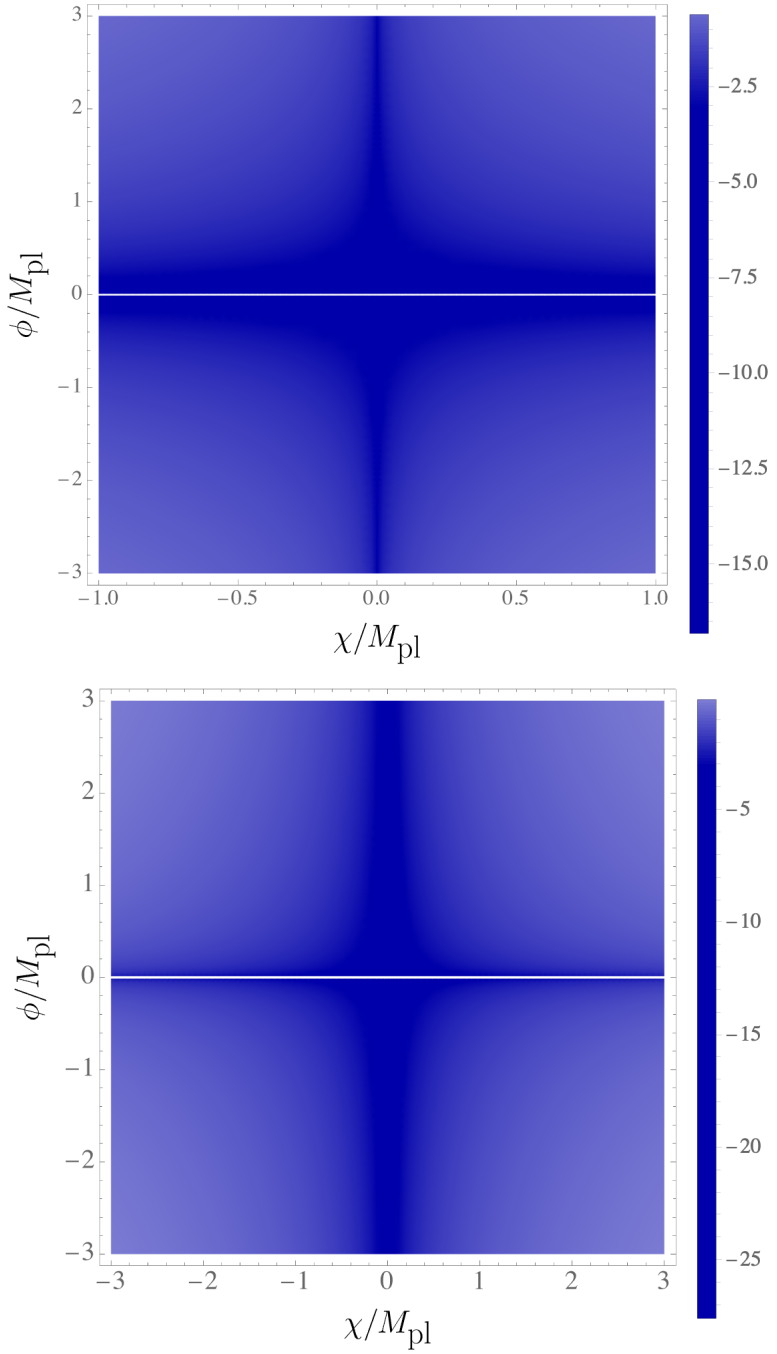

Fig. III.5 Illustration of stochastic effects. We consider the field space spanned by the inflaton field ϕ on the vertical axis and the waterfall field χ on the horizontal axis. On this field space, the ratio Δ between the classical and quantum effects is plotted. The values on the colorscale of the DensityPlot indicate powers of 10.

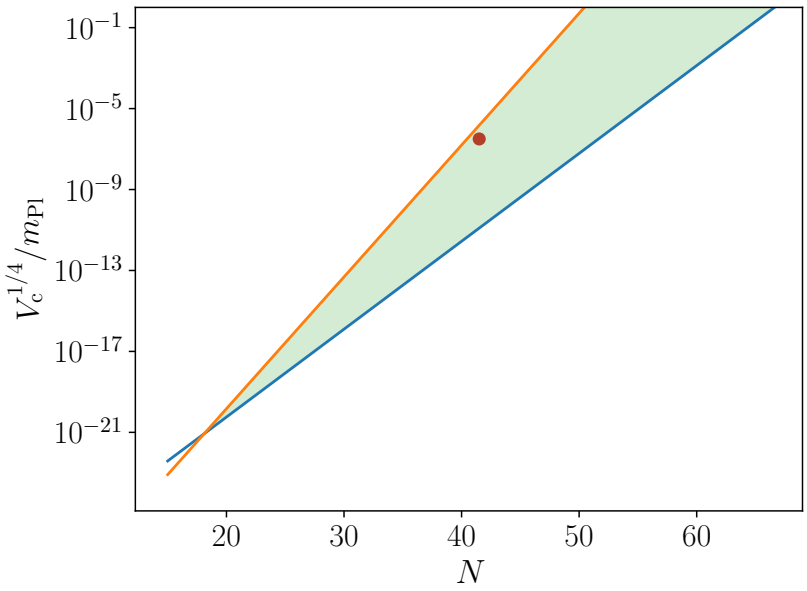

Fig. III.6 Allowed range of the energy scale of inflation (green shaded region). Orange and blue lines represent bounds in Eqs. (III.3.3) and (III.3.5) respectively. The red dot marks the value of the model specified in section III.4.

where N is the number of e-foldings defined by $N \equiv \ln a/a_0$, $\rho_*^{1/4}$ is the energy scale of inflation when the pivot scale leaves the horizon in units of GeV and $T_{\rm reh}$ is the temperature at reheating, also in GeV. We can invert this expression and write

$$\frac{T_{\rm reh}}{\rm MeV} \simeq 1.7 \times 10^7 \, {\rm e}^{3(N-56)} \frac{m_{\rm pl}^2}{\sqrt{V_{\rm c}}} \,, \tag{III.3.2}$$

where $V_{\rm c}$ is defined in Eq. (III.0.1) and we used the fact that $U(\phi) \ll 1$. There are (at least) two conditions that this equation must satisfy. First, the reheating temperature must be larger than the temperature of the Big Bang Nucleosynthesis, which is $T_{\rm BBN} \sim 1$ MeV [117–119]. It follows from the above equation that the upper bound on the energy scale of inflation must be

$$V_{\rm c} < 3 \times 10^{14} \cdot {\rm e}^{6(N-56)} m_{\rm pl}^4 \,. \tag{III.3.3}$$

On the other hand, for a given duration and the energy scale of inflation, one must make sure that blindly applying Eq. (III.3.2) does not lead to the energy density $\rho_{\rm reh}$ at reheating to become larger than the energy scale at the end of inflation. For this estimate it will be sufficient to assume constant energy density during inflation and use the relation of the thermalised radiation

$$\rho_{\rm reh} = \frac{\pi^2 g_*}{30} T_{\rm reh}^4 \,, \tag{III.3.4}$$

where g_* is the effective number of relativistic degrees of freedom. At temperatures $T > 100$ GeV this number is $g_* = \mathcal{O}(100)$. Thus, we find from Eq. (III.3.2) that the condition $V_{\rm end} > \rho_{\rm reh}$, where $V_{\rm end}$ is the energy scale at the end of inflation, leads to the inequality

$$V_{\rm c} > 10^{-19} \left(\frac{\pi^2 g_*}{30}\right)^{\frac{1}{3}} \mathrm{e}^{4(N-56)} m_{\rm pl}^4 \,, \tag{III.3.5}$$

where we took $(V_{\rm c}/V_{\rm end})^{\frac{1}{3}} \sim 1$.

Putting Eqs. (III.3.3) and (III.3.5) together and taking $g_* = 150$ for concreteness and a rough estimate, we find

$$5 \times 10^{-19} \mathrm{e}^{4(N-56)} < \frac{V_{\rm c}}{m_{\rm pl}^4} < 3 \times 10^{14} \cdot \mathrm{e}^{6(N-56)} \,. \tag{III.3.6}$$

This bound is easier to appreciate looking at Fig. III.6. When searching for a viable parameter space of this model, the above condition, together with Eqs. (III.1.13)–(III.1.16), needs to be satisfied.

The effects of radiative corrections to the dynamics of the waterfall field [120] are ignored in this study. We don't expect such corrections to change the picture qualitatively. But their effect on the space of allowed parameter values should certainly be studied, which we plan to do in the future.

III.4 The Primordial Curvature Perturbation

To find models that are compatible with observations and provide large enough primordial perturbation on small scales, we perform numerical simulations. To do that, we first estimate the spectrum using slow-roll approximation for all models in the allowed regions shown in Fig. III.3. This narrows down the set of models which are likely to produce the correct amplitude of the spectrum at the required scales.

We next perform numerical simulations of the exact linear equations Eqs. (III.2.16)–(III.2.22) applied to this narrowed down set of models. Our goal is to find models that give the spectrum with a sharp peak of amplitude $\mathcal{P}_\zeta(k_{\rm max}) \simeq 10^{-1.5}$ at around 35 e-foldings after the pivot scale exits the horizon. Such values are likely to lead to the correct mass distribution of PBHs, as discussed in sec. IV.3.

The parameters of one such model, which we continue using for the rest of the paper, are $\alpha = 0.005$, $A = 4.849$, $B = 5.859$. We found that for this model CMB constraints in Eqs. (III.1.13)–(III.1.16) are best satisfied when the inflaton field value is $\phi_* = 3.89 \times 10^{-9}\, m_{\rm pl}$. Consequently, this leads to the energy scale of inflation $V_{\rm c}^{1/4} = 10^{-6.5}\, m_{\rm pl}$. $N = 35$ e-foldings later the inflaton reaches $\phi_{\rm SBP} = 6.02 \times 10^{-13}\, m_{\rm pl}$. At this moment the trapping field is resonantly excited and rendered unstable. We ran a

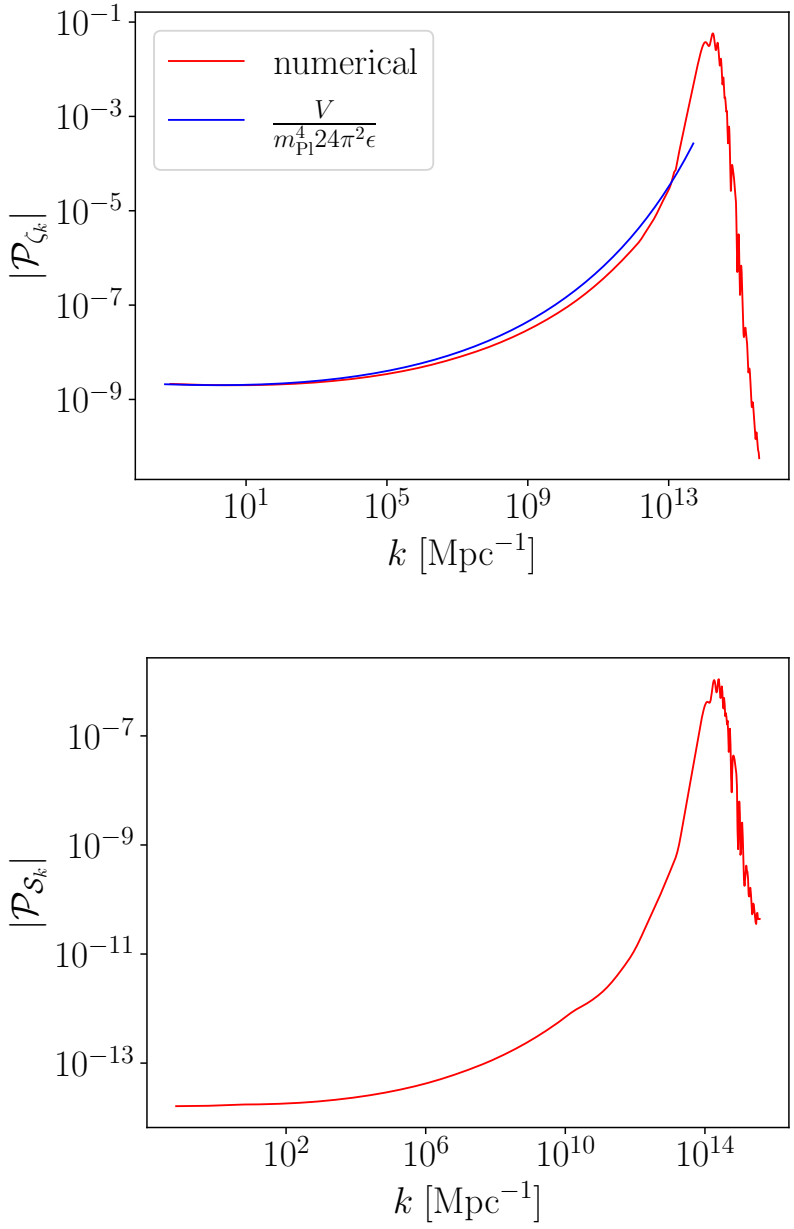

Fig. III.7 Left panel: the primordial curvature perturbation spectrum $\mathcal{P}_\zeta(k)$ (see Eq. (III.2.27)). The red curve indicates numerical results. For comparison we also show (the blue curve) the spectrum computed using the slow-roll approximation (see Eq. (III.4.5)). This curve terminates at the scales that exit the horizon when $\phi = \phi_{\rm SBP}$. Right panel: the spectrum of the isocurvature perturbation $\mathcal{P}_\mathcal{S}(k)$ (see Eq. (III.2.29))

number of simulations to search for parameter values of the waterfall potential that give the right value of $\mathcal{P}_\zeta$ and guarantee a long enough waterfall phase. One such possible model resulted in the trapping field mass $m = 3.3 \times 10^{-13} m_{\rm pl}$ and $g^2 = 0.81$. The quartic self-coupling strength λ is chosen such that the vacuum energy vanishes, i.e., $\lambda = 5/24 \cdot m^4/V(\phi_c) = 1.14 \times 10^{-24}$.

Furthermore, for this choice of parameters, the respective physical quantities are obtained

$$n_s = 0.9743\,, \tag{III.4.1}$$
$$\alpha_s = 0.0067\,, \tag{III.4.2}$$
$$\beta_s = 0.00045\,, \tag{III.4.3}$$
$$r = 3.33 \times 10^{-19}\,. \tag{III.4.4}$$

The duration of inflation from the moment the pivot scale exits the horizon to the end of inflation is $N = 41.5$ e-foldings in this model. It is somewhat shorter than the conventional range from 50 to 60 e-foldings. Nevertheless this value is sufficient to solve Hot Big Bang problems, as detailed in section III.3. Indeed, the discussed model falls within the green region of Fig. III.6.

The numerically computed spectrum is shown in the left panel of Fig. III.7. In that plot we also provide the spectrum (the blue curve) computed using slow-roll approximation [61]

$$\mathcal{P}_\zeta(k) \;=\; \frac{1}{24\pi^2 m_{\rm pl}^4}\,\frac{V}{\epsilon}\bigg|_k\,, \tag{III.4.5}$$

where ϵ is defined in Eq. (III.1.5) and the index 'k' indicates that ϵ and V values must be evaluated at the horizon crossing. As one expects, this expression provides a good approximation of the spectrum for small k, but it starts deviating from the more accurate, numerically computed spectrum once the resonant production of χ particles commences.

In the right panel of Fig. III.7 we also show the spectrum of the isocurvature perturbation. As one can see, it is negligible on the CMB scales (small k values), which is required in order to satisfy the tight bounds on this mode from Planck constraints [93].

In addition to the Newton gauge expressions, we also perform the same simulations for perturbations in the flat gauge (see Appendix A.1), which provides a check of our computations. The results of the latter are not shown, because they are virtually indistinguishable from the Newtonian gauge ones.

Chapter IV

Primordial Black hole

It has been established that dark matter, which interacts only gravitationally and not electromagnetically, is necessary [121] to explain the galactic rotation curves observed [122] from the early 1980s to the 1990s and the structure formation of galaxies and clusters [123]. According to observations, dark matter currently accounts for approximately 30% of the universe, with $\Omega_m = 0.315 \pm 0.007$ [6]; however, its identity remains one of the greatest mysteries in modern cosmology. Candidates for dark matter span a wide range of mass scales, from particles to PBHs, and in this study, we focus on PBHs as the most massive candidates for dark matter. PBHs, originally proposed by Zeldovich and Novikov in 1967 [124], attracted significant attention after Carr and Hawking took the effects of cosmic expansion into account in 1974 [125]. Hawking pointed out that black holes, not limited to PBHs, evaporate through Hawking radiation [126] and therefore possess a finite lifetime that depends on their mass,

$$\tau_{\rm PBH} = 13.8{\rm Gyr}\left(\frac{m_{\rm PBH}}{5.2\times10^{15}{\rm g}}\right)^3. \tag{IV.0.1}$$

Although PBHs with masses $m_{\rm PBH} < 10^{15}$g could in principle lead to several interesting phenomena [127], such as baryogenesis and nucleosynthesis, PBHs in this mass range would have already evaporated over the current age of the Universe. Moreover, alternative explanations exist for such phenomena that do not rely on PBHs. Consequently, Hawking-evaporated PBHs are typically not considered unless they leave stable Planck-mass relics. Therefore, we next focus on the mass range of $m_{\rm PBH} > 10^{15}$g for PBHs. This regime also yields significant results, such as serving as seeds for supermassive black holes in galactic nuclei, generating large-scale structure via Poisson fluctuations, and influencing the thermal and ionization history of the universe. Moreover, they could potentially account for dark matter, which constitutes approximately 30% of the total energy density of the universe. Since PBHs were formed during the radiation-dominated era, they are not subject to the Big Bang nucleosynthesis constraint [128] that "baryons account for at

most 5% of the critical density." In other words, PBHs are non-baryonic and behave in the same manner as other forms of cold dark matter. Among these, the following three mass ranges [129] have attracted particular interest.

- asteroid-mass range : $10^{17}\mathrm{g} - 10^{23}\mathrm{g}$
- intermediate-mass range : $10M_\odot - 10^2 M_\odot$
- supermassive range : $10^{11}M_\odot$ and over

For instance, the possibility that binary black holes in the intermediate-mass range of $10M_\odot - 50M_\odot$ constitute dark matter has attracted significant interest based on observations from LIGO and Virgo. Here, $M_\odot$ denotes the solar mass, 2×10^{33}g. The current observational constraints on this abundance [35, 39] are illustrated in Fig. IV.1 below. It should be noted that, thus far, it is assumed that PBHs possess a monochromatic mass function and are clustered within galactic halos in the same manner as cold dark matter.

In this chapter, we have newly computed the abundance of PBHs produced in the multi-field trapped inflation scenario discussed in the previous chapter III. We have shown in Sec. IV.3 that the masses of the PBHs generated in this scenario lie within the previously mentioned unconstrained asteroid-mass range, and that they can account for almost the entirety of dark matter.

IV.1 Primordial black holes as Dark matter candidate

The formation process of PBHs differs from that of black holes, which result from the gravitational collapse of massive stars. Instead, PBHs are formed when rare and the large fluctuations generated during inflation undergo gravitational collapse upon their re-entry into the horizon. The threshold for this formation, the critical fluctuation δ_c, can be estimated through the framework of Jeans instability. In this chapter, we will again add an overbar to the homogeneous background quantity for discussion due to address fluctuations. First, from the continuity and Poisson equations, the density fluctuation $\delta \equiv (\rho - \bar{\rho})/\bar{\rho} = \delta\rho/\bar{\rho}$ satisfies the equation

$$\frac{\partial^2 \delta}{\partial t^2} + 2H\frac{\partial \delta}{\partial t} - \left(\frac{\bar{\rho}}{2m_{\mathrm{pl}}^2} - \frac{c_s^2 k^2}{a^2}\right)\delta = 0, \tag{IV.1.1}$$

where the sound speed is defined as $c_s^2 = \partial p/\partial\rho$. By treating δ as a particle's position, this can be understood through an analogy with the equation of motion: the first term represents the acceleration of the particle, the second term represents friction proportional to velocity (Hubble drag), and the third term acts as the potential. According to this

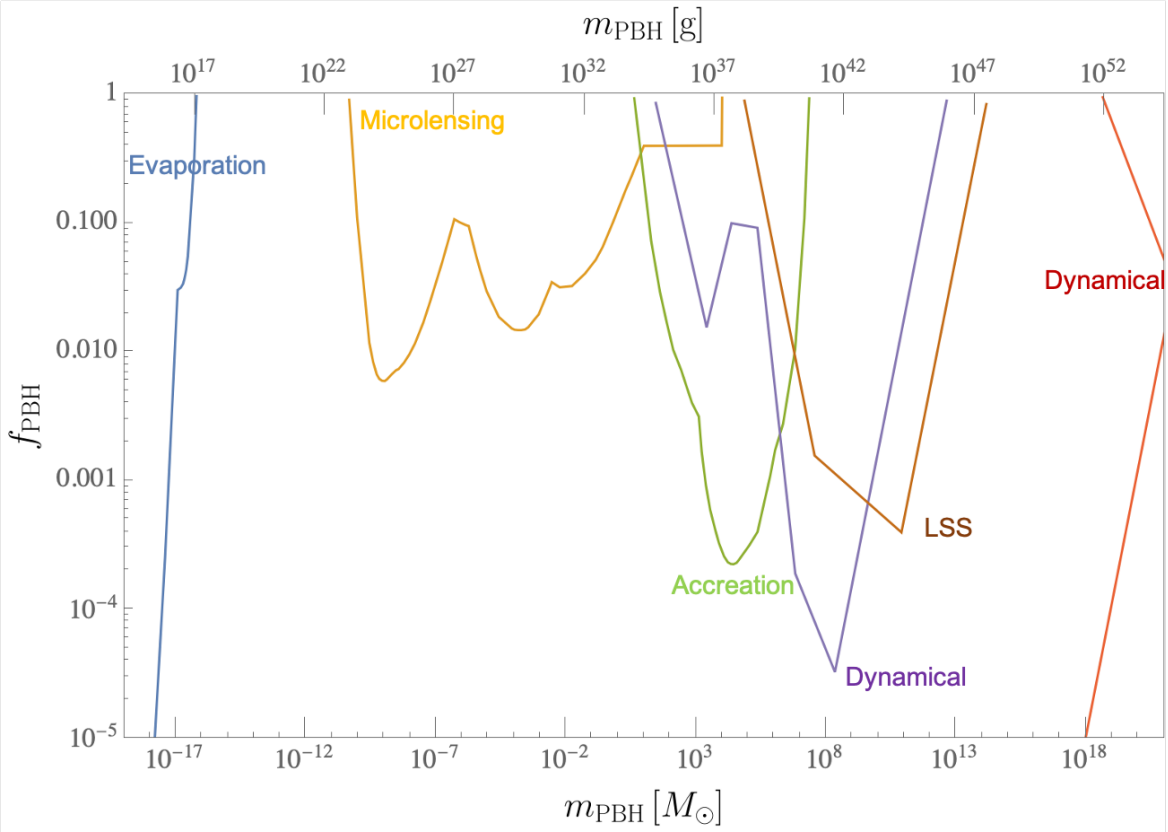

Fig. IV.1 Colored curves represent the observational upper bounds on $f_{\rm PBH}$ [35, 39]. The blue curve corresponds to constraints from the evaporation of the PBHs, including the extragalactic γ-ray background (EGB) [35, 39], the Voyager positron flux (V) [130], and annihilation-line radiation from the Galactic Centre (GC) [131]. The orange curve shows constraints from gravitational lensing, including those from the supernovae (SN) [132], the M31 stars observed by Subaru/HSC [41], the Magellanic Clouds by EROS and MACHO (EM) [133, 134], and the Galactic bulge by the OGLE (O) [135]. The green curve shows the constraints from accretion, including X-ray binaries (XB) [136] and the spectral distortions of the CMB measured by Planck (PA) [137]. The purple curve represents the dynamical constraints, including those from wide binaries (WB) [138], star clusters in Eridanus II (E) [139], halo dynamical-friction (DF) [140], galaxy tidal-distortions (G) [141], heating of stars in the Galactic disk (DH) [140], and the CMB dipole (CMB). The cyan curve indicates constraints from large-scale structure formation [140, 142]. The red curve represents constraints from the CMB dipole anisotropy.

evolution equation, if the coefficient of δ in the third term is negative, the solution for δ tends toward zero, indicating stability. Conversely, if it is positive, the system becomes unstable. This behavior can be interpreted as follows: in the stable case, a large c_s implies that the repulsive pressure during gravitational compression is strong enough to attenuate the density fluctuation, thereby suppressing its growth. In addition to this, if k is sufficiently large, it suggests that matter cannot accumulate effectively on such small scales, preventing the fluctuation from growing. On the other hand, if the third term is positive, the force acts in the same direction as the change in δ, meaning that gravitational growth becomes uncontrollable, and the fluctuation could grow. Therefore, by defining the Jeans length as

$$\lambda_J = \sqrt{\frac{8c_s^2\pi^2 m_{\rm pl}^2}{\bar{\rho}}}, \tag{IV.1.2}$$

the condition for the third term to be positiv

$$\frac{\bar{\rho}}{2m_{\rm pl}^2} > \frac{c_s^2 k^2}{a^2}, \tag{IV.1.3}$$

rewriten in terms of the wavelength $\lambda = 2\pi/p = 2\pi a/k \sim H^{-1}$,that's, the horizon scale, we obtain

$$2\pi\frac{a}{k} > c_s\sqrt{\frac{8\pi^2 m_{\rm pl}^2}{\bar{\rho}}}, \tag{IV.1.4}$$

$$\lambda > \lambda_J. \tag{IV.1.5}$$

From this relation, the critical value δ_c is estimated to be

$$\delta_c \sim c_s^2 \sim \frac{1}{3}. \tag{IV.1.6}$$

More precise analytical calculations [143]

$$\delta_c = \frac{3(1+w)}{5+3w}\sin^2\left(\frac{\pi\sqrt{w}}{1+3w}\right) \approx 0.4, \tag{IV.1.7}$$

have previously been researched. When fluctuations exceeding this threshold re-enter the horizon, they undergo gravitational collapse, leading to the formation of PBHs.

IV.2 Press-Schechter vs Peak

Models have been proposed to analytically describe PBH formation by extrapolating the linear growth solutions of density fluctuations into the nonlinear regime using a spherical

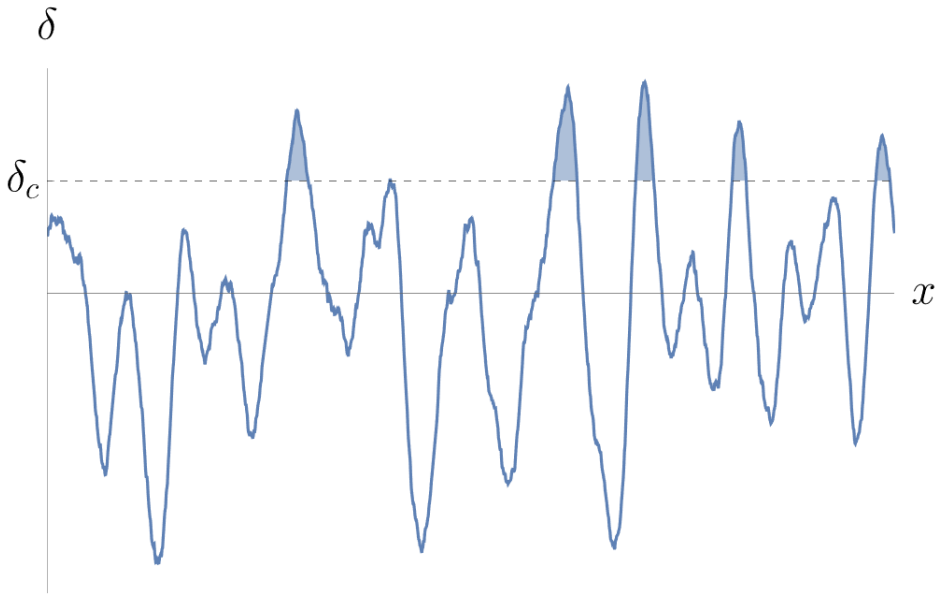

Fig. IV.2 Schematic picture of the fluctuation leading to the PBH formation. The vertical axis represents the density fluctuation δ, while the horizontal axis represents the spatial coordinate x. When the density fluctuation exceeds the threshold δ_c and re-enters the horizon, it undergoes gravitational collapse, resulting in the formation of PBHs.

collapse model. Here, we briefly discuss Press-Schechter theory and peaks theory, which have been widely utilized in the context of nonlinear astronomical formation.

First, in Press-Schechter theory, the mass function $n(M)$ is determined as the number of objects formed per unit volume within the mass range M to $M + \mathrm{d}M$. For a sphere of radius R and mass $M = 4\pi\bar{\rho}R^4/3$, the distribution function of the mass fluctuation δ_M is given by

$$P(\delta_M) = \frac{1}{\sqrt{2\pi\sigma^2(M)}}\exp\left(-\frac{\delta_M^2}{2\sigma^2(M)}\right), \tag{IV.2.1}$$

which follows a Gaussian distribution even after coarse-grained. Here, $\sigma^2(M)$ denotes the variance of the fluctuations. Since PBHs are formed when the fluctuation δ_M at the mass scale M (calculated from the linear growth solution) exceeds a threshold δ_c, the fraction exceeding this threshold is expressed as

$$\beta(\delta_M) = \int_{\delta_c}^{\infty} \mathrm{d}\delta_M \frac{1}{\sqrt{2\pi\sigma^2(M)}}\exp\left(-\frac{\delta_M^2}{2\sigma^2(M)}\right). \tag{IV.2.2}$$

The mass involved in PBH formation per unit volume corresponds to $|\bar{\rho}P(M) - \bar{\rho}P(M + \delta M)|$, which is also equivalent to $n(M)M\mathrm{d}M$. Thus, we obtain

$$n_{\mathrm{PS}}(M)M\mathrm{d}M = 2\bar{\rho}\left|\frac{\mathrm{d}P(M)}{\mathrm{d}M}\right|\mathrm{d}M, \tag{IV.2.3}$$

where the factor of 2 accounts for contributions from regions where the density is lower than the average (negative fluctuations). This theory is frequently used in phenomenology region due to its good agreement with N-body simulations.

In contrast, peak theory considers models where PBHs form at the positions of local maxima of the density that exceed the threshold δ_c. Although the relationship between the number density of PBHs and the distribution of fluctuations is not generally linear, they are not unlinked due to the density fluctuations when the seed of PBHs re-entry the horizon. In this framework, the density fluctuations are first smoothed over a specific scale R_s, known as the smoothing scale, before identifying the peaks. In the original context of astronomical formation, the smoothing scale is determined such that the typical mass of the objects in the region of interest is $M \sim \bar{\rho} R_s^3$, and the threshold δ_c is set to reproduce the observed number density. For a Gaussian distribution, the number density $\mathsf{n}_{\rm peaks}$ [144] in peak theory is given by

$$n_{\rm peaks}(\delta_c, R_c) = \frac{1}{(2\pi)^2}\left[\frac{\langle k^2\rangle(R_c)}{3}\right]^{3/2}(\delta_c^2-1)\exp\left(-\frac{\delta_c^2}{2}\right), \tag{IV.2.4}$$

and β is expressed as

$$\beta_{\rm peaks}(\delta_c) = \frac{(n_s+3)^{3/2}}{6^{3/2}(2\pi)^{1/2}}\delta_c^2\exp\left(-\frac{\delta_c^2}{2}\right). \tag{IV.2.5}$$

In these expressions, $n_{\rm peak}$ is the number density of peaks, ν_c represents the upper limit, and $M(R)$ is the PBH mass formed from a horizon size R, given by $M(R) = (2\pi)^{3/2}R^3\rho$.

Previous studies [145, 146] have already compared Press-Schechter theory with peaks theory. These works indicated that the difference in β between the two theories is not significant when compared to the uncertainty associated with the threshold δ_c. Furthermore, it has been noted that peak theory tends to predict a larger PBH abundance. Consequently, in this study, we adopt the more conservative Press-Schechter theory regarding the PBH abundance.

However, it has been also pointed out that non-Gaussianity can potentially have a significant impact [147, 148] both the abundance and the mass spectrum of PBHs. In this work, we have employed the Press-Schechter under the assumption that the density fluctuations follow a Gaussian distribution. Addressing these complexities is beyond the scope of this paper and remains a subject for future research.

IV.3 Abundance of Primordial black holes

In this section, we focus on PBHs formed during the radiation-dominated era after inflation, since it has been pointed out that PBHs formed before the end of inflation are diluted

exponentially and become negligibly small in abundance [129]. We calculate the mass function (i.e., the mass distribution) of PBHs as predicted by the current model. Roughly speaking, we need the curvature perturbation to be of order $\mathcal{P}_\zeta(k) \sim \mathcal{O}(10^{-1.5})$ [149, 150], so that during radiation domination PBHs are produced via gravitational collapse. Then, the relation between the mass of PBHs and the wave number k can be written by

$$m_{\rm PBH} \sim 10^{20}{\rm g}\left(\frac{k_p}{10^{14}{\rm Mpc}^{-1}}\right)^{-2}. \tag{IV.3.1}$$

This corresponds to $N \sim 35$ e-foldings after the pivot scale exits the horizon. $\mathcal{P}_\zeta$ has the peak at the wave number k_p approximately.

Having the spectrum of the primordial curvature perturbation $\mathcal{P}_\zeta$ (see Fig. III.7) we can compute the abundance of PBHs following, for example, Ref. [34]. First, let us define the fraction of the energy density of PBHs relative to that of Cold Dark Matter (CDM) evaluated at present time

$$f_{\rm PBH} \equiv \frac{\rho_{\rm PBH}}{\rho_{\rm CDM}}, \tag{IV.3.2}$$

where $\rho_{\rm PBH}$ and $\rho_{\rm CDM}$ denote energy densities of PBHs and CDM respectively. Here, dark matter is commonly classified according to the velocity of dark matter particles during the epoch of structure formation after MD. If their velocities are nearly zero, it is referred to as CDM, whereas if they are close to the speed of light, it is classified as hot dark matter (HDM). Since observations of the galaxy distribution, such as those from the Sloan Digital Sky Survey (SDSS), support the CDM scenario, we focus on CDM in this work. Then the mass function per logarithmic bin in mass ${\rm d}f_{\rm PBH}(m_{\rm PBH}){\rm d}\ln m_{\rm PBH} \sim f_{\rm PBH}(m_{\rm PBH})$ can be expressed as

$$f_{\rm PBH}(m_{\rm PBH}) = \frac{\Omega_{\rm m}}{\Omega_{\rm CDM}}\left[\frac{g_*(T)}{g_*(T_{\rm eq})}\frac{g_{*,s}(T_{\rm eq})}{g_{*,s}(T)}\frac{T(m_{\rm PBH})}{T_{\rm eq}}\gamma\beta(m_{\rm PBH})\right], \tag{IV.3.3}$$

where we used the fraction β of the energy density of PBHs $\rho_{\rm PBH}$ relative to the total energy density $\rho_{\rm tot}$ at the formation epoch, $\beta \equiv \rho_{\rm PBH}/\rho_{\rm tot}$. In the above expression, $\Omega_{\rm m}$ and $\Omega_{\rm CDM}$ denote cosmological density parameters of matter and CDM respectively. For these parameters, we adopt the values reported by the Planck team in Ref. [93]. Also, g_*, $g_{*,s}$ denote the number of relativistic degrees of freedom that contribute to the energy and entropy densities respectively. We use their concrete time-dependent values as reported in Ref. [69]. Temperatures $T(m_{\rm PBH})$ and $T_{\rm eq}$ are evaluated at the formation of PBHs and at the matter-radiation equality respectively, while constant γ denotes the ratio between the mass of the PBHs $m_{\rm PBH}$ and the horizon mass $M_{\rm H} = \frac{4\pi}{3}\frac{\rho}{H^3}$ given by

$$m_{\rm PBH} = \gamma M_{\rm H}, \tag{IV.3.4}$$

where the energy density ρ is computed using the Friedmann equation, $\rho = 3m_{\rm Pl}^2 H^2$, and H is the Hubble parameter evaluated at the time of PBH formation. According to a simple analytic formula, the value of γ is estimated to be $\gamma = (1/\sqrt{3})^3 \approx 0.2$ [151].

Assuming that the density perturbation follows Gaussian distribution, we can compute β using the Press Schechter theory [152], which gives

$$\beta(m_{\rm PBH}) = \int_{\delta_{\rm c}}^{\infty} \frac{{\rm d}\delta}{\sqrt{2\pi}\sigma(m_{\rm PBH})} \exp\left[\frac{-\delta^2}{2\sigma^2(m_{\rm PBH})}\right] = \frac{1}{2}{\rm Erfc}\left[\frac{\delta_{\rm c}}{\sqrt{2}\sigma(m_{\rm PBH})}\right]. \tag{IV.3.5}$$

As it is clear from the above, β is a function of the PBH mass, similarly to Eq. (IV.3.3). Here Erfc denotes the complementary error function. The threshold $\delta_{\rm c}$ represents the critical value for PBH formation. The analytical expression for this quantity was computed in Ref. [143]. In this work, we adopt the value $\delta_{\rm c} = 0.45$ [153, 129]. The density perturbation that exceeds this threshold value undergoes gravitational collapse when it re-enters the Hubble horizon, leading to the formation of PBHs.

Furthermore, applying the asymptotic expansion of the complementary error function in Eq. (IV.3.5), we obtain

$$\beta(\sigma) \simeq \frac{\sigma(m_{\rm PBH})}{\sqrt{2\pi}\delta_c} \exp\left[\frac{-\delta_c^2}{2\sigma^2(m_{\rm PBH})}\right], \tag{IV.3.6}$$

where σ is the coarse-grained density perturbation given by

$$\sigma^2(k) = \int_{-\infty}^{\infty} {\rm d}\ln q W^2\left(\frac{q}{k}\right) \frac{4\left(1+w_{\rm eos}\right)^2}{\left(5+3w_{\rm eos}\right)^2}\left(\frac{q}{k}\right)^4 \mathcal{P}_\zeta(q), \tag{IV.3.7}$$

and $w_{\rm eos}$ denotes the equation of state parameter, which is defined by $w_{\rm eos} = p/\rho$, while W denotes the window function, which is taken to be $W(k) = \exp(-k^2/2)$.

Putting all together, the PBH abundance reaches the value $f_{\rm PBH} \sim \mathcal{O}(1)$ in the current model. Moreover, the mass of the PBHs peaks at $m_{\rm PBH} \sim 10^{19.5}$g which is within the asteroid-mass range ($10^{17}{\rm g} \lesssim m_{\rm PBH} \lesssim 10^{23}{\rm g}$) where the observational upper limits (see the colored curves in Fig. IV.3) still allow for the possibility of PBHs being 100% of CDM.

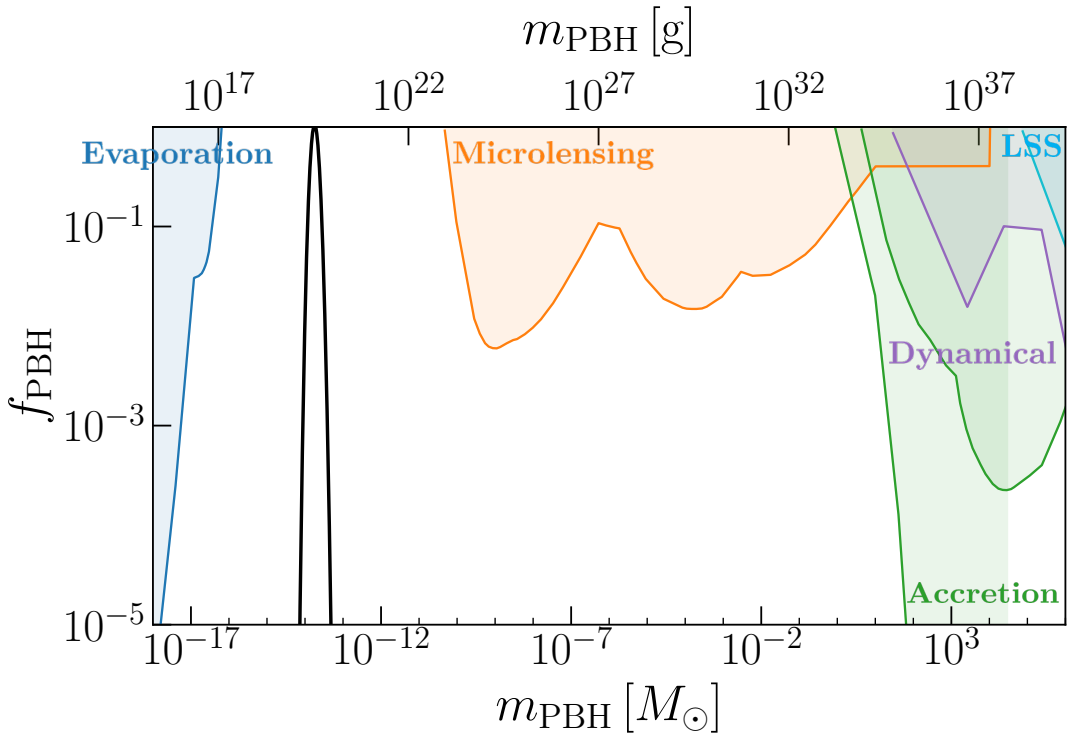

Fig. IV.3 Mass distribution of PBHs (black curve) calculated by the spectrum given in Fig. III.7 as a function of the PBH mass. The vertical axis indicates the energy fraction of PBHs to the CDM (f_{PBH}). The colored curves represent observational upper bounds on f_{PBH} [35, 39]. The blue curve corresponds to constraints from the evaporation of the PBHs, including the extragalactic γ-ray background (EGB) [35, 39], the Voyager positron flux (V) [130], and annihilation-line radiation from the Galactic Centre (GC) [131]. The orange curve shows constraints from gravitational lensing, including those from supernovae (SN) [132], the M31 stars observed by Subaru/HSC [41], the Magellanic Clouds by EROS and MACHO (EM) [133, 134], and the Galactic bulge by the OGLE (O) [135]. The green curve shows the constraints from accretion, including X-ray binaries (XB) [136] and the spectral distortions of the CMB measured by Planck (PA) [137]. The purple curve represents the dynamical constraints, including those from wide binaries (WB) [138], star clusters in Eridanus II (E) [139], halo dynamical-friction (DF) [140], galaxy tidal-distortions (G) [141], heating of stars in the Galactic disk (DH) [140], and the CMB dipole (CMB). The cyan curve indicates constraints from large-scale structure formation [140, 142].

Chapter V

Gravitational waves

Gravitational waves are often described as ripples propagating through spacetime, carrying information about physical phenomena in high-density regions and highly massive astrophysical objects. The amplitude of primordial GWs generated during inflation is constrained by CMB observations to be smaller than the tensor-to-scalar ratio $r < 0.036$ at the 95% confidence level. However, irrespective of whether such primordial GWs are strong enough to be directly observable, induced GWs arise through an independent generation mechanism and are inevitably produced from primordial curvature perturbations. Therefore, in this section we focus on induced gravitational waves generated from primordial curvature perturbations. Although second-order induced GWs are typically suppressed by the square of the curvature perturbations, there exist situations in which they can become larger than the first-order contribution. For instance, if primordial curvature perturbations are amplified on small scales compared to the CMB scale, or if density perturbations grow significantly during a MD era, induced gravitational waves can be enhanced, for example through resonance effects, and exceed the first-order contribution. In particular, the enhancement of primordial curvature perturbations on small scales is realized in several inflationary models, and such enhancement also provides a motivation to explore the production of DM and PBHs. At the same time, in the present model PBHs are produced. As the Universe evolves in time, a certain fraction of these PBHs undergo mergers. During such merger events, GWs with observable amplitudes can be generated from the large spacetime perturbations. If such GWs are observed, they could provide indirect evidence for the existence of PBHs.

In this chapter, we have obtained new results for both induced gravitational waves by tensor perturbations of second order and gravitational waves produced by mergers of PBHs. For the former, we extend the conventional expressions for the gravitational wave spectrum derived under the assumption of a perfect fluid by considering an imperfect fluid that incorporates the viscosity of light particles such as neutrinos. This treatment allows us to implement recent improvements that include the damping of primordial perturbations

predicted in the multi-field trapped inflation model, leading to new predictions for the gravitational wave spectrum. These results are shown in Fig. V.1 of Sec. V.1. On the other hand, for the gravitational waves originating from merging PBH binaries, although previous studies have focused on merger spectra in PBH mass ranges capable of explaining the gravitational wave events observed by LIGO, we present new predictions for the merger spectrum of PBHs in the asteroid-mass range. that arise in the multi-field trapped inflation model and can constitute dark matter candidates. As shown in Fig. V.2 of Sec. V.2, the resulting spectrum depends on the PBH mass and abundance, providing a potential handle to discriminate among inflationary models. Moreover, these signals are shown to be testable with the sensitivity of future gravitational wave observations.

V.1 Induced Gravitational Waves

The large amplitude of the curvature perturbation $\mathcal{P}_\zeta$ on small scales, which is responsible for the formation of PBHs, is also responsible for the (stochastic) induced gravitational waves (SIGWs) that are generated via nonlinear second-order effects. In this section, we calculate the spectrum of such GWs that are produced during the radiation-dominated epoch. For the computation we follow the method detailed in Refs. [49, 53, 154] and adapt it to the current model. The detailed calculation is presented in Appendix B.1. In the absence of anisotropic components, the equation satisfied by tensor perturbations is given in Eq. (II.7.4). In practice, however, density perturbations generate anisotropic stress, rendering the right-hand side nonzero. Multiplying both sides by a^2 and rewriting the equation in terms of conformal time η, we obtain

$$h''(\eta) + 2aHh'(\eta) + k^2 h(\eta) = 4S(\eta). \tag{V.1.1}$$

Here, $S(\eta)$ denotes the source term originating from anisotropic stress

$$S_{\mathbf{k}}(\eta) = \int \frac{\mathrm{d}^3 q}{(2\pi)^{3/2}} e_{ij}(\mathbf{k}) q_i q_j \left(2\Phi_{\mathbf{q}}\Phi_{\mathbf{k}-\mathbf{q}} + \frac{4}{3(1+w)} \left(\mathcal{H}^{-1}\Phi'_{\mathbf{q}} + \Phi_{\mathbf{q}}\right) \left(\mathcal{H}^{-1}\Phi'_{\mathbf{k}-\mathbf{q}} + \Phi_{\mathbf{k}-\mathbf{q}}\right) \right), \tag{V.1.2}$$

where e_{ij} denotes the polarization basis for the $+, \times$ modes defined in Eq. (II.11.10), $\Phi_{\mathbf{k}}$ is the Fourier component of the gravitational potential given in Eq. (II.2.2), and $\mathcal{H} = aH$ is the conformal Hubble parameter. In this case, using the Green's function method, the general solution for $h_{\mathbf{k}}(\eta)$ is given by

$$a(\eta)h_{\mathbf{k}}(\eta) = 4\int^{\eta} \mathrm{d}\bar{\eta}\, G_{\mathbf{k}}(\eta, \bar{\eta}) a(\bar{\eta}) S_{\mathbf{k}}(\bar{\eta}), \tag{V.1.3}$$

where $G_{\mathbf{k}}(\eta,\bar{\eta})$ is the Green's function satisfying $G''_{\mathbf{k}}(\eta,\bar{\eta})+(k^2-a''(\eta)/a(\eta))G_{\mathbf{k}}(\eta,\bar{\eta})=\delta(\eta-\bar{\eta})$. From this, the power spectrum of the tensor perturbation h, $\mathcal{P}_T$, can be obtained

$$\mathcal{P}_T(\eta,k)=4\int_0^\infty \mathrm{d}v\int_{|1-v|}^{1+v}\mathrm{d}u\left(\frac{4v^2-(1+v^2-u^2)^2}{4vu}\right)^2 I^2(v,u,x)\mathcal{P}_\zeta(kv)\mathcal{P}_\zeta(ku), \quad \text{(V.1.4)}$$

where x is the dimensionless variable $x=k\eta$, while $u=|\mathbf{k}-\tilde{\mathbf{k}}|/k$ and $v=\tilde{k}/k$ are integration variables representing the momentum configuration. The function $I(v,u,x)$ is an oscillating function from the source information. Then, we can obtain the spectrum of the gravitational wave

$$\Omega_{\mathrm{GW}}(\eta,k)=\frac{\rho_{\mathrm{GW}}(\eta,k)}{\rho_{\mathrm{tot}}(\eta)}=\frac{1}{24}\left(\frac{k}{a(\eta)H(\eta)}\right)^2\overline{\mathcal{P}_T(\eta,k)}. \quad \text{(V.1.5)}$$

In this expression, the wave number k is related to the frequency f by $k=2\pi f$. The quantity $\rho_{\mathrm{GW}}(\eta,k)$ denotes the energy density of GWs per logarithmic interval of the wave number, and the overline $\overline{\mathcal{P}_T}$ indicates the oscillation average of the tensor perturbation power spectrum $\mathcal{P}_T(\eta,k)$. This quantity is defined as

From the expression for GWs, the spectrum included the scalar perturbations through the source term of the tensor perturbation. The mean free path of weakly interacting light particles such as neutrinos damps the scalar field perturbations on small scales during the radiation-dominated epoch. In other words, perturbations on scales smaller than the mean free path are damped because light particles transport energy from regions with larger fluctuations to those with smaller ones, thereby canceling anisotropies.

$$\Phi_{\mathbf{k}}(\eta)\sim\Phi_{\mathbf{k}(\eta),\mathrm{rad}}(\eta)e^{-k^2/k_D^2}. \quad \text{(V.1.6)}$$

Here, $\Phi_{\mathbf{k}(\eta),\mathrm{rad}}$ denotes the conventional gravitational potential in RD era for a perfect fluid without dissipation effects, and $k_D^2(\eta)$ represents the damping scale [155]

$$k_D^{-2}(\eta)=k^{-2}\int^\eta \mathrm{d}\bar{\eta}\,\frac{2k^2\gamma_{\mathrm{vis}}(\bar{\eta})}{3a^2(\rho+p)}, \quad \text{(V.1.7)}$$

where γ_{vis} denotes the shear viscosity [156, 157],

$$\gamma_{\mathrm{vis}}=\frac{16}{45}\rho_\gamma t_{\mathrm{MFP},\gamma}+\frac{4}{15}\rho_\nu t_{\mathrm{MFP},\nu}\Theta(\eta_{\nu,\mathrm{dec}}-\eta), \quad \text{(V.1.8)}$$

and ρ is the energy density defined in Eq. (I.3.4) and η_{dec} is the time of the decoupling. Using the number density n and the interaction cross section σ, the mean free time is given by $t_{\mathrm{MFP}}=(n\sigma)^{-1}$. In this context, the contribution to the mean free time arising from the Klein–Nishina cross section of photons γ is negligibly small compared to that from the

weak-interaction cross section σ_ν of neutrinos [158, 159]. Substituting the gravitational potential that includes this damping scale into the source term in Eq. (V.1.2), one can obtain the kernel function for gravitational waves and this damping effect influences the induced gravitational waves [51, 155, 160, 52].

Therefore, it also affects induced gravitational waves [51, 155, 160, 52]. Next, in this section, we present the kernel function that incorporates the dissipative effects obtained above, and discuss it in comparison with the kernel function without damping, which is given in Appendix B.1. The effect on the oscillating function I of the source term is given by

$$I_j^{(0)} = -\frac{1-c_s^2\,(u^2+v^2)}{2c_s^4u^2v^2}\Bigg(1-\frac{1-c_s^2\,(u^2+v^2)}{4c_s^2uv}\Big[\,\mathrm{cei}[(1-c_s(u-v))]+\mathrm{cei}[(1+c_s(u-v))] \tag{V.1.9}$$

$$-\,\mathrm{cei}[(1-c_s(u+v))]-\mathrm{cei}[(1+c_s(u+v))]\Big]\Bigg),$$

$$I_y^{(0)} = \frac{\left(1-c_s^2\,(u^2+v^2)\right)^2}{8c_s^6u^3v^3}\Big(\,\mathrm{Sei}[(1-c_s(u-v))]+\mathrm{Sei}[(1+c_s(u-v))]$$

$$-\,\mathrm{Sei}[(1-c_s(u+v))]-\mathrm{Sei}[(1+c_s(u+v))]\Big)\,, \tag{V.1.10}$$

where $c_s^2 = 1/3$ is the sound speed and the subscript j and y denote that the oscillating function is divided into terms of the spherical Bessel function of order zero. Furthermore, the superscript (0) on I denotes the term separated by the order of differentiation of $F = (k_D(\tau)/k_D(\tau_*))^{-2}$, which is normalized by the damping scale $k_D(\tau_*)$ [155, 160] at the pivot scale. The functions cei and Sei are given by

$$\mathrm{cei}(y) = \int_0^\infty \frac{dx}{x} e^{-(u^2+v^2)\kappa_D^2 F[x/x_*]}\,[1-\cos(yx)]\,, \tag{V.1.11}$$

$$\mathrm{Sei}(y) = \int_0^\infty \frac{dx}{x} e^{-(u^2+v^2)\kappa_D^2 F[x/x_*]}\,\sin(yx), \tag{V.1.12}$$

where $\kappa_D = k/k_D(\tau_*)$ is the dimensionless k normalized by the damping scale at the pivot scale. Comparing the kernel function without dissipative effects given in Eq. (B.1.7) in the appendix with the kernel function including the effects presented in Eq. (V.1.9), we find that the first and second terms in Eq. (B.1.7) correspond to $I_j^{(0)}$ and $I_y^{(0)}$ in Eq. (V.1.9), respectively. This implies that the difference between the two expressions (B.1.6V.1.11) arises solely from the exponential factor $e^{-(u^2+v^2)\kappa_D^2 F[x/x_*]}$ appearing in Eq. (V.1.11). This indicates that dissipative effects on the gravitational potential $\Phi_{\rm k}$ enter the kernel function I through the source term $S_{\rm k}$, specifically via the cei, Sei functions, thereby inducing a damping effect in the gravitational wave spectrum.

The result is shown in Fig. V.1. The black solid curve in that figure represents the spectrum of the induced GWs that are generated by scalar perturbations at second order in perturbation theory and are computed above, while the dashed black curve is the same without disspiation effect. As pointed out in Ref. [51, 155, 160, 52], these effect is also found to dissipate the peak and the low-frequency tail of GWs. The pink line shows an approximate spectrum of primary GWs that are generated by vacuum fluctuations during inflation. Other colored curves indicate sensitivity bounds of future planned GW observations (see the caption of Fig. V.1 for details). The figure shows that it becomes evident that our model predicts GWs which fall within the detectability limits of LISA, DECIGO and BBO future observatories.

V.2 Gravitational waves from merging binary PBHs

There is one more source of GWs. As binary PBHs merge they also induce a stochastic GW background [53–55]. We compute the spectrum of such GWs in this section.

Details of the calculation are provided in Appendix B.2, where it is shown that the spectrum obeys the following relation

$$\Omega_{\rm GW}^{(\rm merger)}(f) = \frac{f}{\rho_{\rm c}} \int_0^{z_{\rm sup}} {\rm d}z \, \frac{R(z)}{(1+z)H(z)} \frac{{\rm d}E(f_{\rm s})}{{\rm d}f_{\rm s}}. \tag{V.2.1}$$

In this expression $\rho_{\rm c}$ denotes the critical energy density of the Universe. z is the redshift and $z_{\rm sup}$ is the upper limit of integration, which is computed as $z_{\rm sup} = f_3/f - 1$, where f_3 is the cutoff frequency of GW at the end of the ringdown phase of BH merger [53].

$R(z)$ represents the PBH merger rate and ${\rm d}E(f_{\rm s})/{\rm d}f_{\rm s}$ denotes the energy spectrum of the gravitational wave emitted from the source. Detailed expressions of these functions are provided in Appendix B.2.

As shown in Fig. IV.3, the abundance of PBHs in our model exhibits a pronounced peak at $m_{\rm PBH} \sim 3 \times 10^{19}$g with $f_{\rm PBH} \sim \mathcal{O}(1)$. The GW spectrum that is produced by mergers of such PBHs is shown in Fig. V.2. As can be seen in the figure, GW spectrum falls within the sensitivity region of resonant cavity detectors [56, 57].

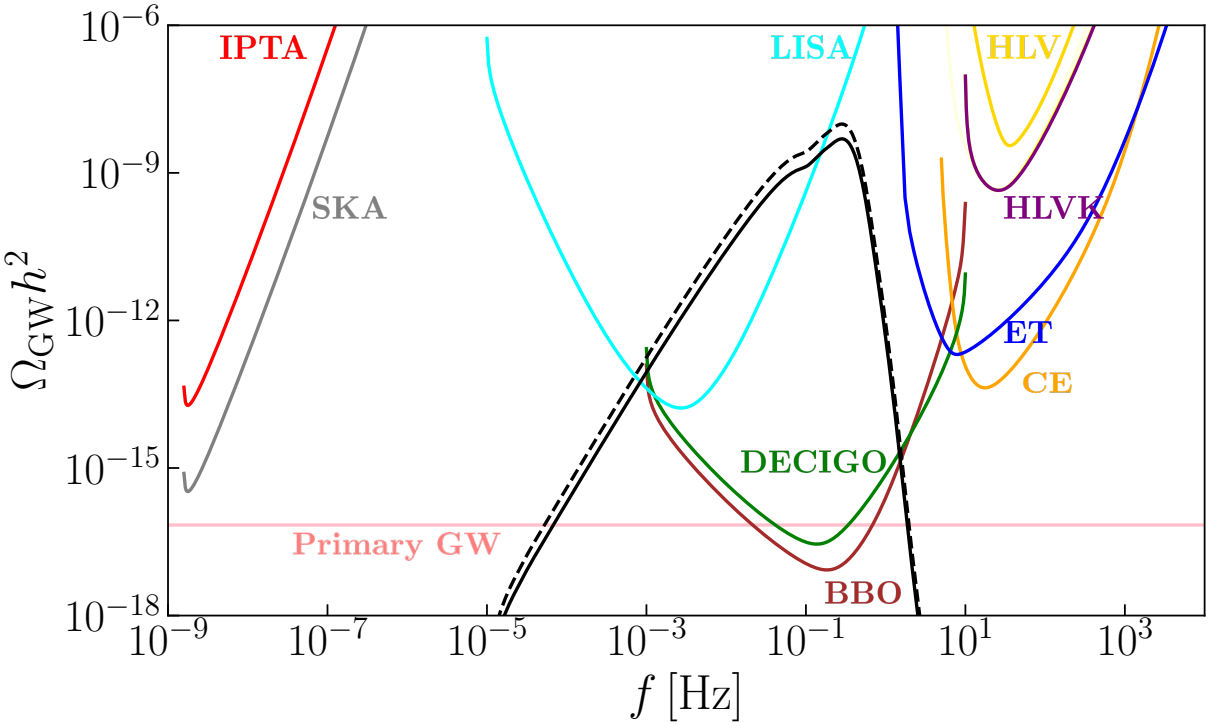

Fig. V.1 Energy density of gravitational waves $\Omega_{\rm GW}h^2$ as a function of the frequency f in units of Hz, where h is the dimensionless Hubble constant. The black dashed curve represents the spectrum of SIGWs, the black solid curve shows GWs with the dissipation, and the pink curve marks the approximate amplitude of primary GWs. Other colored curves show the sensitivities of various gravitational wave observatories [161]. They are the International Pulsar Timing Array (IPTA) (red) [162–165], the Square Kilometre Array (SKA) (grey) [166–168], the Laser Interferometer Space Antenna (LISA) (cyan) [169, 170], the Deci-Hertz Interferometer Gravitational-Wave Observatory (DECIGO) (green) [171–174], the Big-Bang Observer (BBO) (brown) [174–177], the Hanford-Livingston-Virgo (HLV) (yellow) [178–180], the Hanford-Livingston-Virgo-KAGRA (HLVK) (purple) [181, 182], the Einstein Telescope (ET) (blue) [183–186], and the Cosmic Explorer (CE) (orange) [187, 188].

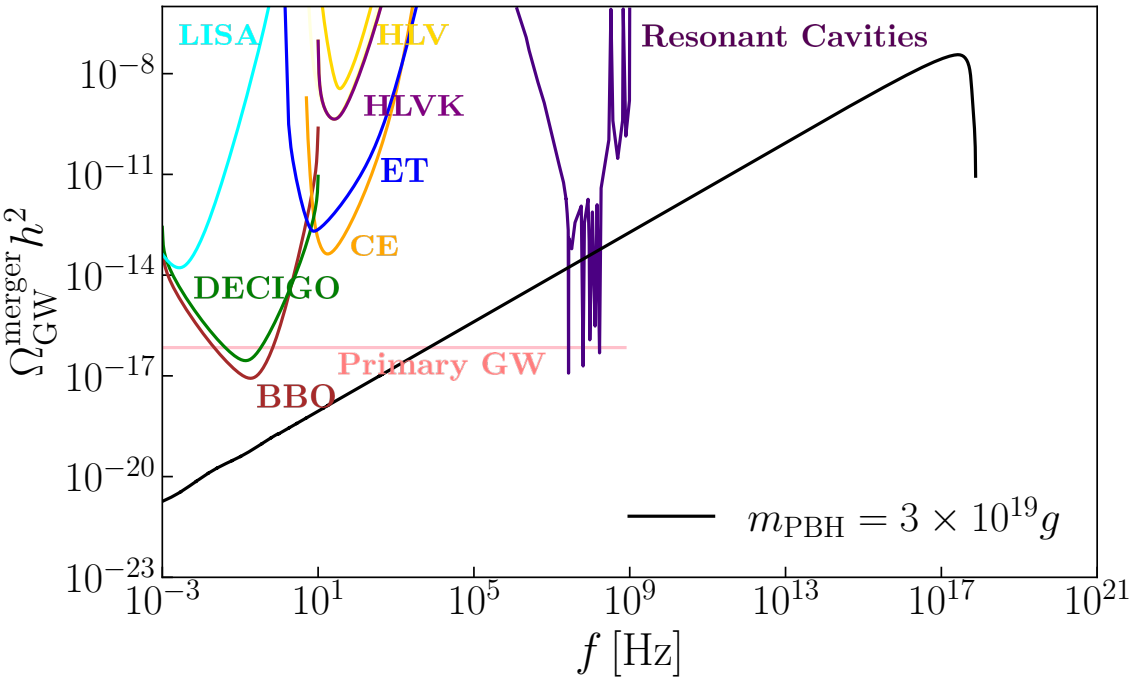

Fig. V.2 Spectra of the GWs from PBH mergers. The horizontal axis represents the frequency f in units of Hz, and the vertical axis shows the energy density of gravitational waves from PBH mergers, $\Omega_{\rm GW}^{\rm merger} h^2$, where h denotes the dimensionless Hubble constant. The black curve represents the spectrum of the gravitational waves from PBH mergers, while the pink curve corresponds to the primary gravitational wave spectrum approximately. The other colored curves indicate the sensitivity curves of future planned gravitational wave observatories [161]. The red curve is the International Pulsar Timing Array (IPTA), the gray curve is the Square Kilometre Array (SKA), the cyan curve is the Laser Interferometer Space Antenna (LISA), the green curve is the Deci-Hertz Interferometer Gravitational-Wave Observatory (DECIGO), the brown curve is the Big-Bang Observer (BBO), the yellow curve is the Hanford-Livingston-Virgo (HLV), the purple curve is the Hanford-Livingston-Virgo-KAGRA (HLVK), the blue curve is the Einstein Telescope (ET), and the orange curve is the Cosmic Explorer (CE). The dark purple curve is the resonant cavity of axion detection [56, 57].

Chapter VI

Swampland Distance Conjecture

In this chapter, we examine how the Swampland Conjecture, which imposes consistency conditions between a UV-complete theory and an effective field theory (EFT), constrains specific inflation models. An EFT is characterized by a finite energy cutoff within which it is valid. In other words, a low-energy EFT can always be obtained by integrating out the UV degrees of freedom from a high-energy theory. Conversely, when approaching from the low-energy side, the theory remains in the landscape only up to its cutoff scale, or beyond this scale, it may enter the swampland, where embedding into a UV-complete theory becomes impossible. By imposing the Swampland Conjecture from this low-energy perspective, it is believed that one can access quantum gravity or string theory. In particular, the Swampland Distance Conjecture can also impose constraints on the energy cutoff scale relevant for inflation. In this chapter, as constraints on inflation models, we apply both the Swampland Distance Conjecture and the well-known Lyth bound, thereby restricting the parameter space of specific inflationary scenarios. As shown in Fig. VI.6 of Sec. VI.3, we find that these constraints are in fact more stringent than those derived from conventional bottom-up observations, such as the Planck 2018 data.

VI.1 Bound from the Swampland distance conjecture

By using SDC, the authors in Refs. [189, 190] argues that the Hubble expansion rate during the primordial inflation should be smaller than the cutoff scale, $H \leq m_{\rm pl} e^{-\lambda_{\rm dc}\Delta\phi/m_{\rm pl}}$. Here $\lambda_{\rm dc}$ is the exponential rate at which an infinite tower of states becomes light, $m_{\rm pl}$ is the (reduced) Planck mass ($\simeq 2.4 \times 10^{18}$ GeV), and $\Delta\phi$ is the excursion distance of the inflaton ϕ during the inflation. The constraint can be viewed as the upper bound on the field excursion

$$\frac{\Delta\phi}{m_{\rm pl}} \leq \frac{1}{\lambda_{\rm dc}} \log\left(\frac{m_{\rm pl}}{H}\right). \tag{VI.1.1}$$

When we rewrite this inequality as a relation between $\Delta\phi$ and the tensor-to-scalar ratio r, we obtain

$$\frac{\Delta\phi}{m_{\rm pl}} \leq \frac{1}{2\lambda_{\rm dc}} \log\left(\frac{2}{\pi^2 A_s r}\right), \tag{VI.1.2}$$

where A_s is the amplitude of the curvature perturbation ($\sim 2.1 \times 10^{-9}$) produced by the inflation at the horizon crossing of a large scale (e.g., $\sim 0.05{\rm Mpc}^{-1}$) [6]. Based on the emergent string conjecture [191], the sharpened distance conjecture [192, 193] (see also [194]) puts lower bound on the parameter $\lambda_{\rm dc}$ to be $\lambda_{\rm dc} \geq \frac{1}{\sqrt{d-2}}$, where d is the number of dimensions. For a concrete values of $\lambda_{\rm dc}$, the following three are chosen in this paper.

$$\lambda_{\rm dc} = \begin{cases} 1 & \text{(a reference value)}, \\ \sqrt{\frac{D-2}{(D-d)(d-2)}} = \sqrt{\frac{3}{2}} & \text{(Kaluza Klein (KK) tower)}, \\ \frac{1}{\sqrt{d-2}} = \frac{1}{\sqrt{2}} & \text{(string tower)}. \end{cases} \tag{VI.1.3}$$

Here D is the dimension before the compactification for the KK tower, and we take $D = d + 1$ and $d = 4$. The first one $\lambda_{\rm dc} = 1$ is just for reference for simplicity. The second one is derived naturally from the dimension reduction, and it is the same as the case for the KK tower. The third one is the minimum value of $\lambda_{\rm dc}$ and corresponds to the case where the string tower is the lightest [192–194]. The upper bounds on $\Delta\phi$ as a function of r are illustrated in Fig. VI.1 for there three cases. We note that, in controlled scenario of string inflation (see e.g. Refs. [12, 195] for reviews), the KK tower is always lighter than the string tower. Therefore, it is natural to take the case of the KK tower, which puts the stringent bound on $\Delta\phi$.

The SDC up to this point provides the upper bounds on the tensor-to-scalar ratio r as a function of the excursion distance of the field $\Delta\phi$. In the next section, we will look at the Lyth Bound, which provides the lower bound on the tensor-to-scalar ratio r as a function of $\Delta\phi$.

VI.2 Lyth Bound

In this section, we consider possible constraints imposed on the model parameters of the inflation by the Lyth Bound. We discuss typical large field models of the slowroll inflation in which the inflation is induced by the inflaton field slowly-rolling on a flat potential in the beginning. In this case, the inflation ends by the breakdown of the conditions for the slowroll at a late time due to the fast-rolling on the potential which becomes steeper than the one in the beginning. Then, the Lyth Bound gives an upper bound on the tensor-to-scalar ratio r as a function of the field excursion $\Delta\phi$. Here, we explicitly state

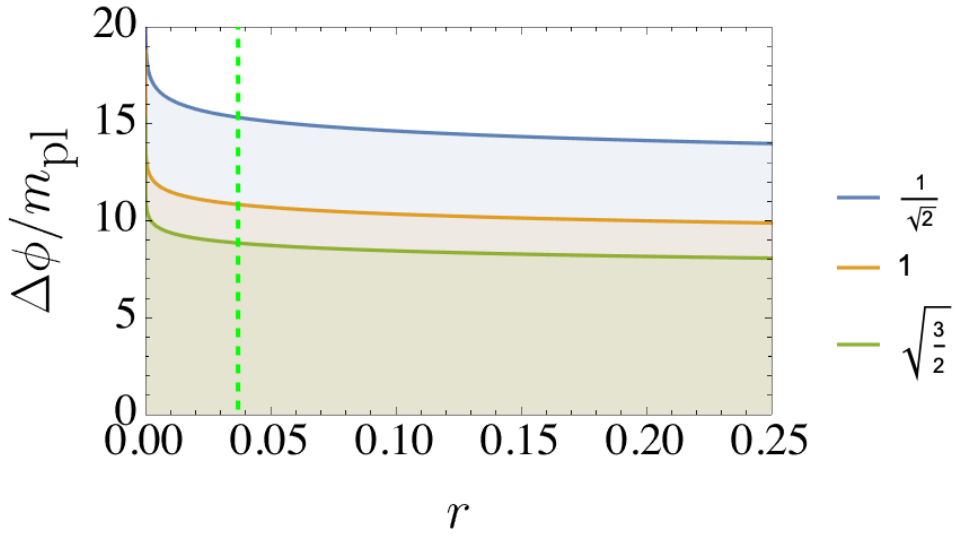

Fig. VI.1 Upper bounds on the tensor-to-scalar ratio r as a function of the excursion distance of the inflaton $\Delta\phi$. Regarding the reference values for $\lambda_{\rm dc}$, we take 1, $\sqrt{\frac{3}{2}}$, and the minimum $\frac{1}{\sqrt{2}}$ in the d=4 dimensions. The vertical green dashed line is the observational upper bound on the tensor-to-scalar ratio, $r < 0.036$ (95% C.L.) by the observational data of the Cosmic Microwave Background (CMB) [7, 8].

the first and second slowroll parameters (I.5.15) again as a function of ϕ as follows.

$$\epsilon(\phi) \equiv \frac{m_{\rm pl}^2}{2}\left(\frac{V_{,\phi}}{V}\right)^2, \tag{VI.2.1}$$

$$\eta(\phi) \equiv m_{\rm pl}^2\left(\frac{V_{,\phi\phi}}{V}\right)^2. \tag{VI.2.2}$$

where the subscript $,\phi$ denotes the differentiation with respect to ϕ. The e-folding number (I.4.5) during the inflation is explicitly showed similarly by

$$N(t) \equiv \ln\frac{a_{\rm end}}{a(t)} = \int_{a(t)}^{a_{\rm end}}\frac{da}{a} = \int_t^{t_{\rm end}} H dt, \tag{VI.2.3}$$

where the subscript *end* represents the value at the end of the inflation $t = t_{\rm end}$.

To solve both the horizon problem and the flatness problem, the e-folding number $N(t_{\rm CMB})$ between a kind of the initial time $t = t_{\rm CMB}$ [1], and the end of inflation ($t = t_{\rm end}$) must be greater than 47 – 62. The upper limit (N=62) comes from the upper bound on the energy scale of the potential of the inflation $V^{1/4} \lesssim 10^{16}$ GeV, which corresponds to the upper bound on the tensor-to-scalar ratio $r < 0.036$ [7, 8]. On the other hand, the lower limit ($N = 47$) comes from the most conservative lower bound on the reheating temperature after inflation ($T_R > 4$ MeV [196]). This is obtained from the conditions for the successful

[1] Correctly, at $t = t_{\rm CMB}$, the mode, which produced the fluctuation of the CMB, exited the horizon. This is not the initial time. The actual initial time $t_{\rm initial}$ should be shorter than $t_{\rm initial} \leq t_{\rm CMB}$

Big Bang nucleosynthesis in terms of the thermalization of background neutrino and keeping the neutron to proton ratio (n/p) unchanged even by the scatterings of the emitted high-energy particles off the background particles [117, 197, 118, 198, 119, 196].

Furthermore, expressing this relation as a function of the scalar field ϕ, we have

$$N(\phi_{\rm CMB}) = \int_{\phi_{\rm end}}^{\phi_{\rm CMB}} \frac{V}{V_{,\phi}} \frac{d\phi}{m_{\rm pl}^2}. \tag{VI.2.4}$$

By the definition, the tensor-to-scalar ratio r is also expressed by

$$r \equiv \frac{P_T}{P_\zeta} = 16\epsilon, \tag{VI.2.5}$$

with $P_T = \frac{2V}{3\pi^2 m_{\rm pl}^4}$ is the tensor perturbation, and $P_\zeta = \frac{V}{24\pi^2 m_{\rm pl}^4 \epsilon}$ is the scalar curvature perturbation. Regarding the Lyth Bound, expressing the e-foldings number (VI.2.4) using the slowroll parameter (VI.2.1), we obtain

$$N(\phi_{\rm CMB}) = \int_{\phi_{\rm end}}^{\phi_{\rm CMB}} \frac{1}{\sqrt{2\epsilon(\phi)}} \frac{d\phi}{m_{\rm pl}}. \tag{VI.2.6}$$

Inside the integrand, if we took an initial value as the representative of each variable, e.g., $\epsilon(\phi) = \epsilon(\phi_{\rm CMB})$ at the beginning $t = t_{\rm CMB}$, because of the inequality $\epsilon(\phi_{\rm end}) > \epsilon(\phi_{\rm CMB})$, we obtain

$$r \leq 2.2 \times 10^{-3} \left(\frac{\Delta N}{60}\right)^{-2} \left(\frac{\Delta\phi}{m_{\rm pl}}\right)^2, \tag{VI.2.7}$$

with $\Delta N = N_{\rm end} - N_{\rm CMB}$ and $\Delta\phi = |\phi_{\rm CMB} - \phi_{\rm end}|$, respectively. This inequality is called the Lyth Bound In Fig. VI.2, we plot the Lyth bound which gives the lower bound on $\Delta\phi$ as a function of r.

VI.3 Combined limits from Swampland Distance Conjecture and Lyth Bound

In this section, we consider the region enclosed by the Swampland Distance Conjecture in (VI.1.2) and the Lyth Bound in (VI.2.7) in the 2D-plane of the field distance $\Delta\phi$ and the tensor-to-scalar ratio r. Among the representative four inflation models described in Section I.5, we showed the relationship between the field distance and the tensor-to-scalar ratio which are related each other through the e-foldings number N given in Eq. (VI.2.6). We plot the value of r as a function of $\Delta\phi$ predicted in each model on the same plane and compare it with the region enclosed by the Swampland Distance Conjecture and the Lyth

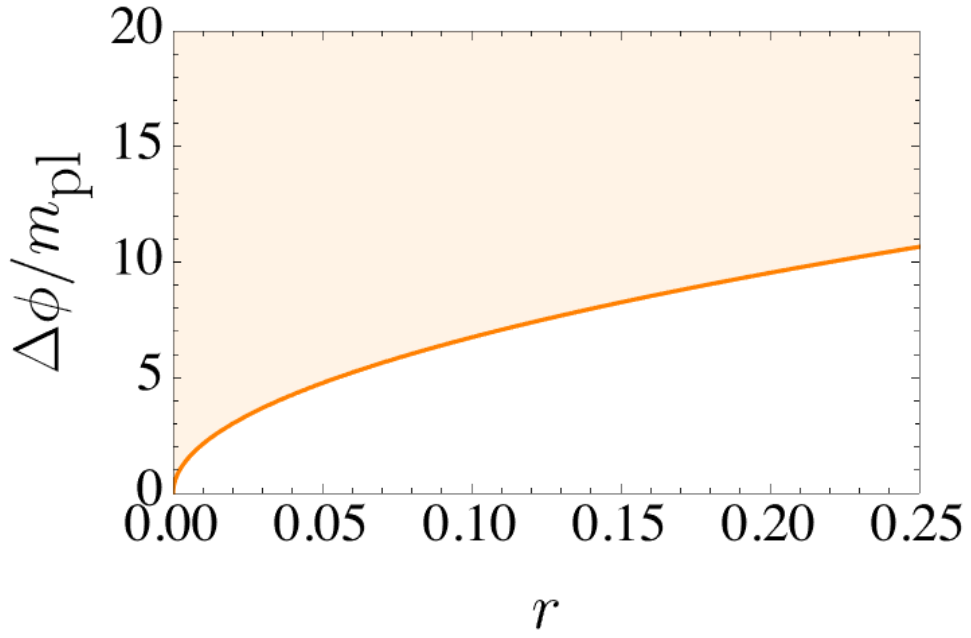

Fig. VI.2 Lower bound on $\Delta\phi$ as a function of r from the Lyth bound. Here we put $\Delta\phi = 60$ for a representative value in large field models.

Bound. Here, the parameters adopted in this analysis are shown in Table VI.1. which refers to the ranges of the parameters studied in the paper of the Planck collaboration in 2018 [93].

Here, taking the chaotic inflation model as an example, we explicitly demonstrate how these quantities can be mapped onto the $r - \Delta\phi$ plane, which will be plotted next. The potential of the chaotic inflation model introduced at the beginning, together with its derivative with respect to ϕ, is given by

$$V = V_0 \left(\frac{\phi}{m_{\rm pl}}\right)^p , \tag{VI.3.1}$$

$$V_{,\phi} = V_0 \frac{p\phi^{p-1}}{m_{\rm pl}^p}, \tag{VI.3.2}$$

Table VI.1 Parameter ranges for each inflation model.

Inflation Model	**Parameter Range**
Chaotic	$0 < p < 4$
Natural	$0.3 < \log_{10}(F/m_{\rm pl}) < 2.5$
Hilltop	$-2 < \log_{10}(\mu_4/m_{\rm pl}) < 2$
α attractor	$-2 < \log_{10}(\alpha) < 4$

Table VI.2 Parameter ranges for representative inflation models.

$$V_{,\phi\phi} = V_0 \frac{p(p-1)\phi^{p-2}}{m_{\rm pl}^p}, \tag{VI.3.3}$$

respectively. The corresponding slow-roll parameters are then given by

$$\epsilon = \frac{1}{2}\left(\frac{V_{,\phi}}{V} m_{\rm pl}\right)^2 = \frac{1}{2}\left(\frac{p m_{\rm pl}}{\phi}\right), \tag{VI.3.4}$$

$$\eta = \frac{V_{,\phi\phi}}{V} m_{\rm pl}^2 = \frac{p(p-1)}{\phi^2} m_{\rm pl}^2, \tag{VI.3.5}$$

where we assume that inflation ends when the slow-roll conditions are violated, namely when $\epsilon \sim 1$ or $|\eta| \sim 1$. Under this assumption, the field value at the end of inflation is given by

$$\frac{\phi_{\rm end}}{m_{\rm pl}} = {\rm Max}\left[\frac{p}{\sqrt{2}}, \sqrt{p(p-1)}\right], \tag{VI.3.6}$$

where Max denotes choosing the larger of the two arguments. Since inflation terminates once either of the conditions $\epsilon \sim 1$ or $|\eta| \sim 1$ is satisfied, the larger value determines $\phi_{\rm end}$. On the other hand, the field value at which perturbations on the CMB scale are generated can be obtained as follows. Considering the e-folding number, we have

$$N = \int_{\phi_{\rm end}}^{\phi_{\rm CMB}} \frac{1}{\sqrt{\epsilon(\phi)}} \frac{{\rm d}\phi}{m_{\rm pl}} = \frac{1}{2pm_{\rm pl}^2}\left(\phi_{\rm CMB}^2 - \phi_{\rm end}^2\right), \tag{VI.3.7}$$

which can be solved for $\phi_{\rm CMB}$ as

$$\phi_{\rm CMB} = \sqrt{2pm_{\rm pl}^2 N + \phi_{\rm end}^2(p)}. \tag{VI.3.8}$$

Thus, once $\phi_{\rm CMB}$ and $\phi_{\rm end}$ are determined, the field excursion $\Delta\phi = |\phi_{\rm CMB} - \phi_{\rm end}|$ can be directly evaluated. Meanwhile, since the first slow-roll parameter has already been obtained, the tensor-to-scalar ratio $r = 16\epsilon$ can also be computed. Therefore, from Eqs. (VI.3.8VI.3.6), it follows that both r and $\Delta\phi$ depend on the inflationary potential parameters p and N. By varying these parameters over appropriate ranges, one can thus plot the allowed region in the $r - \Delta\phi$ plane. The remaining cases, namely the Natural, Hilltop, and α attractor models, can be treated following an analogous procedure.

The results are shown in Fig. VI.4. The parameter $\lambda_{\rm dc}$ of the Swampland Distance Conjecture is taken to be 1. For some values within the parameter range of each inflation model, the number of e-foldings is taken from 47 to 62. For example, $p = 1$ for the Chaotic inflation model is the darkest red line plotted traversing the orange Chaotic region in Fig. VI.4. This red line is obtained by fixing the parameter $p = 1$ and plotting the e-foldings number from 47 to 62. The region obtained when the parameter p is varied within the range of Table VI.1 is the region enclosed by the light orange color. The

two longest orange curves are obtained by fixing the e-foldings number to be 62 (upper one) or 47 (lower one), respectively, and varying the parameter p. Similarly, the plot for Natural Inflation is the black region enclosed by the black curves. The plot for Hilltop Inflation is the green region enclosed by the green curves. The plot for the α attractor is the light blue region enclosed by the light blue curves. The regions of the $T-$model and $E-$model are plotted on extremely close area, so we combined these as the figure of the α attractor. As is clear from the figure, the Natural Inflation model and the α

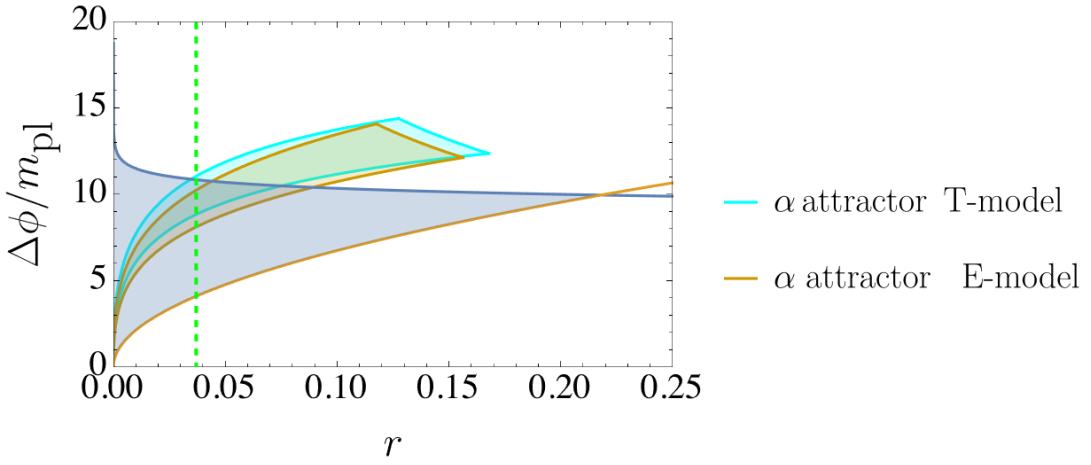

Fig. VI.3 The α attractor T-model (shown in cyan) and the E-model (shown in brown) are plotted separately. As can be seen from the figure, these two models occupy very similar positions compared with the other models such as the Chaotic, Natural, and Hilltop cases. For this reason, in the subsequent figures they are collectively plotted and referred to simply as the α attractor.

attractor inflation model coincide with the case of $p = 2$ for the chaotic inflation model in the large parameter regions of $F/m_{\rm pl}$ and α, respectively. Similarly, it can be seen that Hilltop inflation in the large parameter region of μ also coincides with the chaotic inflation model of $p = 4/3$ [199].

In Fig. VI.5, we chose $\lambda_{\rm dc} = 1/\sqrt{2}$, which is the case for the tower of moduli space. On the other hand, in Fig. VI.6, the case of $\lambda_{\rm dc} = \sqrt{3/2}$, which corresponds to the case of the KK tower.

It is interesting that the case for $\lambda_{\rm dc} = \sqrt{3/2}$ gives the most stringent upper bounds on r and $\Delta\phi$. In this case, it is notable that only the Swampland Distance Conjecture excluded some regions of r at around $r \sim 0.030 - 0.036$ and $\Delta\phi \sim 9 - 10 m_{\rm pl}$, which is stronger than the observational bound from the CMB by the Planck collaboration 2018, $r < 0.036$ (the vertical green dashed line) [7, 8]. Only by such a theoretical requirement, the models of the inflation such as the Natural inflation, the Hilltop inflation and the α-attractors were killed by the Swampland Distance Conjecture (Fig. VI.6).

The Lyth bound would be a good rough guide for observing the general behavior of the prediction of r in inflation models. However, it sometimes gives a wrong prediction.

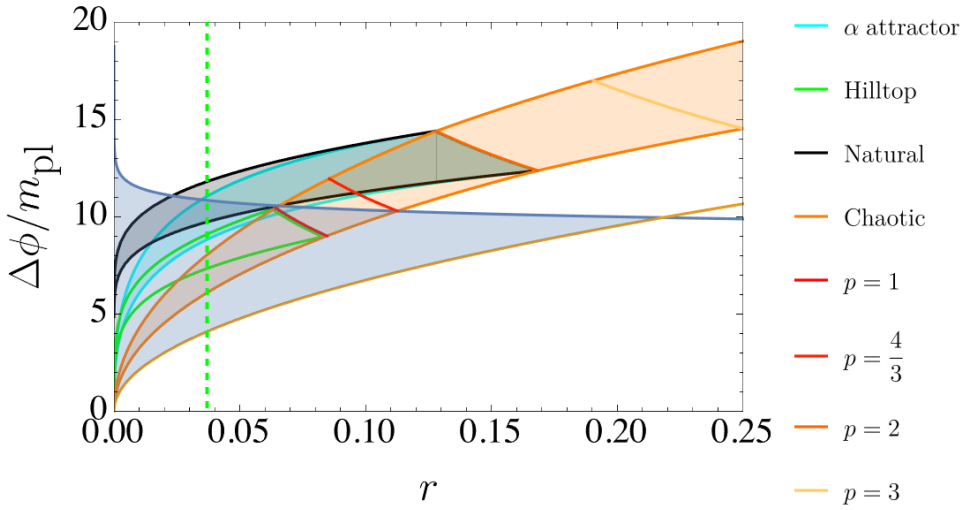

Fig. VI.4 Allowed regions for four inflation models enclosed by the Swampland Distance Conjecture (blue) and the Lyth Bound (brown). We adopted the parameter $\lambda_{\rm dc} = 1$ for the Swampland Distance Conjecture. For the theoretical calculations, we plotted the cases for Chaotic inflation with the red lines for $p = 1, 4/3, 2, 3$, Natural inflation (black), Hilltop inflation (green) and α-attractors (cyan). Two lines mean N=47 (lower one) and N=62 (upper one), respectively. The vertical green dashed line is the observational upper bound on r by the data of the Cosmic Microwave Background (CMB) [7, 8].

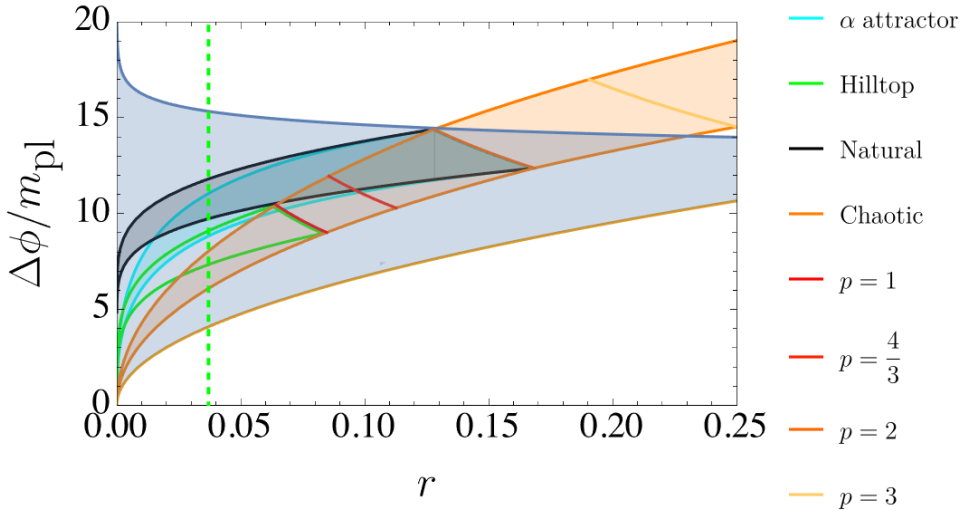

Fig. VI.5 The same as that of Fig. VI.4, but for $\lambda_{\rm dc} = \sqrt{\frac{1}{2}}$.

The results of this study clearly show that when comparing with observed values, it is necessary to calculate the concrete predictions for each model, not just by using the Lyth bound.

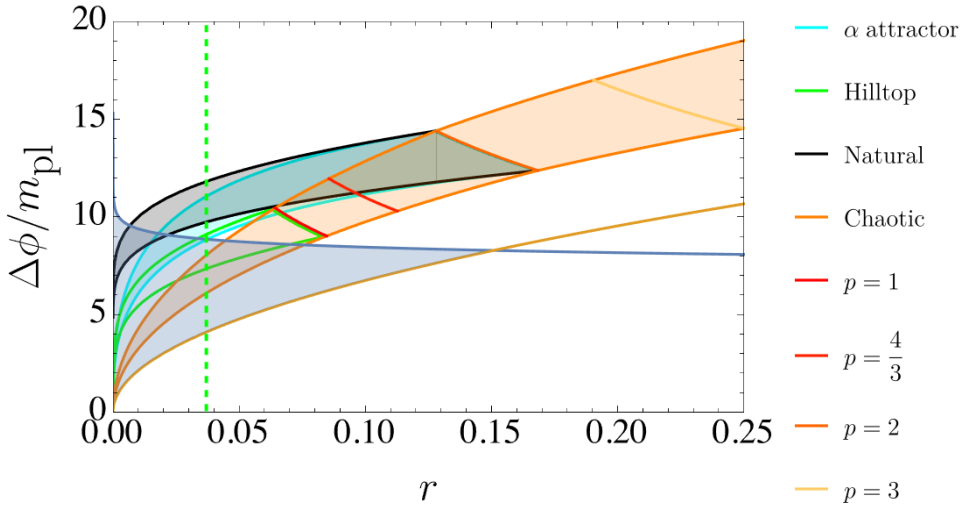

Fig. VI.6 The same as that of Fig. VI.4, but for $\lambda_{\rm dc} = \sqrt{3/2}$.

Chapter VII

Conclusion

In this work, we study a multi-field inflation scenario with a tachyonic trap in the context of supersymmetric running-mass-inflation models. The scenario is reminiscent of hybrid inflation with some modifications. Initially, the inflaton field rolls down the running-mass potential. When the critical point $\phi_{\rm SBP}$ is reached, which we called the symmetry breaking point, the waterfall field is resonantly excited. Such excitations backreact onto the motion of the inflaton field anchoring its value at $\phi_{\rm SBP}$. The remaining e-folding numbers of inflation are generated during the waterfall phase. To make this phase long enough, the potential in the waterfall direction must be sufficiently flat.

The proposed scenario enables us to model running-mass-inflation from the time when observable scales exit the horizon to the end of inflation. It also allows us to compute the spectrum of the curvature perturbation for the full duration of inflation. We find that the spectrum exhibits a sharp peak, corresponding to the scales that exit the horizon around SBP. The enhancement of the spectrum at these scales is due to the shape of the running-mass potential. Additionally, the resonance amplifies the amplitude of the spectrum by several orders of magnitude more.

Such a large perturbation gives rise to PBHs with masses in the range 10^{17}g – 10^{23}g, which are viable dark matter candidates. In Fig. IV.3 of Sec. IV.3, we obtained new results showing that PBH abundances capable of explaining nearly all dark matter can be generated within the currently unconstrained asteroid-mass region. The same perturbation also sources induced gravitational waves in the deci-Hz range, providing a natural signal for upcoming space-based interferometers such as LISA, DECIGO, and BBO. This paper incorporates the latest results that consider the dissipative effect due to the mean free path of light particles in a more realistic imperfect fluid, differing from the conventional spectrum of gravitational waves assuming a perfect fluid. As shown by the black solid curve in Fig. V.1 of Sec. V.1, we obtained results indicating that the gravitational wave spectrum decays compared to the conventional case without damping. Furthermore, PBHs formed in this scenario can subsequently assemble into binaries, whose mergers generate gravitational

waves observable both in resonant cavity experiments via the inverse Gertsenshtein effect and in future space-based detectors. As shown in Fig. V.2 in Sec. V.2, the results for the gravitational wave spectrum when PBHs in the asteroid-mass region merge, without assuming the conventional PBH abundance to be nearly one, suggest that this could become a specific bottleneck for inflation models.

In this paper, in addition to bottom-up observation, we have studied the Swanpland conjecture, which has been obtained in the construction of quantum gravity theory, to address the question of how much we can narrow down the large field inflation models to those that are quantum gravity-theoretically advantageous. Among the Swanpland conjectures, the property known as the Swanpland Distance Conjecture provides an upper bound on the primary gravitational waves produced by large field inflation models. On the other hand, the Lyth bound, which provides a lower bound on primary gravitational waves, plays a complementary role to the Swanpland Distance Conjecture. In this paper, we report the following new points for the first time.

In terms of the upper bound on gravitational waves, some of the major large field inflation models are more strongly constrained by the Swanpland Distance Conjecture than that of the CMB constraints. It is interesting that the case for $\lambda_{\rm dc} = \sqrt{3/2}$ gives the most stringent upper bounds on r as a function of $\Delta\phi$.[1] In this case, it is notable that the Swampland Distance Conjecture alone excluded r at around $r \sim 0.030 - 0.036$ and $\Delta\phi \sim 9 - 10 m_{\rm pl}$, which is stronger than the observational bound from the CMB by the Planck collaboration 2018, $r < 0.036$ [7, 8]. Only by such a theoretical requirement, some parameters in the models of the inflation, such as Natural inflation, the Hilltop inflation or, the α-attractors are excluded by the Swampland Distance Conjecture.

The latest results from the Atacama Cosmology Telescope (ACT)[99, 100] show a slightly larger spectral index compared to Planck 2018. At the CMB pivot scale $k_{\rm CMB}$ $=0.05{\rm Mpc}^{-1}$, the spectral index was constrained to be $n_s = 0.974 \pm 0.003$ (68% C.L.). This result excludes the Natural inflation model at more than the 2σ level. Furthermore, although the α-attractor model showed good agreement with Planck 2018 regarding the tensor-to-scalar ratio and spectral index, the ACT partially allowed for the e-foldings number $N \gtrsim 57$. Many other parameter regions are under tension at the 2σ level.

In particular, the shift towards a larger spectral index by the latest ACT has opened up parameter regions where the parameter p of the Chaotic inflation model is less than one. Interestingly, our results are able to constrain the region where $p < 1$. This means that the ACT and our results are complementary to each other.

[1] As remarked before, this is preferred from a string theory point of view.

Appendix A

Appendices for Chapter III&IV

A.1 The Primordial Perturbation in the Flat Gauge

In the flat gauge the scalar part of the spatial curvature perturbation vanishes. This allows us to write the perturbed line element as

$$\mathrm{d}s^2 = -(1+2\alpha)\,\mathrm{d}t^2 - 2a\beta_{,i}\mathrm{d}x^i\mathrm{d}t + a^2\left(\delta_{ij}+2\partial_i\partial_j\gamma\right)\mathrm{d}x^i\mathrm{d}x^j\,, \tag{A.1.1}$$

where α is the perturbation of the lapse, β is the scalar part of the perturbation of the shift and γ is a scalar function. In this gauge the equations for the field perturbation can be written as [61]

$$\delta\ddot{\varphi}_{kI} + 3H\delta\dot{\varphi}_{kI} + \frac{k^2}{a^2}\delta\varphi_{kI} + V_{,IJ}\delta\varphi_k^J = a^{-3}\frac{\mathrm{d}}{\mathrm{d}t}\left(\frac{a^3}{H}\dot{\varphi}_I\dot{\varphi}_J\right)\delta\varphi_k^J\,, \tag{A.1.2}$$

where repeated indices imply summation and for brevity we used the notation $\varphi_I = (\phi,\chi)$ and similarly for the perturbation. The potential $V(\phi,\chi)$ is provided in Eq. (III.2.19). For the homogeneous value of the χ field, we used the same expression as in Eq. (III.2.15).

Due to spatial homogeneity of the background FRW metric perturbation variables β and γ come in the combination given by [200] [1]

$$\Psi_k \equiv a\left(\beta_k + a\dot{\gamma}_k\right)\,. \tag{A.1.3}$$

This variable satisfies the equation

$$2H\frac{k^2}{a^2}\Psi_k = -\dot{\varphi}_I\delta\dot{\varphi}^I + \left(\ddot{\varphi}_I + \frac{\dot{\varphi}_J\dot{\varphi}^J}{2H}\dot{\varphi}_I\right)\delta\varphi_k^I\,. \tag{A.1.4}$$

[1] The Ψ symbol here should not be confused with the metric perturbation in the Newtonian gauge in Eq. (III.2.12).

In terms of these variables the curvature perturbation on the uniform density slice ζ is given by

$$\zeta_k \;=\; -\frac{H\left(\dot\varphi_I\delta\varphi^I_k+\frac{2}{3}\frac{k^2}{a^2}\Psi_k\right)}{\dot\varphi_I\dot\varphi^I}\,. \tag{A.1.5}$$

In order to check our numerical computations we run the simulations in the Newtonian and flat gauges independently and then check if they give consistent results. To perform the comparison we need the expressions that relate the various quantities in the two gauges. The final result for ζ can be checked by comparing Eq. (A.1.5) above with Eq. (III.2.26). But we also compare intermediate quantities. For example, the Newtonian curvature perturbation Φ_k in Eq. (III.2.12) and Ψ_k in Eq. (A.1.3) above are related by

$$\Phi_k \;=\; H\Psi_k\,. \tag{A.1.6}$$

We checked numerically that Φ_k computed solving Newtonian gauge equations coincide exactly with the flat gauge solution of Ψ_k after performing the conversion of the latter to Φ_k using the above equation. Similarly, we can compare the scalar field perturbations.

Similar conclusions hold for the field perturbations too. Such perturbations in the two gauges are related by

$$\delta\varphi^I_k\big|_{\rm Newt} \;=\; \delta\varphi^I_k\big|_{\rm flat}-\dot\varphi^I\Psi_k\,. \tag{A.1.7}$$

Again, the LHS of this equation, as computed from Eqs. (III.2.20) and (III.2.21), coincides with the RHS, as computed using Eqs. (A.1.2) and (A.1.4).

Appendix B

Appendix for Chapter V

B.1 Detailed calculations of induced gravitational waves

In this section, we introduce the detailed computations of the spectrum of induced gravitational waves in the radiation-dominated epoch [48, 49, 154], which were only summarized in Section V.1. Here we do not consider non-gaussian perturbation for simplicity [201–203]. As given in Eq. (V.1.5), the spectrum of induced gravitational waves is expressed to be

$$\Omega_{\rm GW}(\eta,k)=\frac{\rho_{\rm GW}(\eta,k)}{\rho_{\rm tot}(\eta)}=\frac{1}{24}\left(\frac{k}{a(\eta)H(\eta)}\right)^2\overline{\mathcal{P}_T(\eta,k)}, \tag{B.1.1}$$

where η is the conformal time, the wave number k is related to the GW frequency f via $k=2\pi f$, and $\rho_{\rm GW}(\eta,k)$ is the energy density of gravitational waves per logarithmic wave number. The overline denotes the oscillation average. $\mathcal{P}_T(\eta,k)$ is the power spectrum of the tensor perturbation T which is expressed by

$$\mathcal{P}_T(\eta,k)=4\int_0^\infty {\rm d}v\int_{|1-v|}^{1+v}{\rm d}u\left(\frac{4v^2-(1+v^2-u^2)^2}{4vu}\right)^2 I^2(v,u,x)\mathcal{P}_\zeta(kv)\mathcal{P}_\zeta(ku), \tag{B.1.2}$$

where x is the dimensionless variable $x=k\eta$. The variables u and v are defined by $u=|\mathbf{k}-\tilde{\mathbf{k}}|/k$ and $v=\tilde{k}/k$, respectively. The function $I(v,u,x)$ is an oscillating kernel function encoding the source information given by

$$I(v,u,x)=\int_0^x {\rm d}\bar{x}\frac{a(\bar{\eta})}{a(\eta)}kG_k(\eta,\bar{\eta})f(v,u,\bar{x}), \tag{B.1.3}$$

where G_k is the Green's function, defined by the solution to the differential equation

$$G_k''(\eta,\bar{\eta})+\left(k^2-a''(\eta)/a(\eta)\right)G_k(\eta,\bar{\eta})=\delta(\eta-\bar{\eta}), \tag{B.1.4}$$

with primes denoting derivatives with respect to η. The function $f(v,u,\bar{x})$ represents the source term constructed from second-order scalar perturbations. Since the kernel function I with dissipation has been presented in Sec. V.1, this Appendix provides the expression for the kernel function without dissipative effect, which is shown by the black dashed curve in Fig. V.1. Therefore, by performing the integration using the addition theorem and integration by parts [204], one obtains

$$\begin{aligned}I_{\rm RD}(v,u,x)=\frac{3}{4u^3v^3x}\Bigg(-\frac{4}{x^3}\Bigg(uv\left(u^2+v^2-3\right)x^3\sin x-6uvx^2\cos\frac{ux}{\sqrt{3}}\cos\frac{vx}{\sqrt{3}}\\ +6\sqrt{3}ux\cos\frac{ux}{\sqrt{3}}\sin\frac{vx}{\sqrt{3}}+6\sqrt{3}vx\sin\frac{ux}{\sqrt{3}}\cos\frac{vx}{\sqrt{3}}-3\left(6+\left(u^2+v^2-3\right)x^2\right)\\ \sin\frac{ux}{\sqrt{3}}\sin\frac{vx}{\sqrt{3}}\Bigg)+\left(u^2+v^2-3\right)^2\Bigg(\sin x\Bigg(\mathrm{Ci}\left(\left(1-\frac{v-u}{\sqrt{3}}\right)x\right)\\ +\mathrm{Ci}\left(\left(1+\frac{v-u}{\sqrt{3}}\right)x\right)-\mathrm{Ci}\left(\left|1-\frac{v+u}{\sqrt{3}}\right|x\right)-\mathrm{Ci}\left(\left(1+\frac{v+u}{\sqrt{3}}\right)x\right)\\ +\log\left|\frac{3-(u+v)^2}{3-(u-v)^2}\right|\Bigg)+\cos x\Bigg(-\mathrm{Si}\left(\left(1-\frac{v-u}{\sqrt{3}}\right)x\right)-\mathrm{Si}\left(\left(1+\frac{v-u}{\sqrt{3}}\right)x\right)\\ +\mathrm{Si}\left(\left(1-\frac{v+u}{\sqrt{3}}\right)x\right)+\mathrm{Si}\left(\left(1+\frac{v+u}{\sqrt{3}}\right)x\right)\Bigg)\Bigg)\Bigg),\end{aligned} \tag{B.1.5}$$

as shown in Refs. [150, 205]. Here, the sine integral Si and the cosine integral Ci are defined as

$$\mathrm{Si}(x)=\int_0^x \mathrm{d}\bar{x}\,\frac{\sin\bar{x}}{\bar{x}},\quad \mathrm{Ci}(x)=-\int_x^\infty \mathrm{d}\bar{x}\,\frac{\cos\bar{x}}{\bar{x}}. \tag{B.1.6}$$

To evaluate the spectrum of GWs observed at present, we take the late-time limit $\eta\to\infty$, or equivalently $x\gg 1$. In addition, if we take the oscillation average in this limit, we obtain

$$\begin{aligned}\overline{I^2_{\rm RD}(v,u,x\to\infty)}=\frac{1}{2}\left(\frac{3(u^2+v^2-3)}{4u^3v^3x}\right)^2\Bigg(\left(-4uv+(u^2+v^2-3)\log\left|\frac{3-(u+v)^2}{3-(u-v)^2}\right|\right)^2\\ +\pi^2(u^2+v^2-3)^2\Theta(v+u-\sqrt{3})\Bigg),\end{aligned} \tag{B.1.7}$$

where Θ denotes the Heaviside theta function. Furthermore, as pointed out in Ref. [49], due to the symmetry under the exchange of u and v, we can perform a change of variables from (u,v) to (t,s) with $t=u+v-1$ and $s=u-v$. Under this transformation, the

oscillation-averaged kernel function becomes

$$\overline{I^2_{\rm RD}(t,s,x\to\infty)} = \frac{288(-5+s^2+t(2+t))^2}{x^2(1-s+t)^6(1+s+t)^6}\left(\frac{\pi^2}{4}(-5+s^2+t(2+t))^2\Theta(t-(\sqrt{3}-1))\right.$$
$$\left.+\left(-(t-s+1)(t+s+1)+\frac{1}{2}(-5+s^2+t(2+t))\log\left|\frac{-2+t(2+t)}{3-s^2}\right|\right)^2\right). \tag{B.1.8}$$

Rewriting the power spectrum of the tensor perturbations $\mathcal{P}_T(\eta,k)$ in terms of the new variables s and t, one obtains

$$\mathcal{P}_T(\eta,k) = 2\int_0^\infty {\rm d}t\int_{-1}^1 {\rm d}s\left[\frac{t(2+t)\,(s^2-1)}{(1-s+t)(1+s+t)}\right]^2 I^2(t,s,x\to\infty)\mathcal{P}_\zeta\left(k\frac{t-s+1}{2}\right)\mathcal{P}_\zeta\left(k\frac{t+s+1}{2}\right). \tag{B.1.9}$$

B.2 Detailed calculations of gravitational waves from merging binary PBHs

In this section, we discuss the details of the computations of the gravitational wave spectrum emitted from merging binary PBHs [54, 55, 53] which was only summarized in Section V.2. The spectrum of gravitational waves from the PBH mergers is given by Eq. (V.2.1), which we write here again

$$\Omega_{\rm GW}^{\rm (merger)}(f) = \frac{f}{\rho_{\rm c}}\int_0^{z_{\rm sup}} {\rm d}z\,\frac{R(z)}{(1+z)H(z)}\frac{{\rm d}E(f_{\rm s})}{{\rm d}f_{\rm s}}, \tag{B.2.1}$$

where the Hubble parameter is given by $H(z) = H_0[\Omega_{\rm r}(1+z)^4+\Omega_{\rm m}(1+z)^3+\Omega_\Lambda]^{1/2}$with $\Omega_{\rm r}$ and $\Omega_\Lambda = 1-\Omega_{\rm r}-\Omega_{\rm m}$ being the Ω parameters of radiation, and the present-day cosmological constant, respectively. The quantity $R(z)$ denotes the rate of the mergers for the binary PBHs per comoving volume for a PBH mass $m_{\rm PBH}$, given by

$$R(z) = n_{\rm PBH}\frac{{\rm d}P_t}{{\rm d}t} = \frac{f_{\rm PBH}\Omega_{\rm CDM}\rho_{\rm c}}{m_{\rm PBH}}\frac{{\rm d}P_t}{{\rm d}t}, \tag{B.2.2}$$

where ${\rm d}P_t/{\rm d}t$ is the probability distribution for a PBH merger occurring at time t, given by We assume that PBHs are randomly distributed in space according to a Poisson distribution at the time of their formation. In order to form a binary, the comoving distance x to the nearest PBH must be smaller than the average PBH separation at redshift z

$$f_{\rm PBH}^{1/3}l_{\rm PBH} = f_{\rm PBH}^{1/3}\frac{n_{\rm PBH}^{-1/3}}{1+z}. \tag{B.2.3}$$

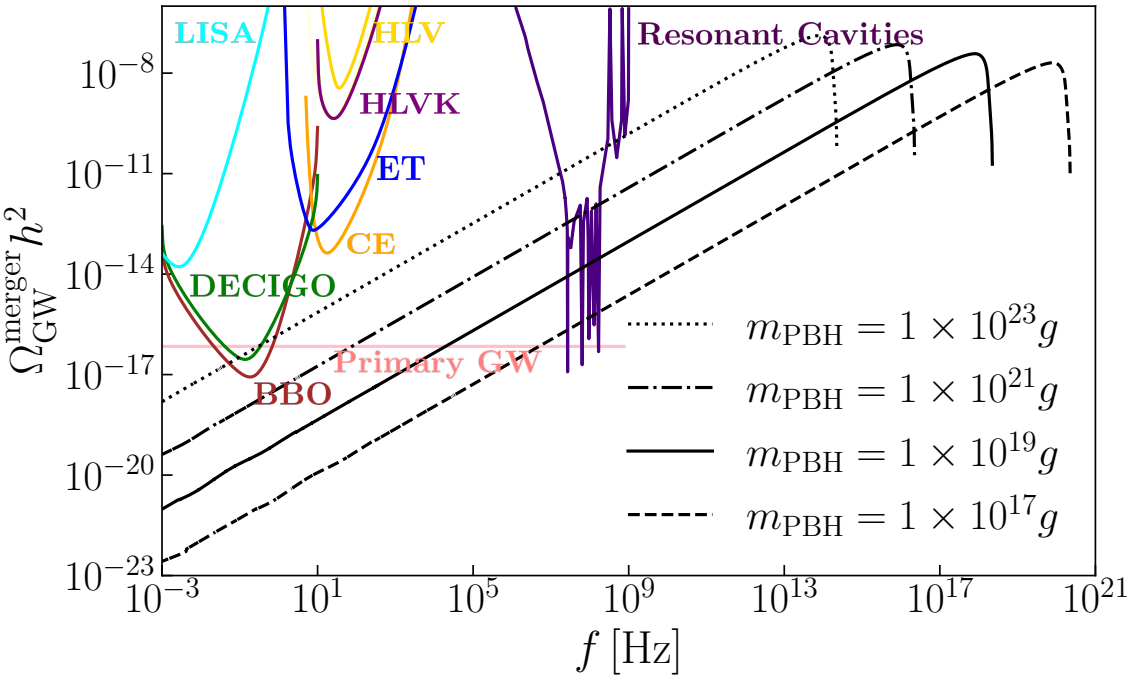

Fig. B.1 GW spectrum generated by PBH mergers. The horizontal axis represents the frequency f in units of Hz, while the vertical axis corresponds to the energy density of the gravitational waves originating from PBH mergers, denoted by $\Omega_{\rm GW}^{\rm merger} h^2$, where h is the dimensionless Hubble parameter. The black curve represents the spectrum of the gravitational waves from mergers of PBH with 10^{17}g(dashed), 10^{19}g(solid), 10^{21}g(dot-dashed), and 10^{23}g(dashed) respectively within the sensitivity range of resonant cavities of axion. Furthermore, the signal from PBHs with 10^{23}g (dotted line) can be observed within the sensitivity of reach not only the resonant cavities of axion but also DECIGO and BBO. The pink curve approximately corresponds to the spectrum of primary gravitational waves. The other colored curves indicate the sensitivity curves of future planned gravitational-wave observatories [161], and resonant cavities for the axion detection [56, 57].

If this condition is satisfied, the PBH located at the nearest distance y to the binary exerts a tidal torque on the pair, leading to the formation of a highly eccentric binary with separation x. Assuming that the binary undergoes Keplerian motion after its formation, the probability $\mathrm{d}P$ that the distances lie within the intervals $(x, x+\mathrm{d}x)$ and $(y, y+\mathrm{d}y)$ is given by

$$\mathrm{d}P = \frac{4\pi x^2 \mathrm{d}x}{n_{\mathrm{PBH}}^{-1}} \frac{4\pi y^2 \mathrm{d}y}{n_{\mathrm{PBH}}^{-1}} \exp\left[-\frac{4\pi y^4}{4n_{\mathrm{PBH}}^{-1}}\right] \Theta(y-x). \tag{B.2.4}$$

These expressions for x and y can be rewritten in terms of the semi-major axis a of the binary and the eccentricity $e = \sqrt{1-(x/y)^6}$, and can further be expressed in terms of the merger time t and the eccentricity e [206]. When the distance y to the third PBH is small, the tidal torque is strong, resulting in a smaller eccentricity e. This is why the binary orbit then becomes closer to circular, making binary formation more efficient and enhancing the merger rate. Conversely, when y is very large, the eccentricity e increases, the orbit approaches a parabolic trajectory, and binary formation becomes less efficient, leading to a suppressed merger rate. As y is increased further, once it exceeds the mean separation of the PBH distribution, the merger rate is expected to decrease even more rapidly. The corresponding threshold value, expressed in terms of the merger time, is denoted by t_c. Taking this into account, the probability distribution for a PBH merger occurring at time t can be rewritten as

$$\frac{\mathrm{d}P_t}{\mathrm{d}t} = \frac{3}{58t} \times \begin{cases} \left(\frac{t}{T_{\mathrm{per}}}\right)^{3/37} - \left(\frac{t}{T_{\mathrm{per}}}\right)^{3/8} & (t < t_{\mathrm{c}}) \\ \left(\frac{t}{T_{\mathrm{per}}}\right)^{3/8} \left(\left(\frac{t}{t_{\mathrm{c}}}\right)^{-29/56} \left(\frac{4\pi f_{\mathrm{PBH}}}{3}\right)^{-29/8} - 1\right) & (t \geq t_{\mathrm{c}}) \end{cases}, \tag{B.2.5}$$

with t_{c} defined by $t_{\mathrm{c}} = (4\pi f_{\mathrm{PBH}}/3)^{37/3} T_{\mathrm{per}}$ and T_{per} given by

$$T_{\mathrm{per}} = \frac{729}{340\pi^2 (1+z_{\mathrm{eq}})^4 (4\pi f_{\mathrm{PBH}}^{16} m_{\mathrm{PBH}}^5 \rho_{\mathrm{c}}^4/3)^{1/3}}, \tag{B.2.6}$$

where z_{eq} is the redshift at the epoch of matter-radiation equality. The typical time t at which mergers occur is given by

$$t = \int_z^\infty \frac{dz'}{(1+z')H(z')}, \tag{B.2.7}$$

In Eq. (V.2.1), the GW energy spectrum of a non–spinning PBH binary from the source, $\mathrm{d}E(f_\mathrm{s})/\mathrm{d}f_\mathrm{s}$, is modeled based on the phenomenological waveforms [207] as

$$\frac{\mathrm{d}E(f_\mathrm{s})}{\mathrm{d}f_\mathrm{s}} = \frac{(G\pi)^{2/3}M_c^{5/3}}{3}\begin{cases} f_\mathrm{s}^{-1/3} & \text{for } f_\mathrm{s} < f_1;\ \text{inspiral phase} \\ w_1 f_\mathrm{s}^{2/3} & \text{for } f_1 \le f_\mathrm{s} < f_2;\ \text{merger phase} \\ w_2 \frac{f_\mathrm{s}^2}{\left(1+\frac{4(f_\mathrm{s}-f_2)^2}{\sigma^2}\right)^2} & \text{for } f_2 \le f_\mathrm{s} \le f_3;\ \text{ringdown phase} \\ 0, & \text{for } f_3 < f_\mathrm{s}, \end{cases} \tag{B.2.8}$$

where $f_\mathrm{s} = (1+z)f$ denotes the frequency emitted at the source and M_c is the chirp mass defined by $M_c^{5/3} = m_{\mathrm{PBH},1}m_{\mathrm{PBH},2}/(m_{\mathrm{PBH},1}+m_{\mathrm{PBH},2})^{1/3}$.

Here, the inspiral phase refers to the stage during which the two PBHs emit gravitational waves, lose energy, and gradually decrease their separation; the merger phase corresponds to the highly nonlinear gravitational stage. The ringdown phase denotes the stage in which the merged object undergoes damped oscillations after the merger. The parameters w_1 and w_2 are fitting coefficients chosen to ensure the continuity of the spectrum, given by $w_1 = f_1^{-1}$ and $w_2 = f_1^{-1}f_2^{-4/3}$. f_1, f_2, f_3, and σ are given

$$\pi M_t f_1 = (1 - 4.455 + 3.521) + 0.6437\eta - 0.05822\eta^2 - 7.092\eta^3 \tag{B.2.9}$$

$$\pi M_t f_2 = (1 - 0.63)/2 + 0.1469\eta - 0.0249\eta^2 + 2.325\eta^3 \tag{B.2.10}$$

$$\pi M_t f_3 = 0.3236 - 0.1331\eta - 0.2714\eta^2 + 4.922\eta^3 \tag{B.2.11}$$

$$\pi M_t \sigma = (1 - 0.63)/4 - 0.4098\eta + 1.829\eta^2 - 2.87\eta^3, \tag{B.2.12}$$

where the total mass $M_t = m_{\mathrm{PBH},1}+m_{\mathrm{PBH},2}$ and the symmetric mass ratio $\eta = m_{\mathrm{PBH},1}m_{\mathrm{PBH},2}/(m_{\mathrm{PBH},1}+m_{\mathrm{PBH},2})^2$.

We now consider the asteroid-mass range ($10^{17}\mathrm{g} \lesssim m_\mathrm{PBH} \lesssim 10^{23}\mathrm{g}$), in which an abundance $f_\mathrm{PBH} \sim \mathcal{O}(1)$ is allowed under observational constraints to become the 100% CDM. Within this mass range, we choose four benchmark values, 10^{17}g, 10^{19}g, 10^{21}g, and 10^{23}g, and compute the corresponding spectra of the gravitational waves from the PBH mergers. These plots are shown as the black curves in Fig. B.1.

Acknowledgements

First of all, I would like to express my greatest appreciation to Kazunori Kohri at Division of Science, National Astronomical Observatory of Japan (NAOJ), Graduate University for Advanced Studies (SOKENDAI) and High Energy Accelerator Research Organization (KEK). Even after his relocation to NAOJ, he continued to support my research as my de facto supervisor. Without his immense support and numerous insightful suggestions, I would not have been able to continue my doctoral studies.

I also would like to express my deep gratitude to Takahiko Matsubara at SOKENDAI and KEK, who took over as my supervisor after Kazunori's departure. I truly appreciate his constructive suggestions and kind advice. I must mention that the coffee he brewed for me was one of the best I have had during these five years. My sincere thanks also go to Yuko Urakawa at SOKENDAI and KEK for providing fruitful discussions and insightful advice throughout my research.

I would like to express my heartfelt appreciation to Mindaugas Karčiauskas at the Center for Physical Sciences and Technology (FTMC) for his exceptional support during our collaboration in Lithuania. His extensive support, ranging from daily life to academic research was instrumental in the progress of my work. His wonderful personality also made our collaboration a truly remarkable and enjoyable experience for me.

I also express my appreciation to those who discussed with me, Tin Long Chau, Shirabe Endo, Yingqiu He, Ryoji Higami, Gaku Isago, Arata Ishige, Sakura Itatani, Kouki Kanazawa, Tomoki Katayama, Shotaro Kawanago, Hayate Kimura, Mikage Kobayashi, Tadashi Kuramoto, Raphael Lehner, Houheng Leong, Jinyang Li, Tomoya Nishiki, Worapat Piensuk, Daisuke Shimozuru, Haruki Takahashi, Ryoto Takai, Lukas Treuer, Tenta Tsuji, Cheng-Tsung Wang, Hidenaga Watanabe, Naoyuki Yamamori, Shotaro Yata.

Finally, I would like to thank all members of the KEK Theory Center.

References

[1] J. Ellis and D. Wands, *Inflation (2023)*, 2312.13238.

[2] K. Sato, *First-order phase transition of a vacuum and the expansion of the Universe*, *Mon. Not. Roy. Astron. Soc.* **195** (1981) 467.

[3] A.D. Linde, *A New Inflationary Universe Scenario: A Possible Solution of the Horizon, Flatness, Homogeneity, Isotropy and Primordial Monopole Problems*, *Phys. Lett. B* **108** (1982) 389.

[4] A.A. Starobinsky, *A New Type of Isotropic Cosmological Models Without Singularity*, *Phys. Lett. B* **91** (1980) 99.

[5] A.H. Guth, *The Inflationary Universe: A Possible Solution to the Horizon and Flatness Problems*, *Phys. Rev. D* **23** (1981) 347.

[6] Planck collaboration, *Planck 2018 results. VI. Cosmological parameters*, *Astron. Astrophys.* **641** (2020) A6 [1807.06209].

[7] BICEP, Keck collaboration, *Improved Constraints on Primordial Gravitational Waves using Planck, WMAP, and BICEP/Keck Observations through the 2018 Observing Season*, *Phys. Rev. Lett.* **127** (2021) 151301 [2110.00483].

[8] M. Tristram et al., *Improved limits on the tensor-to-scalar ratio using BICEP and Planck data*, *Phys. Rev. D* **105** (2022) 083524 [2112.07961].

[9] C. Vafa, *The String landscape and the swampland*, hep-th/0509212.

[10] H. Ooguri and C. Vafa, *On the Geometry of the String Landscape and the Swampland*, *Nucl. Phys. B* **766** (2007) 21 [hep-th/0605264].

[11] N. Cribiori and F. Tonioni, *Cosmological constraints from UV/IR mixing*, 2507.02738.

[12] D. Baumann and L. McAllister, *Inflation and String Theory*, Cambridge Monographs on Mathematical Physics, Cambridge University Press (5, 2015), 10.1017/CBO9781316105733, [1404.2601].

[13] L. Kofman, A.D. Linde, X. Liu, A. Maloney, L. McAllister and E. Silverstein, *Beauty is attractive: Moduli trapping at enhanced symmetry points*, *JHEP* **05** (2004) 030 [hep-th/0403001].

[14] D. Green, B. Horn, L. Senatore and E. Silverstein, *Trapped inflation*, *Phys. Rev. D* **80** (2009) 063533 [0902.1006].

[15] D.J.H. Chung, E.W. Kolb, A. Riotto and I.I. Tkachev, *Probing Planckian physics: Resonant production of particles during inflation and features in the primordial power spectrum*, *Phys. Rev. D* **62** (2000) 043508 [hep-ph/9910437].

[16] O. Elgaroy, S. Hannestad and T. Haugboelle, *Observational constraints on particle production during inflation*, *JCAP* **09** (2003) 008 [astro-ph/0306229].

[17] A.E. Romano and M. Sasaki, *Effects of particle production during inflation*, *Phys. Rev. D* **78** (2008) 103522 [0809.5142].

[18] N. Barnaby, Z. Huang, L. Kofman and D. Pogosyan, *Cosmological Fluctuations from Infra-Red Cascading During Inflation*, *Phys. Rev. D* **80** (2009) 043501 [0902.0615].

[19] N. Barnaby, *Nongaussianity from Particle Production During Inflation*, *Adv. Astron.* **2010** (2010) 156180 [1010.5507].

[20] L. Pearce, M. Peloso and L. Sorbo, *Resonant particle production during inflation: a full analytical study*, *JCAP* **05** (2017) 054 [1702.07661].

[21] Y.-F. Cai, J. Jiang, M. Sasaki, V. Vardanyan and Z. Zhou, *Beating the Lyth Bound by Parametric Resonance during Inflation*, *Phys. Rev. Lett.* **127** (2021) 251301 [2105.12554].

[22] J.F. Dufaux, G.N. Felder, L. Kofman, M. Peloso and D. Podolsky, *Preheating with trilinear interactions: Tachyonic resonance*, *JCAP* **07** (2006) 006 [hep-ph/0602144].

[23] K. Dimopoulos, M. Karčiauskas and C. Owen, *Quintessential inflation with a trap and axionic dark matter*, *Phys. Rev. D* **100** (2019) 083530 [1907.04676].

[24] M. Karčiauskas, S. Rusak and A. Saez, *Quintessential inflation and nonlinear effects of the tachyonic trap mechanism*, *Phys. Rev. D* **105** (2022) 043535 [2112.11536].

[25] S.M. Leach, I.J. Grivell and A.R. Liddle, *Black hole constraints on the running mass inflation model*, *Phys. Rev. D* **62** (2000) 043516 [astro-ph/0004296].

[26] A.D. Linde, *Hybrid inflation*, *Phys. Rev. D* **49** (1994) 748 [astro-ph/9307002].

[27] E.J. Copeland, A.R. Liddle, D.H. Lyth, E.D. Stewart and D. Wands, *False vacuum inflation with Einstein gravity*, *Phys. Rev. D* **49** (1994) 6410 [astro-ph/9401011].

[28] K. Kohri, D.H. Lyth and A. Melchiorri, *Black hole formation and slow-roll inflation*, *JCAP* **04** (2008) 038 [0711.5006].

[29] L. Alabidi and K. Kohri, *Generating Primordial Black Holes Via Hilltop-Type Inflation Models*, *Phys. Rev. D* **80** (2009) 063511 [0906.1398].

[30] L. Alabidi, K. Kohri, M. Sasaki and Y. Sendouda, *Observable Spectra of Induced Gravitational Waves from Inflation*, *JCAP* **09** (2012) 017 [1203.4663].

[31] L. Alabidi, K. Kohri, M. Sasaki and Y. Sendouda, *Observable induced gravitational waves from an early matter phase*, *JCAP* **05** (2013) 033 [1303.4519].

[32] K. Inomata, M. Kawasaki, K. Mukaida, Y. Tada and T.T. Yanagida, *Inflationary Primordial Black Holes as All Dark Matter*, *Phys. Rev. D* **96** (2017) 043504 [1701.02544].

[33] K. Inomata, M. Kawasaki, K. Mukaida, Y. Tada and T.T. Yanagida, *Inflationary primordial black holes for the LIGO gravitational wave events and pulsar timing array experiments*, *Phys. Rev. D* **95** (2017) 123510 [1611.06130].

[34] K. Kohri and T. Terada, *Primordial Black Hole Dark Matter and LIGO/Virgo Merger Rate from Inflation with Running Spectral Indices: Formation in the Matter- and/or Radiation-Dominated Universe*, *Class. Quant. Grav.* **35** (2018) 235017 [1802.06785].

[35] B. Carr, K. Kohri, Y. Sendouda and J. Yokoyama, *Constraints on primordial black holes*, *Rept. Prog. Phys.* **84** (2021) 116902 [2002.12778].

[36] B. Carr and F. Kuhnel, *Primordial Black Holes as Dark Matter: Recent Developments*, *Ann. Rev. Nucl. Part. Sci.* **70** (2020) 355 [2006.02838].

[37] A.M. Green and B.J. Kavanagh, *Primordial Black Holes as a dark matter candidate*, *J. Phys. G* **48** (2021) 043001 [2007.10722].

[38] A. Escrivà, F. Kuhnel and Y. Tada, *Primordial Black Holes*, 2211.05767.

[39] B.J. Carr, K. Kohri, Y. Sendouda and J. Yokoyama, *New cosmological constraints on primordial black holes*, *Phys. Rev. D* **81** (2010) 104019 [0912.5297].

[40] H. Niikura et al., *Microlensing constraints on primordial black holes with Subaru/HSC Andromeda observations*, *Nature Astron.* **3** (2019) 524 [1701.02151].

[41] N. Smyth, S. Profumo, S. English, T. Jeltema, K. McKinnon and P. Guhathakurta, *Updated Constraints on Asteroid-Mass Primordial Black Holes as Dark Matter*, *Phys. Rev. D* **101** (2020) 063005 [1910.01285].

[42] S. Mollerach, D. Harari and S. Matarrese, *CMB polarization from secondary vector and tensor modes*, *Phys. Rev. D* **69** (2004) 063002 [astro-ph/0310711].

[43] K.N. Ananda, C. Clarkson and D. Wands, *The Cosmological gravitational wave background from primordial density perturbations*, *Phys. Rev. D* **75** (2007) 123518 [gr-qc/0612013].

[44] D. Baumann, P.J. Steinhardt, K. Takahashi and K. Ichiki, *Gravitational Wave Spectrum Induced by Primordial Scalar Perturbations*, *Phys. Rev. D* **76** (2007) 084019 [hep-th/0703290].

[45] R. Saito and J. Yokoyama, *Gravitational wave background as a probe of the primordial black hole abundance*, *Phys. Rev. Lett.* **102** (2009) 161101 [0812.4339].

[46] E. Bugaev and P. Klimai, *Induced gravitational wave background and primordial black holes*, *Phys. Rev. D* **81** (2010) 023517 [0908.0664].

[47] H. Assadullahi and D. Wands, *Gravitational waves from an early matter era*, *Phys. Rev. D* **79** (2009) 083511 [0901.0989].

[48] J.R. Espinosa, D. Racco and A. Riotto, *A Cosmological Signature of the SM Higgs Instability: Gravitational Waves*, *JCAP* **09** (2018) 012 [1804.07732].

[49] K. Kohri and T. Terada, *Semianalytic calculation of gravitational wave spectrum nonlinearly induced from primordial curvature perturbations*, *Phys. Rev. D* **97** (2018) 123532 [1804.08577].

[50] R.-G. Cai, S. Pi and M. Sasaki, *Universal infrared scaling of gravitational wave background spectra*, *Phys. Rev. D* **102** (2020) 083528 [1909.13728].

[51] G. Domènech and J. Chluba, *Regularizing the induced GW spectrum with dissipative effects*, *JCAP* **07** (2025) 034 [2503.13670].

[52] Y.-H. Yu and S. Wang, *Silk damping in scalar-induced gravitational waves: a novel probe for new physics*, *Sci. China Phys. Mech. Astron.* **68** (2025) 210412 [2405.02960].

[53] M. Sasaki, T. Suyama, T. Tanaka and S. Yokoyama, *Primordial black holes—perspectives in gravitational wave astronomy*, *Class. Quant. Grav.* **35** (2018) 063001 [1801.05235].

[54] S. Wang, T. Terada and K. Kohri, *Prospective constraints on the primordial black hole abundance from the stochastic gravitational-wave backgrounds produced by coalescing events and curvature perturbations*, *Phys. Rev. D* **99** (2019) 103531 [1903.05924].

[55] K. Kohri, T. Terada and T.T. Yanagida, *Induced gravitational waves probing primordial black hole dark matter with the memory burden effect*, *Phys. Rev. D* **111** (2025) 063543 [2409.06365].

[56] A. Berlin, D. Blas, R. Tito D'Agnolo, S.A.R. Ellis, R. Harnik, Y. Kahn et al., *Detecting high-frequency gravitational waves with microwave cavities*, *Phys. Rev. D* **105** (2022) 116011 [2112.11465].

[57] N. Herman, L. Lehoucq and A. Fúzfa, *Electromagnetic antennas for the resonant detection of the stochastic gravitational wave background*, *Phys. Rev. D* **108** (2023) 124009 [2203.15668].

[58] S. Weinberg, *Gravitation and Cosmology: Principles and Applications of the General Theory of Relativity*, John Wiley and Sons, New York (1972).

[59] S. Weinberg, *Cosmology* (2008).

[60] S. Dodelson, *Modern Cosmology*, Academic Press, Amsterdam (2003).

[61] D.H. Lyth and A.R. Liddle, *The primordial density perturbation: Cosmology, inflation and the origin of structure* (2009).

[62] D. Baumann, *Primordial Cosmology*, *PoS* **TASI2017** (2018) 009 [1807.03098].

[63] A. Friedman, *On the Curvature of space*, *Z. Phys.* **10** (1922) 377.

[64] G. Lemaitre, *A Homogeneous Universe of Constant Mass and Increasing Radius accounting for the Radial Velocity of Extra-galactic Nebulæ*, *Mon. Not. Roy. Astron. Soc.* **91** (1931) 483.

[65] H.P. Robertson, *Kinematics and World-Structure*, *Astrophys. J.* **82** (1935) 284.

[66] A.G. Walker, *On Milne's Theory of World-Structure*, *Proc. Lond. Math. Soc. s* **2-42** (1937) 90.

[67] R.A. Alpher, H. Bethe and G. Gamow, *The origin of chemical elements*, *Phys. Rev.* **73** (1948) 803.

[68] T.S. Coleman and M. Roos, *Effective degrees of freedom during the radiation era*, *Phys. Rev. D* **68** (2003) 027702 [astro-ph/0304281].

[69] K. Saikawa and S. Shirai, *Precise WIMP Dark Matter Abundance and Standard Model Thermodynamics*, *JCAP* **08** (2020) 011 [2005.03544].

[70] K. Saikawa and S. Shirai, *Primordial gravitational waves, precisely: The role of thermodynamics in the Standard Model*, *JCAP* **05** (2018) 035 [1803.01038].

[71] A.R. Liddle and S.M. Leach, *How long before the end of inflation were observable perturbations produced?*, *Phys. Rev. D* **68** (2003) 103503 [astro-ph/0305263].

[72] A. Linde, *Chaotic inflation*, *Physics Letters B* **129** (1983) 177.

[73] F.C. Adams, J.R. Bond, K. Freese, J.A. Frieman and A.V. Olinto, *Natural inflation: Particle physics models, power law spectra for large scale structure, and constraints from COBE*, *Phys. Rev. D* **47** (1993) 426 [hep-ph/9207245].

[74] S. Chongchitnan, *Inflation model building with an accurate measure of e-folding*, *Phys. Rev. D* **94** (2016) 043526 [1605.04871].

[75] S. Ferrara, R. Kallosh, A. Linde and M. Porrati, *Higher Order Corrections in Minimal Supergravity Models of Inflation*, *JCAP* **11** (2013) 046 [1309.1085].

[76] R. Kallosh and A. Linde, *Non-minimal Inflationary Attractors*, *JCAP* **10** (2013) 033 [1307.7938].

[77] L. Boubekeur and D.H. Lyth, *Hilltop inflation*, *JCAP* **07** (2005) 010 [hep-ph/0502047].

[78] J.M. Bardeen, *Gauge Invariant Cosmological Perturbations*, *Phys. Rev. D* **22** (1980) 1882.

[79] A.R. Liddle and D.H. Lyth, *Cosmological Inflation and Large-Scale Structure*, Cambridge University Press (2000), 10.1017/CBO9781139175180.

[80] D.H. Lyth, K.A. Malik and M. Sasaki, *A General proof of the conservation of the curvature perturbation*, *JCAP* **05** (2005) 004 [astro-ph/0411220].

[81] D. Wands, K.A. Malik, D.H. Lyth and A.R. Liddle, *A New approach to the evolution of cosmological perturbations on large scales*, *Phys. Rev. D* **62** (2000) 043527 [astro-ph/0003278].

[82] A. Riotto, *Inflation and the theory of cosmological perturbations*, *ICTP Lect. Notes Ser.* **14** (2003) 317 [hep-ph/0210162].

[83] R.L. Arnowitt, S. Deser and C.W. Misner, *The Dynamics of general relativity*, *Gen. Rel. Grav.* **40** (2008) 1997 [gr-qc/0405109].

[84] D. Polarski and A.A. Starobinsky, *Semiclassicality and decoherence of cosmological perturbations*, *Class. Quant. Grav.* **13** (1996) 377 [gr-qc/9504030].

[85] S.M. Leach and A.R. Liddle, *Inflationary perturbations near horizon crossing*, *Physical Review D* **63** (2001) .

[86] S. Chongchitnan, *Inflationary e-folding and the implications for gravitational-wave detection*, 2017. 10.48550/ARXIV.1705.02712.

[87] S.S. Mishra and V. Sahni, *Primordial black holes from a tiny bump/dip in the inflaton potential*, *Journal of Cosmology and Astroparticle Physics* **2020** (2020) 007.

[88] E.D. Stewart, *Flattening the inflaton's potential with quantum corrections*, *Phys. Lett. B* **391** (1997) 34 [hep-ph/9606241].

[89] E.D. Stewart, *Flattening the inflaton's potential with quantum corrections. 2.*, *Phys. Rev. D* **56** (1997) 2019 [hep-ph/9703232].

[90] L. Covi, D.H. Lyth and L. Roszkowski, *Observational constraints on an inflation model with a running mass*, *Phys. Rev. D* **60** (1999) 023509 [hep-ph/9809310].

[91] S. Kachru, R. Kallosh, A.D. Linde, J.M. Maldacena, L.P. McAllister and S.P. Trivedi, *Towards inflation in string theory*, *JCAP* **0310** (2003) 013 [hep-th/0308055].

[92] S. Iso, K. Kohri and K. Shimada, *Small field Coleman-Weinberg inflation driven by a fermion condensate*, *Phys. Rev. D* **91** (2015) 044006 [1408.2339].

[93] Planck collaboration, *Planck 2018 results. X. Constraints on inflation*, *Astron. Astrophys.* **641** (2020) A10 [1807.06211].

[94] W.H. Kinney, *A Hamilton-Jacobi approach to nonslow roll inflation*, *Phys. Rev. D* **56** (1997) 2002 [hep-ph/9702427].

[95] S. Inoue and J. Yokoyama, *Curvature perturbation at the local extremum of the inflaton's potential*, *Phys. Lett. B* **524** (2002) 15 [hep-ph/0104083].

[96] W.H. Kinney, *Horizon crossing and inflation with large eta*, *Phys. Rev. D* **72** (2005) 023515 [gr-qc/0503017].

[97] J. Martin, H. Motohashi and T. Suyama, *Ultra Slow-Roll Inflation and the non-Gaussianity Consistency Relation*, *Phys. Rev. D* **87** (2013) 023514 [1211.0083].

[98] Planck collaboration, *Planck 2013 results. XXII. Constraints on inflation*, *Astron. Astrophys.* **571** (2014) A22 [1303.5082].

[99] ACT collaboration, *The Atacama Cosmology Telescope: DR6 Power Spectra, Likelihoods and ΛCDM Parameters*, 2503.14452.

[100] ACT collaboration, *The Atacama Cosmology Telescope: DR6 Constraints on Extended Cosmological Models*, 2503.14454.

[101] T. Bringmann, P. Scott and Y. Akrami, *Improved constraints on the primordial power spectrum at small scales from ultracompact minihalos*, *Phys. Rev. D* **85** (2012) 125027 [1110.2484].

[102] K. Inomata and T. Nakama, *Gravitational waves induced by scalar perturbations as probes of the small-scale primordial spectrum*, *Phys. Rev. D* **99** (2019) 043511 [1812.00674].

[103] L. Kofman, A.D. Linde and A.A. Starobinsky, *Towards the theory of reheating after inflation*, *Phys. Rev. D* **56** (1997) 3258 [hep-ph/9704452].

[104] G.N. Felder, L. Kofman and A.D. Linde, *Tachyonic instability and dynamics of spontaneous symmetry breaking*, *Phys. Rev. D* **64** (2001) 123517 [hep-th/0106179].

[105] D. Battefeld, T. Battefeld, C. Byrnes and D. Langlois, *Beauty is Distractive: Particle production during multifield inflation*, *JCAP* **08** (2011) 025 [1106.1891].

[106] S.S. Naik, K. Furuuchi and P. Chingangbam, *Particle production during inflation: a Bayesian analysis with CMB data from Planck 2018*, *JCAP* **07** (2022) 016 [2202.05862].

[107] H. Kodama and T. Hamazaki, *Evolution of cosmological perturbations in a stage dominated by an oscillatory scalar field*, *Prog. Theor. Phys.* **96** (1996) 949 [gr-qc/9608022].

[108] B.A. Bassett, F. Tamburini, D.I. Kaiser and R. Maartens, *Metric preheating and limitations of linearized gravity. 2.*, *Nucl. Phys. B* **561** (1999) 188 [hep-ph/9901319].

[109] J.T. Giblin and A.J. Tishue, *Preheating in Full General Relativity*, *Phys. Rev. D* **100** (2019) 063543 [1907.10601].

[110] B. Eggemeier, P. Hayman, J.C. Niemeyer and R. Easther, *Postinflationary structure formation boosted by parametric self-resonance*, *Phys. Rev. D* **109** (2024) 043521 [2311.08780].

[111] C. Gordon, D. Wands, B.A. Bassett and R. Maartens, *Adiabatic and entropy perturbations from inflation*, *Phys. Rev. D* **63** (2000) 023506 [astro-ph/0009131].

[112] T. Murata and Y. Tada, *Stochastic-tail of the curvature perturbation in hybrid inflation*, 2507.22439.

[113] A.A. Starobinsky, *STOCHASTIC DE SITTER (INFLATIONARY) STAGE IN THE EARLY UNIVERSE*, *Lect. Notes Phys.* **246** (1986) 107.

[114] A.A. Starobinsky and J. Yokoyama, *Equilibrium state of a selfinteracting scalar field in the De Sitter background*, *Phys. Rev. D* **50** (1994) 6357 [astro-ph/9407016].

[115] M. Sasaki, Y. Nambu and K.-i. Nakao, *Classical Behavior of a Scalar Field in the Inflationary Universe*, *Nucl. Phys. B* **308** (1988) 868.

[116] J. Martin and V. Vennin, *Stochastic Effects in Hybrid Inflation*, *Phys. Rev. D* **85** (2012) 043525 [1110.2070].

[117] M. Kawasaki, K. Kohri and N. Sugiyama, *Cosmological constraints on late time entropy production*, *Phys. Rev. Lett.* **82** (1999) 4168 [astro-ph/9811437].

[118] S. Hannestad, *What is the lowest possible reheating temperature?*, *Phys. Rev. D* **70** (2004) 043506 [astro-ph/0403291].

[119] P.F. de Salas, M. Lattanzi, G. Mangano, G. Miele, S. Pastor and O. Pisanti, *Bounds on very low reheating scenarios after Planck*, *Phys. Rev. D* **92** (2015) 123534 [1511.00672].

[120] J.-O. Gong and M. Mylova, *Effective field theory of waterfall in hybrid inflation*, *JCAP* **07** (2022) 021 [2202.13882].

[121] F. Zwicky, *Die Rotverschiebung von extragalaktischen Nebeln*, *Helv. Phys. Acta* **6** (1933) 110.

[122] V.C. Rubin, N. Thonnard and W.K. Ford, Jr., *Rotational properties of 21 SC galaxies with a large range of luminosities and radii, from NGC 4605 /R = 4kpc/ to UGC 2885 /R = 122 kpc/*, *Astrophys. J.* **238** (1980) 471.

[123] V. de Lapparent, M.J. Geller and J.P. Huchra, *A Slice of the universe*, *Astrophys. J. Lett.* **302** (1986) L1.

[124] Y.B. Zel'dovich and I.D. Novikov, *The Hypothesis of Cores Retarded during Expansion and the Hot Cosmological Model*, *Sov. Astron.* **10** (1967) 602.

[125] B.J. Carr and S.W. Hawking, *Black holes in the early Universe*, *Mon. Not. Roy. Astron. Soc.* **168** (1974) 399.

[126] S.W. Hawking, *Particle Creation by Black Holes*, *Commun. Math. Phys.* **43** (1975) 199.

[127] Y.B. Zel'dovich and I.D. Novikov, *The Hypothesis of Cores Retarded during Expansion and the Hot Cosmological Model*, *Sov. Astron.* **10** (1967) 602.

[128] B.J. Carr, J.H. Gilbert and J.E. Lidsey, *Black hole relics and inflation: Limits on blue perturbation spectra*, *Physical Review D* **50** (1994) 4853.

[129] B. Carr and F. Kuhnel, *Primordial black holes as dark matter candidates*, *SciPost Phys. Lect. Notes* **48** (2022) 1 [2110.02821].

[130] M. Boudaud and M. Cirelli, *Voyager 1 $e^{\pm}$ Further Constrain Primordial Black Holes as Dark Matter*, *Phys. Rev. Lett.* **122** (2019) 041104 [1807.03075].

[131] B.J. Carr, K. Kohri, Y. Sendouda and J. Yokoyama, *Constraints on primordial black holes from the Galactic gamma-ray background*, *Phys. Rev. D* **94** (2016) 044029 [1604.05349].

[132] P.W. Graham, S. Rajendran and J. Varela, *Dark Matter Triggers of Supernovae*, *Phys. Rev. D* **92** (2015) 063007 [1505.04444].

[133] EROS-2 collaboration, *Limits on the Macho Content of the Galactic Halo from the EROS-2 Survey of the Magellanic Clouds*, *Astron. Astrophys.* **469** (2007) 387 [astro-ph/0607207].

[134] MACHO collaboration, *MACHO project limits on black hole dark matter in the 1-30 solar mass range*, *Astrophys. J. Lett.* **550** (2001) L169 [astro-ph/0011506].

[135] H. Niikura, M. Takada, S. Yokoyama, T. Sumi and S. Masaki, *Constraints on Earth-mass primordial black holes from OGLE 5-year microlensing events*, *Phys. Rev. D* **99** (2019) 083503 [1901.07120].

[136] Y. Inoue and A. Kusenko, *New X-ray bound on density of primordial black holes*, *JCAP* **10** (2017) 034 [1705.00791].

[137] H. Tashiro and N. Sugiyama, *Constraints on Primordial Black Holes by Distortions of Cosmic Microwave Background*, *Phys. Rev. D* **78** (2008) 023004 [0801.3172].

[138] M.A. Monroy-Rodríguez and C. Allen, *The end of the macho era, revisited: New limits on macho masses from halo wide binaries*, *The Astrophysical Journal* **790** (2014) 159.

[139] MUSE collaboration, *The MUSE-Faint survey: I. Spectroscopic evidence for a star cluster in Eridanus 2 and constraints on MACHOs as a constituent of dark matter*, *Astron. Astrophys.* **635** (2020) A107 [2001.08790].

[140] B. Carr and J. Silk, *Primordial Black Holes as Generators of Cosmic Structures*, *Mon. Not. Roy. Astron. Soc.* **478** (2018) 3756 [1801.00672].

[141] B.J. Carr and M. Sakellariadou, *Dynamical Constraints on Dark Matter in Compact Objects*, *Journal of something* **516** (1999) 195.

[142] R. Murgia, G. Scelfo, M. Viel and A. Raccanelli, *Lyman-α Forest Constraints on Primordial Black Holes as Dark Matter*, *Phys. Rev. Lett.* **123** (2019) 071102 [1903.10509].

[143] T. Harada, C.-M. Yoo and K. Kohri, *Threshold of primordial black hole formation*, *Phys. Rev. D* **88** (2013) 084051 [1309.4201].

[144] J.M. Bardeen, J.R. Bond, N. Kaiser and A.S. Szalay, *The Statistics of Peaks of Gaussian Random Fields*, *Astrophys. J.* **304** (1986) 15.

[145] S. Young, C.T. Byrnes and M. Sasaki, *Calculating the mass fraction of primordial black holes*, *JCAP* **07** (2014) 045 [1405.7023].

[146] A.M. Green, A.R. Liddle, K.A. Malik and M. Sasaki, *A New calculation of the mass fraction of primordial black holes*, *Phys. Rev. D* **70** (2004) 041502 [astro-ph/0403181].

[147] C.-M. Yoo, T. Harada, J. Garriga and K. Kohri, *Primordial black hole abundance from random Gaussian curvature perturbations and a local density threshold*, *PTEP* **2018** (2018) 123E01 [1805.03946].

[148] C.-M. Yoo, J.-O. Gong and S. Yokoyama, *Abundance of primordial black holes with local non-Gaussianity in peak theory*, *JCAP* **09** (2019) 033 [1906.06790].

[149] X. Wang, K. Kohri and T.T. Yanagida, *Primordial Black Holes Save R^2 Inflation*, 2506.06797.

[150] D.Y. Cheong, K. Kohri and S.C. Park, *The inflaton that could: primordial black holes and second order gravitational waves from tachyonic instability induced in Higgs-R^2 inflation*, *JCAP* **10** (2022) 015 [2205.14813].

[151] B.J. Carr, *The Primordial black hole mass spectrum*, *Astrophys. J.* **201** (1975) 1.

[152] W.H. Press and P. Schechter, *Formation of galaxies and clusters of galaxies by selfsimilar gravitational condensation*, *Astrophys. J.* **187** (1974) 425.

[153] I. Musco, J.C. Miller and L. Rezzolla, *Computations of primordial black hole formation*, *Class. Quant. Grav.* **22** (2005) 1405 [gr-qc/0412063].

[154] T. Terada, *Semianalytic calculation of the gravitational wave spectrum induced by curvature perturbations*, 2509.18694.

[155] D. Jeong, J. Pradler, J. Chluba and M. Kamionkowski, *Silk damping at a redshift of a billion: a new limit on small-scale adiabatic perturbations*, *Phys. Rev. Lett.* **113** (2014) 061301 [1403.3697].

[156] S. Weinberg, *Entropy generation and the survival of protogalaxies in an expanding universe*, *Astrophys. J.* **168** (1971) 175.

[157] N. Kaiser, *Small-angle anisotropy of the microwave background radiation in the adiabatic theory*, *Mon. Not. Roy. Astron. Soc.* **202** (1983) 1169.

[158] S. Weinberg, *Damping of tensor modes in cosmology*, *Phys. Rev. D* **69** (2004) 023503 [astro-ph/0306304].

[159] D.A. Dicus and W.W. Repko, *Comment on damping of tensor modes in cosmology*, *Phys. Rev. D* **72** (2005) 088302 [astro-ph/0509096].

[160] Y.-H. Yu, Z. Chang and S. Wang, *Comprehensive analysis of dissipative effects in the induced gravitational waves*, 10, 2025 [2510.18663].

[161] K. Schmitz, *New Sensitivity Curves for Gravitational-Wave Signals from Cosmological Phase Transitions*, *JHEP* **01** (2021) 097 [2002.04615].

[162] G. Hobbs, A. Archibald, Z. Arzoumanian, D. Backer, M. Bailes, N.D.R. Bhat et al., *The international pulsar timing array project: using pulsars as a gravitational wave detector*, *Classical and Quantum Gravity* **27** (2010) 084013.

[163] R.N. Manchester, *The international pulsar timing array*, *Classical and Quantum Gravity* **30** (2013) 224010.

[164] J.P.W. Verbiest, L. Lentati, G. Hobbs, R. van Haasteren, P.B. Demorest, G.H. Janssen et al., *The international pulsar timing array: First data release*, *Monthly Notices of the Royal Astronomical Society* **458** (2016) 1267.

[165] J.S. Hazboun, C.M.F. Mingarelli and K. Lee, *The Second International Pulsar Timing Array Mock Data Challenge*, Oct., 2018.

[166] C.L. Carilli and S. Rawlings, *Science with the Square Kilometer Array: Motivation, key science projects, standards and assumptions*, *New Astron. Rev.* **48** (2004) 979 [astro-ph/0409274].

[167] G. Janssen et al., *Gravitational wave astronomy with the SKA*, *PoS* **AASKA14** (2015) 037 [1501.00127].

[168] A. Weltman et al., *Fundamental physics with the Square Kilometre Array*, *Publ. Astron. Soc. Austral.* **37** (2020) e002 [1810.02680].

[169] P. Amaro-Seoane, H. Audley, S. Babak, J. Baker, E. Barausse, P. Bender et al., *Laser interferometer space antenna*, 2017.

[170] J. Baker et al., *The Laser Interferometer Space Antenna: Unveiling the Millihertz Gravitational Wave Sky*, Sept., 2019.

[171] N. Seto, S. Kawamura and T. Nakamura, *Possibility of direct measurement of the acceleration of the universe using 0.1-Hz band laser interferometer gravitational wave antenna in space*, *Phys. Rev. Lett.* **87** (2001) 221103 [astro-ph/0108011].

[172] S. Kawamura et al., *The Japanese space gravitational wave antenna DECIGO*, *Class. Quant. Grav.* **23** (2006) S125.

[173] K. Yagi and N. Seto, *Detector configuration of DECIGO/BBO and identification of cosmological neutron-star binaries*, *Phys. Rev. D* **83** (2011) 044011 [1101.3940].

[174] S. Isoyama, H. Nakano and T. Nakamura, *Multiband Gravitational-Wave Astronomy: Observing binary inspirals with a decihertz detector, B-DECIGO*, *PTEP* **2018** (2018) 073E01 [1802.06977].

[175] J. Crowder and N.J. Cornish, *Beyond LISA: Exploring future gravitational wave missions*, *Phys. Rev. D* **72** (2005) 083005 [gr-qc/0506015].

[176] V. Corbin and N.J. Cornish, *Detecting the cosmic gravitational wave background with the big bang observer*, *Class. Quant. Grav.* **23** (2006) 2435 [gr-qc/0512039].

[177] G.M. Harry, P. Fritschel, D.A. Shaddock, W. Folkner and E.S. Phinney, *Laser interferometry for the big bang observer*, *Class. Quant. Grav.* **23** (2006) 4887.

[178] LIGO Scientific, Virgo collaboration, J. Kissel, "*H1 Calibrated Sensitivity Spectra Jun 10 2017 (Representative Best of O2 - C02, With Cleaning / Subtraction)*.."

[179] LIGO Scientific, Virgo collaboration, J. Kissel, "*L1 Calibrated Sensitivity Spectra Aug 06 2017 (Representative Best of O2 - C02, With Cleaning / Subtraction)*.."

[180] LIGO Scientific, Virgo collaboration, "*GWTC-1: Fig. 1 ..*"

[181] LIGO Scientific, Virgo collaboration, L. Barsotti, P. Fritschel, M. Evans and S. Gras, "*Updated Advanced LIGO sensitivity design curve*."

[182] LIGO Scientific, Virgo collaboration, C. Berry, S. Fairhurst, B. O'Reilly, M. Razzano and P.J. Sutton, "*Prospects for Observing and Localizing Gravitational-Wave Transients with Advanced LIGO, Advanced Virgo and KAGRA*."

[183] M. Punturo et al., *The Einstein Telescope: A third-generation gravitational wave observatory*, *Class. Quant. Grav.* **27** (2010) 194002.

[184] S. Hild et al., *Sensitivity Studies for Third-Generation Gravitational Wave Observatories*, *Class. Quant. Grav.* **28** (2011) 094013 [1012.0908].

[185] B. Sathyaprakash et al., *Scientific Objectives of Einstein Telescope*, *Class. Quant. Grav.* **29** (2012) 124013 [1206.0331].

[186] ET collaboration, *Science Case for the Einstein Telescope*, *JCAP* **03** (2020) 050 [1912.02622].

[187] LIGO Scientific collaboration, *Exploring the Sensitivity of Next Generation Gravitational Wave Detectors*, *Class. Quant. Grav.* **34** (2017) 044001 [1607.08697].

[188] D. Reitze et al., *Cosmic Explorer: The U.S. Contribution to Gravitational-Wave Astronomy beyond LIGO*, *Bull. Am. Astron. Soc.* **51** (2019) 035 [1907.04833].

[189] A. Hebecker and T. Wrase, *The Asymptotic dS Swampland Conjecture - a Simplified Derivation and a Potential Loophole*, *Fortsch. Phys.* **67** (2019) 1800097 [1810.08182].

[190] M. Scalisi and I. Valenzuela, *Swampland distance conjecture, inflation and α-attractors*, *JHEP* **08** (2019) 160 [1812.07558].

[191] S.-J. Lee, W. Lerche and T. Weigand, *Emergent strings from infinite distance limits*, *JHEP* **02** (2022) 190 [1910.01135].

[192] M. Etheredge, B. Heidenreich, S. Kaya, Y. Qiu and T. Rudelius, *Sharpening the Distance Conjecture in diverse dimensions*, *JHEP* **12** (2022) 114 [2206.04063].

[193] B. Heidenreich, M. Reece and T. Rudelius, *Repulsive Forces and the Weak Gravity Conjecture*, *JHEP* **10** (2019) 055 [1906.02206].

[194] N.B. Agmon, A. Bedroya, M.J. Kang and C. Vafa, *Lectures on the string landscape and the Swampland*, 2212.06187.

[195] M. Cicoli, J.P. Conlon, A. Maharana, S. Parameswaran, F. Quevedo and I. Zavala, *String cosmology: From the early universe to today*, *Phys. Rept.* **1059** (2024) 1 [2303.04819].

[196] T. Hasegawa, N. Hiroshima, K. Kohri, R.S.L. Hansen, T. Tram and S. Hannestad, *MeV-scale reheating temperature and thermalization of oscillating neutrinos by radiative and hadronic decays of massive particles*, *JCAP* **12** (2019) 012 [1908.10189].

[197] M. Kawasaki, K. Kohri and N. Sugiyama, *MeV scale reheating temperature and thermalization of neutrino background*, *Phys. Rev. D* **62** (2000) 023506 [astro-ph/0002127].

[198] K. Ichikawa, M. Kawasaki and F. Takahashi, *The Oscillation effects on thermalization of the neutrinos in the Universe with low reheating temperature*, *Phys. Rev. D* **72** (2005) 043522 [astro-ph/0505395].

[199] K. Kohri, C.S. Lim and C.-M. Lin, *Distinguishing between Extra Natural Inflation and Natural Inflation after BICEP2*, *JCAP* **08** (2014) 001 [1405.0772].

[200] J.-c. Hwang, *Perturbations of the Robertson-Walker space - multicomponent sources and generalized gravity*, *Astrophys.J.* **375** (1991) 443.

[201] R.-g. Cai, S. Pi and M. Sasaki, *Gravitational Waves Induced by non-Gaussian Scalar Perturbations*, *Phys. Rev. Lett.* **122** (2019) 201101 [1810.11000].

[202] J.-P. Li, S. Wang, Z.-C. Zhao and K. Kohri, *Complete analysis of the background and anisotropies of scalar-induced gravitational waves: primordial non-Gaussianity f_{NL} and g_{NL} considered*, *JCAP* **06** (2024) 039 [2309.07792].

[203] J.-P. Li, S. Wang, Z.-C. Zhao and K. Kohri, *Angular bispectrum and trispectrum of scalar-induced gravitational waves: all contributions from primordial non-Gaussianity f_{NL} and g_{NL}*, *JCAP* **05** (2024) 109 [2403.00238].

[204] K.N. Ananda, C. Clarkson and D. Wands, *Cosmological gravitational wave background from primordial density perturbations*, *Physical Review D* **75** (2007) .

[205] Y. Lu, A. Ali, Y. Gong, J. Lin and F. Zhang, *Gauge transformation of scalar induced gravitational waves*, *Phys. Rev. D* **102** (2020) 083503 [2006.03450].

[206] P.C. Peters, *Gravitational radiation from relativistic systems*, *Phys. Rev. D* **5** (1972) 2476.

[207] D.E. Neville, *The Volume operator for spin networks with planar or cylindrical symmetry*, *Phys. Rev. D* **73** (2006) 124004 [gr-qc/0511005].